UPPSALA
UNIVERSITET

Digital Comprehensive Summaries of Uppsala Dissertations from the Faculty of Science and Technology 1498

Mimicking the Outer Coordination Sphere in [FeFe]-Hydrogenase Active Site Models

From Extended Ligand Design to Metal-Organic Frameworks

SONJA PULLEN

ACTA
UNIVERSITATIS
UPSALIENSIS
UPPSALA
2017

ISSN 1651-6214
ISBN 978-91-554-9878-8
urn:nbn:se:uu:diva-318975

Dissertation presented at Uppsala University to be publicly examined in Häggsalen, Ångströmlaboratoriet, Lägerhyddsvägen 1, Uppsala, Friday, 19 May 2017 at 13:15 for the degree of Doctor of Philosophy. The examination will be conducted in English. Faculty examiner: Professor Patrick L. Holland (Department of Chemistry - Yale University).

Abstract
Pullen, S. 2017. Mimicking the Outer Coordination Sphere in [FeFe]-Hydrogenase Active Site Models. *From Extended Ligand Design to Metal-Organic Frameworks*. *Digital Comprehensive Summaries of Uppsala Dissertations from the Faculty of Science and Technology* 1498. 115 pp. Uppsala: Acta Universitatis Upsaliensis. ISBN 978-91-554-9878-8.

Biomimetic catalysis is an important research field, as a better understanding of nature´s powerful toolbox for the conversion of molecules can lead to technological progress. [FeFe]-hydrogenases are very efficient catalysts for hydrogen production. These enzymes play a crucial role in the metabolism of green algae and certain cyanobacteria. Their active site consists of a diiron complex that is embedded in an interactive protein matrix.

In this thesis, two pathways for mimicking the outer coordination sphere effects resulting from the protein matrix are explored.

The first is the construction of model complexes containing phosphine ligands that are coordinated to the iron center as well as covalently linked to the bridging ligand of the complex. The effect of such linkers is an increased energy barrier for the rotation of the $Fe(CO_2)(PL_3)$-subunit, which potentially could stabilize a terminal hydride that is an important intermediate in the proton reduction cycle.

The second pathway follows the incorporation of [FeFe]-hydrogenase active site model complexes into metal-organic frameworks (MOFs). Resulting MOF-catalysts exhibit increased photocatalytic activity compared to homogenous references due to a stabilizing effect on catalytic intermediates by the surrounding framework. Catalyst accessibility within the MOF and the influence of the framework on chemical reactivity are examined in the work presented. Furthermore, an initial step towards application of MOF-catalysts in a device was made by interfacing them with electrodes.

The work of this thesis highlights strategies for the improvement of biomimetic model catalysts and the knowledge gained can be transferred to other systems mimicking the function of enzymes.

Keywords: [FeFe]-hydrogenases, outer coordination sphere, model complexes, biomimetic catalysis, artificial photosynthesis, metal-organic frameworks

Sonja Pullen, Department of Chemistry - Ångström, Molecular Biomimetics, Box 523, Uppsala University, SE-75120 Uppsala, Sweden.

ISSN 1651-6214
ISBN 978-91-554-9878-8
urn:nbn:se:uu:diva-318975 (http://urn.kb.se/resolve?urn=urn:nbn:se:uu:diva-318975)

“Iron is the master of them all”

Rudyard Kipling,
Cold iron, 1910 in Rewards and Fairies

This thesis is dedicated to my family.

List of papers

This thesis is based on the following papers, which are referred to in the text by their Roman numerals.

I **Direct Observation of Key Catalytic Intermediates in a Photoinduced Proton Reduction Cycle with a Diiron Carbonyl Complex.**
Mirmohades, M.; Pullen, S.; Stein, M.; Maji, S.; Ott, S.; Hammarström, L.; Lomoth, R.
J. Am. Chem. Soc. **2014**, *136*, 17366–17369.

My contribution: I conducted the catalyst synthesis and was responsible for the DFT calculations. I contributed to writing the manuscript.

II **Restricted Rotation in [FeFe]-Hydrogenase Active Site mimics by tethering phosphine ligands.**
Pullen, S.; Maji, S.; Ott, S.; Stein, M.
Manuscript in preparation.

My contribution: I planned the study, performed all experimental work except synthesis of compound **11**, and was main responsible for the DFT calculations. I wrote the manuscript.

III **Enhanced Photochemical Hydrogen Production by a Molecular Diiron Catalyst Incorporated into a Metal-Organic Framework.**
Pullen, S.[*]; Fei, H.[*]; Orthaber, A.; Cohen, S. M.; Ott, S.
J. Am. Chem. Soc. **2013**, *135*, 16997–17003.

My contribution: I synthesized and characterized the homogenous catalyst and was responsible for the photocatalysis study. I contributed to writing the manuscript.

IV **Catalyst Accessibility to Chemical Reductant in Metal-Organic Frameworks.**
Roy, S.[*]; Pascanu, V.[*]; Pullen, S.[*]; Gonzáles-Miera, G; Ott, S.; Martín-Matute, B.
Chem. Comm. **2017**, *53*, 3257–3260.

My contribution: I synthesized and characterized the molecular catalyst and performed initial photocatalysis experiments.

V **Functionalization of Robust Zr(IV)-based Metal–Organic Framework Films via a Postsynthetic Ligand Exchange.**
Fei, H.; Pullen, S.; Wagner, A.; Ott, S.; Cohen, S. M.
Chem. Comm. **2015**, *51*, 66–69.

My contribution: I synthesized the catalyst, contributed to developing the method for thin film preparation, and performed electrochemical characterization of functionalized thin films. I contributed to writing the manuscript.

VI **[FeFe] Hydrogenase Active Site Model Chemistry in a UiO-66 Metal-Organic Framework.**
Pullen, S.; Roy, S.; Ott, S.
Manuscript submitted to Chem. Comm.

My contribution: I planned the study and conducted all experimental work except electrochemical analysis of the MOFs. I wrote the manuscript.

* *Authors contributed equally to this work.*

Unpublished results

Chapter 5

Dual incorporation in UiO-67.

My contribution: I planned the study and conducted the synthetic work of the solvothermal synthesis approach. I performed the photocatalysis studies and electrochemical analysis of the ligand. I am responsible for the data analysis.

Ligand insertion in pcn-700.

My contribution: I tested ligand insertion of the catalyst into pcn-700 crystals and performed the characterization by optical microscopy, IR spectroscopy, and photocatalysis.

Chapter 6

Spectro-electrochemical analysis of UiO-66-1.

My contribution: I planned the study and performed all experimental work. I was responsible for data analysis and interpretation.

Papers not included in this thesis:

VII **Structural Dynamics inside a Functionalized Metal-Organic Framework Probed by Ultrafast 2D IR Spectroscopy.**
Nishida, J.; Tamimi, A.; Fei, H.; Pullen, S.; Ott, S.; Cohen, S. M.; Fayer, M. D.
PNAS **2014**, *111* 18442–18447.

VIII **The potential of ion beams for characterization of metal–organic frameworks.**
Wagner, A; Pullen, S.; Ott, S.; Primetzhofer, A.
Nuclear Instruments and Methods in Physics Research B, **2015**.

IX **Photochemical Hydrogen Production with Metal-Organic Frameworks.**
Pullen, S.; Ott, S.
Topics in Catalysis **2016**, *59*, 1712–1721.

X **Ultrafast Electron Transfer between Dye and Catalyst on a Mesoporous NiO Surface.**
Brown, A.; Antila, L.; Mirmohades, M.; Pullen, S.; Ott, S.; Hammarström, L.
J. Am. Chem. Soc. **2016**, *138*, 8060–8063.

XI **Homogeneous Cobalt/Vanadium Complexes as Precursors for Functionalized Mixed Oxides in Visible-Light-Driven Water Oxidation.**
Pavliuk, M. V.; Mijangos, E.; Makhankova, V. G.; Kokozay, V. N.; Pullen, S.; Liu, J.; Zhu, J.; Styring, S. and Thapper, A.
ChemSusChem **2016**, *9*, 1–11.

XII **Hydrogen Evolution with Nanoengineered ZnO Interfaces Decorated by a Beetroot Extract and a Hydrogenase Mimic.**
Sa, J.; Pavliuk, M. V.; Cieslak, A. M.; Abdellah, M.; Budinská, A.; Pullen, S.; Sokolowski, K.; Fernandes, D.; Szlachetko, J.; Bastos, E.; Ott, S.; Hammarström, L.; Edvinsson, T.; Lewinski
Journal of Sustainable Energy and Fuels, **2017**, *1*, 69–73.

XIII **Functional small molecules and polymers containing P=C and As=C bonds as hybrid pi-conjugated materials.**
Morales Salazar, D.; Mijangos, E.; Pullen, S.; Gao, M.; Orthaber, A.
Chem. Comm., **2017**, *53*, 1120–1123.

XIV **Electrochemical characterization of an organometallic catalyst incorporated in a non-conducting metal-organic framework.**
Mijangos, E.; Roy, S.; Pullen, S.; Lomoth, R.; Ott, S.
Dalton Trans., **2017**, DOI: 10.1039/C7DT00578D.

Reprints were made with permission from the publishers.

Contents

Abbreviations

adt	azadithiolate
ATP	Adenosine triphosphate
ATR-IR	attenuated total reflectance infrared spectroscopy
bdt	1,2-benzenedithiolate
BDC	1,4-benzene-dicarboxylic acid
BPDC	4,4'-biphenyl dicarboxylic acid
bpy	2,2'-bipyridine
BP-86	Becke-Perdew 86, DFT functional
B3-LYP	Becke, 3-parameter, Lee-Yang-Parr, DFT functional
CAT	catalyst
COOH	carboxylic acid
COSMO	conductor-like screening model
CV	cyclic voltammogram
dcbdt	1,4-dicarboxy-2,3-benzenedithiolate
DCM	dichloromethane
dcbpy	5,5'-dicarboxy-2,2'-bipyridine
def2-TZVP	basis set with triple-zeta valence polarization
DFT	density functional theory
DMF	dimethylformamide
dm-bpy	dimethyl-[2,2'-bipyridyl] 5,5' dicarboxylate
$E_{p,a}$	anodic potential
$E_{p,c}$	cathodic potential
$E_{1/2}$	half-wave potential
EDTA	ethylenediaminetetraacetic acid
EDX	energy dispersive X-ray
EXAFS	extended X-ray absorption fine spectroscopy
Fc/Fc^+	ferrocene/ferrocenium redox couple
Fe_d	distal iron
Fe_p	proximal iron
FT-IR	Fourier-transformed Infrared spectroscopy
FTO	fluorine doped tin oxide
GC	gas chromatography
ΔG	Gibbs free energy difference
G_{gas}	Gibbs free energy in gas phase
G_{solv}	Gibbs free energy in solution
H_2ase	hydrogenase
HR-MS	high-resolution mass spectrometry

ICP-OES	inductively coupled plasma optical emission spectrometry
IR	Infrared
mcbdt	1-monocarboxy-2,3-benzenedithiolate
mabdt	1-monoamide-2,3-benzenedithiolate
MLCT	metal to ligand charge transfer
MeCN	acetonitrile
MeOH	methanol
MIL-101	Materials Institute Lavoisier, No. 101
MOF	Metal-Organic framework
NMR	nucelar magnetic resonance spectroscopy
OEC	oxygen evolving complex
ORTEP	Oak Right Thermal Ellipsoid Plot
pcn-700	porous coordination network, No. 700
pdt	1,3-propyl-dithiolate
pK_a	negative decadic logarithm of K_a, the acid constant
Py	pyridine
PyBop	benzotriazol-1-yl-oxytripyrrolidinophosphonium (PF_6^-)
PRC	proton reduction catalyst
PS	photosensitizer
PS-I	photosystem I
PS-II	photosystem II
PSE	post-synthetic linker exchange
PSM	post-synthetic modification
PSI	post-synthetic linker insertion
PXRD	powder X-ray diffraction
SAM	self-assembled monolayer
SBU	sub-building unit
SEC	spectro-electrochemistry
SEM	scanning electron microscopy
$TBAPF_6$	tetrabutylammoniumhexafluorophosphate
THF	tetrahydrofuran
TMEDA	tetramethyl-ethylene diamine
TON	turnover number
TOF	turnover frequency
triflic acid	trifluormethanesulfonic acid
TTF	tetrathiafulvene
UiO-66	University in Oslo, No. 66
UV	ultraviolet
Vis	visual
WOC	water oxidation catalyst
ZIF	zeolithic imidazolium framework
ϵ	dielectric constant
$\pi*$	antibonding π orbital
ν_{CO}	vibrational frequencies of CO stretches

1. Introduction

"*Affordable and clean energy (for everyone)*" is one of the 17 goals for sustainable development stated by UNESCO in 2016.[1] Since it has become apparent that constant demographic and economic growth will undoubtedly lead to an energy crisis and a change in climate, scientists from all disciplines are seeking solutions.[2–4] In the development of renewable energy technologies, large efforts have already been achieved. Especially the development and implementation of solar cells have been a big step forward[5–7] and in many regions electricity from sunlight is already harvested – when the sun is shining. Similarly, there are plenty of windparks delivering large amounts of electricity[8] – if the wind is blowing. The main problem, however, is the fact that electricity cannot be stored in large quantities and therefore, it is still the fossil fuels (i.e. oil and natural gas) that are used to satisfy most of the global energy need.[9] They represent about 80 % of the energy consumed worldwide.[10] Not only the fact that the stocks of fossil fuels are limited and unequally distributed over the planet causes political and social problems;[11,12] the emission of greenhouse gas CO_2 from burning fossil fuels clearly affects the climate, as its increasing presence in the atmosphere is considered one of the major factors for global warming.[3,13]

Thus, it is one of the most important challenges in science today to search for and develop strategies to replace fossil fuels by cheap and environmentally friendly alternative fuels.[14–17] They should be retrieved from abundant resources and possibly be part of a continuous cycle that has the smallest possible negative effect on the environment. The process of finding such solutions is very long and diverse, and it requires large efforts in fundamental research.[18]

Hydrogen is considered to be a sustainable energy carrier,[19–22] as it is a nontoxic gas that can be produced from the cheap and abundant source water. Furthermore, its gravimetric energy storage density (120 MJ/kg) is the highest possible for all compounds that are considered as energy storage materials. If the stored energy is to be consumed, hydrogen can easily be reconverted into electricity by fuel cells. And if this process is carried out with molecular oxygen as reaction partner, water is the only byproduct, which makes this process clean and environmentally friendly. Today, the vast majority of hydrogen (96 %) is produced by steam reforming of fossil fuels.[23] In steam reforming, methane and steam react at high temperatures (approx. 1000 °C)

with a nickel catalyst to form hydrogen (H_2) and carbon monoxide (CO). In a second step at lower temperatures (approx. 200 – 400 °C) that is called the *water gas-shift reaction*, CO is reacted with water to form CO_2 and more H_2. Since fossil fuels are limited and CO_2 is released by this process, an alternative and sustainable production pathway is urgently needed. Splitting of water with the use of sunlight is one such alternative under consideration. A technically already available process makes use of solar panels that are coupled to an electrolyzer.[8] When electricity is generated by the solar cells, water is split into hydrogen and oxygen. However, a platinum catalyst is required in this commercially available technology. Platinum is a noble metal and therefore expensive. Furthermore, during the indirect conversion of solar energy via electricity into H_2, energy losses through wires and during electrolysis can be expected.[16] More promising would therefore be the development of catalysts based on inexpensive and more abundant metals that directly convert water into hydrogen.

Already in 1912, the Italian scientist Giacomo Ciamician realized the problem of our society being dependent on fossil fuels:

> "*MODERN civilization is the daughter of coal, for this offers to mankind the solar energy in its most concentrated form; that is, in a form in which it has been accumulated in a long series of centuries.*"[24]

In a detailed analysis of the situation, Ciamician realized that the sun is the most powerful source of energy. His solution for supplying the growing civilization in future was to use this energy and produce renewable solar fuels like the plants do.

1.1 Enzymes and Biomimetic Catalysis

As nature had billions of years to develop, it is an inexhaustible pool of beautiful concepts to be understood and used for mankinds purposes. In biomimicry, researchers are aiming to develop processes and products that are working based on nature's principles. One prominent example for this is the *Lotus effect*.[25] The leafs of the lotus flower are able to repell water very efficiently and thus keep themselves clean. The reason for this intriguing property is a very sophisticated surface architecture that minimizes the adhesion of water droplets. As water is collected at the surface, dirt particles can easily be washed away. This effect has been studied intensively by scientists and then used in nanotechnology applications such as self-cleaning glasses.[26]

Biomimetic catalysis takes nature's catalysts – the enzymes – as blueprints for creating functional (molecular) catalysts.[27,28] Enzymes contain active

sites, which often are built up from metals that are buried inside a protein matrix.[29,30] Catalysis that occurs at those metal centers is highly influenced and directed by surrounding amino acid residues. Specific channels and pockets enable substrate and product selectivity. In order to replicate the functionality of enzymes, it is probably not necessary to copy the entire structure. However, the most important aspects have to be understood and evaluated. Collaborative efforts from both biologists and chemists are required for this purpose. Crystallography and structural analysis of the enzyme are crucial for uncovering the identity of the active site and the constitution of its surrounding. Once the structure is known, chemists can synthesize model complexes with structural similarity and test their functionality.[31,32]

1.1.1 Artificial Photosynthesis

Artificial photosynthesis basically can be described as a concept of mimicking natural photosynthesis and other enzymatic processes for splitting of water. The produced reducing equivalents are used for the reduction of protons, carbon dioxide or other substances. The reactions are fascilitated by the help of synthetic catalysts and using sunlight as energy source.

Natural photosynthesis is a very complex process that can be divided into the light and the dark reactions. The light reactions are powered by sunlight and involve water splitting and reduction of $NADP^+$ to NADPH using the reducing equivalents generated by oxidation of water. Water splitting takes place in photosystem II (PS-II), and reduction of $NADP^+$ is done by photosystem I (PS-I). NADPH is then used in the fixation of CO_2 and its conversion into carbon-based compounds such as sugars; this process constitutes the dark reactions and is achieved by a complex machinery of enzymes.[33] The net reaction of natural photosynthesis is thus the following:

$$H_2O + CO_2 \xrightarrow{h\nu} O_2 + {}^1\!/_6(C_6H_{12}O_6) \tag{1.1}$$

Artificial photosynthesis simplifies the natural process and protons resulting from water oxidation are reduced directly to produce molecular hydrogen (Equation 1.2). Alternatively, reducing equivalents can be used for the reduction of CO_2. This is however a much more complex multi-electron process that can lead to a variety of reaction products such as CO or formate. In this thesis, the focus lies on the generation of molecular hydrogen.

$$2\,H_2O \rightarrow O_2 + 2\,H_2 \tag{1.2}$$

The first example of an artificial system that generated oxygen and hydrogen was presented 1972 by Honda and Fujishima.[34] They built a photoelectrochemical cell with a TiO_2-based anode and a platinum cathode to conduct water splitting under UV irradiation (Figure 1.1).

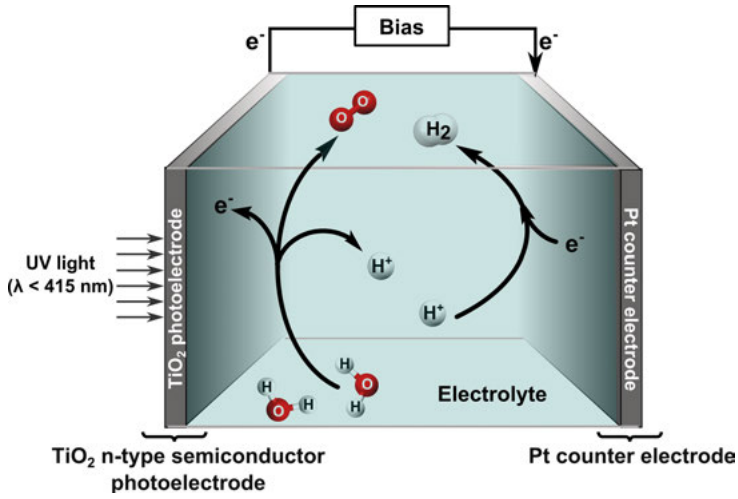

Figure 1.1. First photoelectrochemical cell for water splitting under UV light presented by Honda and Fujishima in 1972.[34]

Oxidation of water essentially yields molecular oxygen, protons, and electrons (Equation 1.3).

$$2\,H_2O \rightarrow O_2 + 4\,H^+ + 4\,e^- \tag{1.3}$$

Natural photosynthesis manages this multi-electron oxidation with a cubic Mn_4O_xCa cluster – the so called oxygen evolving complex (OEC).[35] OEC is embedded in a defined amino acid pocket and represents the heart of photosystem II. Water oxidation occurs close to the thermodynamic potential with a TOF of 400 s^{-1}. The reaction is enabled by the strong oxidant $P680^+$ that is produced after initial light absorption and oxidative quenching of the thereby produced excited state. $P680^+$ takes up electrons from OEC via a tyrosine residue in a step-wise, one-electron-at-a-time fashion. Protons are released into the thylakoid membrane and from there they can be delivered to other reaction centers.[33]

Synthetic model compounds of OEC have been prepared, and a recently presented model by a team around Zhao and Dau is to date the closest structural mimic.[36] This model complex resembles the Mn_4Ca-cluster very well and can undergo a four-fold oxidation. However, the functionality of the native OEC could not be reproduced with this model complex. There are functional molecular water oxidation catalysts (WOCs) based on manganese, ruthenium, iron, iridium, cobalt, and other metals.[37] Benchmarking molecular WOCs are mostly based on ruthenium. The first example of these was the so called *blue dimer*,[38] a dinuclear oxo-bridged ruthenium complex that was presented in 1982. Following up, Sun, Llobet, and others have developed a large number of ruthenium-based WOCs. With the use of strong oxidant Ce(IV) at pH 1, these catalysts reach TONs of up to 100 000 and TOFs of 1000 s^{-1}.[39]

Protons and electrons generated through water splitting can be used in different ways. Coming directly from the photosynthetic reaction, they are involved in ATP synthesis as they pass the thylakoid membrane.[33] Nature's catalysts for the conversion of protons to produce molecular hydrogen (Equation 1.4) are the hydrogenases.[40] Hydrogenases and their model complexes are the focus of this thesis and will be discussed in detail in the following section.

$$2\,H^+ + 2\,e^- \rightarrow H_2 \tag{1.4}$$

Platinum electrodes[34] and colloids[41] were used for proton reduction already more than 40 years ago. Later on, molecular platinum complexes have been reported in the literature.[42,43] Since platinum is a noble metal and thus not feasible for a sustainable solar fuel production system, alternative catalysts based on abundant metals are needed. Today, a large number of homogenous catalysts based on cheap metals such as iron, cobalt, and nickel are known. Among the best are cobalt-based catalysts in photochemical systems[44] and nickel-based *DuBois* catalysts[45,46] in electrochemical hydrogen formation, reaching TOFs up to 100 000 s^{-1}. In the work presented in this thesis, the focus lies on the investigation of proton reduction catalysts inspired by the active site of [FeFe]-hydrogenase enzymes.

There are also many heterogenous systems for both water oxidation and proton reduction.[47] Since the presented work focuses on molecular catalysts, these will not be further discussed. There are several advantages with molecular catalysts:

1. Synthesis of simpler molecular catalysts is straightforward. More complex structures can also be prepared employing smart synthetic strategies.
2. Their properties can be readily tuned by ligand design.
3. Molecular catalysts can be studied with common electrochemical and spectroscopic techniques.
4. Mechanistic studies can be supplemented and tested relatively easily by computations.
5. Molecular catalysts can be combined with photosensitizers in photocatalysis systems and screened for optimizing conditions.
6. In many cases, they are the closest mimics of enzymatic active sites.

A complete and functional system for solar-driven water splitting would need to couple both water oxidation and proton reduction. For this, there are various possible designs including catalyst-photosensitizer colloids suspended in electrolyte that are kept in bags.[48] An alternative design more common in research labs is the construction of a photoelectrochemical cell.[49–51] Figure 1.2 shows a schematic drawing thereof. Each of the two photoelectrodes is composed of a suitable semiconductor-based electrode that is sensitized with the respective catalyst and photosensitizer (PS). PS absorbs light of a specific

wavelength and drives the catalytic reaction by oxidizing or reducing the catalyst. The two functionalities can either be co-sensitized next to each other on the electrode surface, or attached in form of a molecular dyad.[52,53]

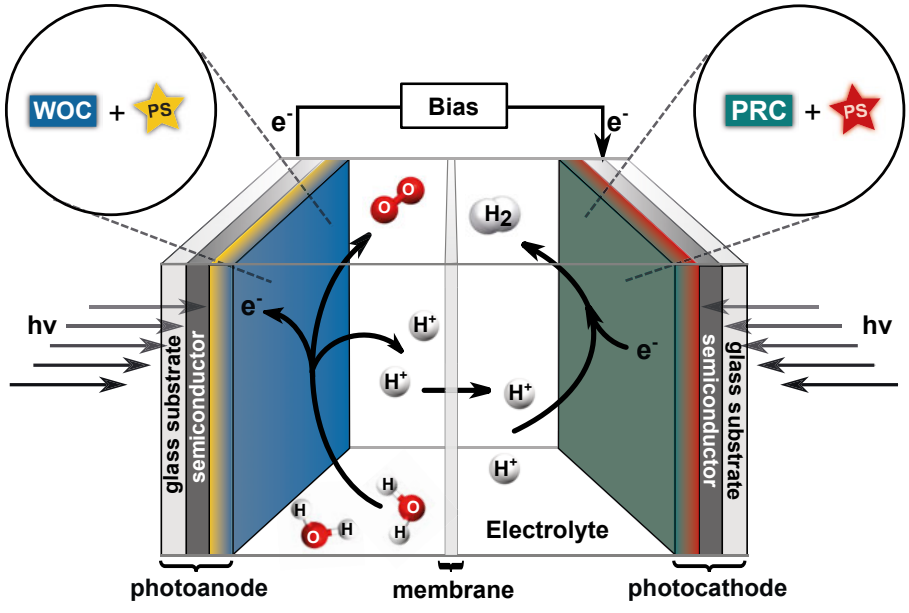

Figure 1.2. A possible setup of a photoelectrochemical cell for generating solar hydrogen and oxygen. The photoanode (left) consists of a seminconducting material decorated with a water oxidation catalyst (WOC) and a photosensitizer (PS). The photocathode comprises a proton reduction catalyst (PRC) and a PS.

1.1.2 [FeFe]-Hydrogenases

Hydrogenase enzymes (H_2ases) are nature's catalysts for the reversible transformation of protons and electrons into molecular hydrogen. They are significant in the metabolism of certain cyanobacteria and green algae.[40,54] Three different classes of hydrogenases are described, according to the constitution of their active sites: [NiFe]-H_2ases contain one nickel and one iron atom in their active center. The other two are iron-only hydrogenases with one ([Fe]-H_2ases) and two ([FeFe]-H_2ases) iron atoms, respectively. [NiFe]-H_2ases and [Fe]-H_2ases are mainly directed towards hydrogen oxidation; [FeFe]-H_2ases are very efficient proton reduction catalysts with TOFs reaching 9000 s^{-1}.[55]

The structure of [FeFe]-H_2ases in *Clostridium pasteurianum* has been identified by X-ray crystallography in 1998 (Figure 1.3).[56] The active site is composed of a dinuclear [2Fe2S] subunit (H-cluster) that is connected to a larger [4Fe4S] cubic cluster via a cystein linker. The iron that is connected to the cystein linker is denoted proximal (Fe_p), the other one distal (Fe_d). Several other

non-linked [4Fe4S] cubane clusters form an electron transport chain, enabling the transport of electrons between the outside of the protein and the H-cluster, where the actual catalysis takes place. In the active site, the two iron atoms are linked by a dithiolate bridge (-S-CH-X-CH-S-) and coordinate a set of three CO and two CN^- ligands, which are stabilizing the low oxidation states of the metal centers (Fe_p(II) and Fe_d(I)). One of the CO ligands resides in a bridging position between the two iron atoms and leaves an open coordination site at Fe_d. This position can either be free or occupied by a water molecule. In the catalysis mechanism, the open site is approached by a proton to form a terminal hydride. A deactivation pathway of [FeFe]-H_2ase proceeds via inhibition of the open site by a CO ligand.

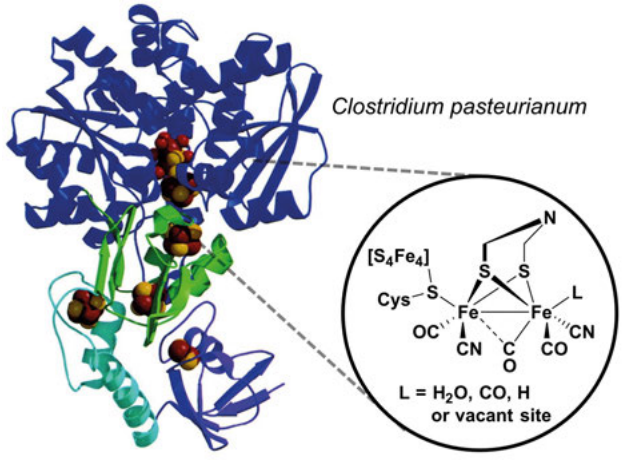

Figure 1.3. Crystal structure and schematic of the [FeFe] hydrogenase active site from *Clostridium pasteurianum*. The crystal structure is reprinted from reference [56] with permission from AAAS.

For a long time after the crystallographic report in 1998, the identity of the atom X in the dithiolate bridge was unknown, as crystallographic information was not clear enough. In 2009, a spectroscopic investigation by Lubitz and coworkers suggested that it should be a nitrogen atom.[57] A few years later, this finding was confirmed in a formidable study by a group of researchers around Lubitz, Fontecave, and Happe. They prepared three synthetic model complexes, structurally very similar to the H-cluster, with N, O, or CH_2 in the bridge. Each of these complexes was loaded onto bacterial *Thermotoga maritima* HydF, a helper protein for the assembly of the H_2ase. HydF loaded with the complex was then transferred to *apo-HydA1*, which is one of the hydrogenases of an algae called *Chlamydomonas reinhardtii*. Hydrogen evolution with resulting activated enzymes *HydA1* was tested and only the nitrogen-containing model complex yielded reactivity comparable to the

native enzyme.[58] From a mechanistic perspective, this assignment makes a lot of sense.

The mechanism of [FeFe]-H_2ase enzymes is quite different from heterogenous catalysts. Platinum electrodes for example produce hydrogen by stabilizing hydrogen atoms on the electrode surface. In [FeFe]-H_2ases, proton reduction proceeds via oxidative addition of a proton to the open coordination site on Fe_d (Scheme 1.1). A hydride intermediate is formed, which then combines with a second proton to form molecular hydrogen (Equation 1.5).[59,60]

$$2\,H^+ + 2\,e^- \rightarrow H^- + H^+ \rightarrow H_2 \qquad (1.5)$$

The pendant amine in the bridgehead can serve as a proton shuttle for the protonation and thereby reduce the energy barrier needed for the reaction.[61–63]

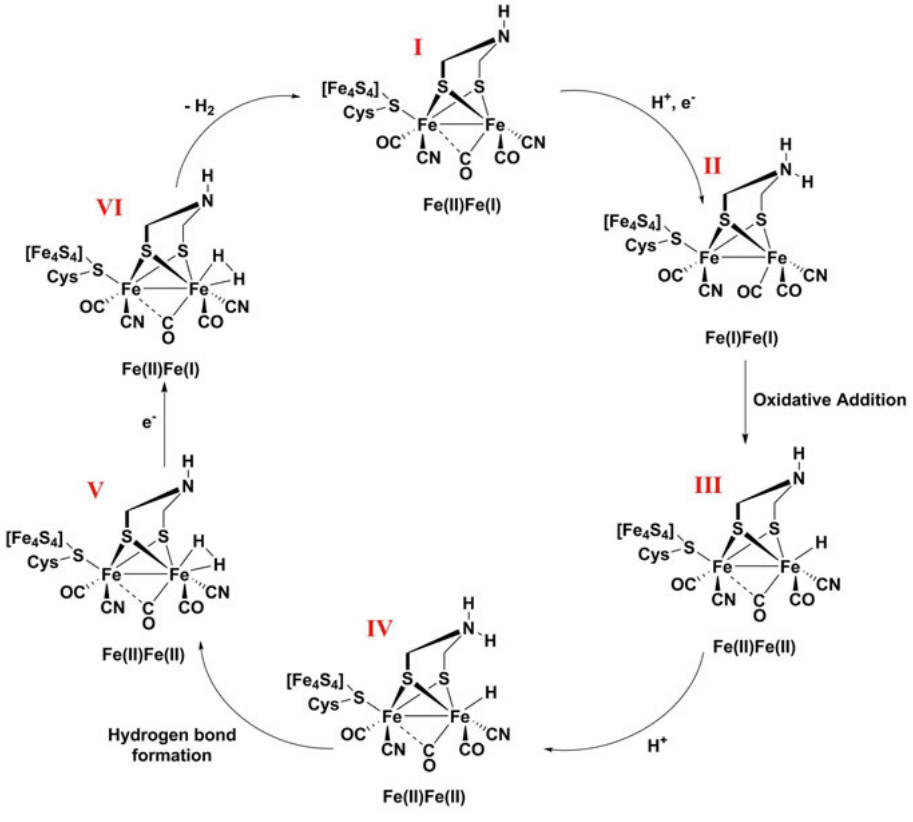

Scheme 1.1. Proposed catalytic cycle of proton reduction based on a theoretical study by Liu, Hall, and Zampella.[61]

Reiher and coworkers have investigated the mechanism quantum-mechanically in more detail.[64] They found that interactions between the active site and amino acid residues of the protein matrix play a crucial role. Initial formation

of a terminal hydride at Fe_d was calculated to be exothermic (e.g. thermodynamically feasible). From another computational study on model complexes it is known that this terminal hydride is thermodynamically not the most stable.[65] A bridging hydride between the two iron centers is more favorable. However, Reiher could show that in the enzyme the transformation of the terminal into the bridging hydride requires a ligand rearrangement that is prevented by strong interactions of the ligands with the surrounding protein matrix. The calculated energy barrier for this rearrangement was found to be 29 kcal mol^{-1}. An alternative pathway leading directly to the bridging hydride would proceed via protonation from a lysine residue. This proton transfer showed however to be endothermic. Therefore, the authors concluded that the pathway via formation of the terminal hydride is kinetically favored.

1.1.3 Artificial Model Compounds of the [FeFe]-H_2ase Active Site

Mimicking the structure and function of the [FeFe]-H_2ase active site has been in focus of organometallic chemists for a long time.[66] Even before the enzyme's structure was revealed in 1998, there had been iron-carbonyl complexes with thiol ligands in literature.[67] Since then, more than two hundred molecular model complexes have been prepared with different sets of ligands.[68,69]

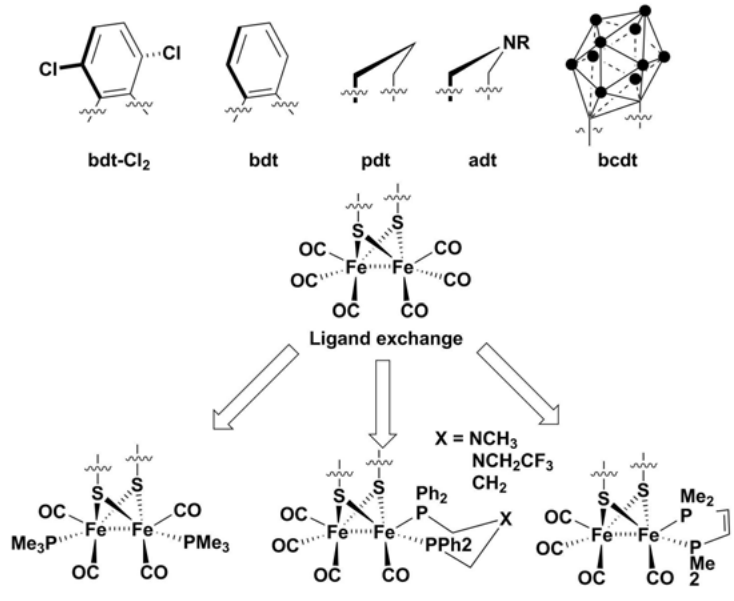

Scheme 1.2. Selection of model complexes of the [FeFe]-H_2ase active site.

Scheme 1.2 shows a selection of various model complexes. The nature of the bridging dithiolate ligand influences the electron density in the diiron cen-

ter. Propyldithiolate (pdt) complexes are reduced irreversibly, while benzenedithiolate bridged (bdt) complexes typically feature a reversible reduction.[70] In this thesis, only bdt-bridged complexes will be used. Hexacarbonyl iron dithiolate complexes are synthetically directly accessible from reacting iron carbonyl precursors (e.g. $Fe_3(CO)_{12}$) with the respective dithiolate ligand. Replacement of one or two CO ligands with stronger electron donating CN^- or phosphines enables further tuning of their electronic properties.[71,72] Furthermore, these models are seen as closer mimics to the enzyme's active site that also contains two cyanides.

Efforts have been made on making synthetic models that mimic the [FeFe]-H_2ase active site as close as possible. Diiron carbonyl complexes as presented in Scheme 1.2 are in the oxidation state Fe(I)Fe(I). In contrast, the enzyme active site starts the catalytic cycle in an Fe(II)Fe(I) oxidation state, due to the cysteine linker at Fe_p. Similar synthetic structures have been prepared by pendant thioether ligands attached to the bridging dithiolate. Upon oxidation of the initial Fe(I)Fe(I) complex, the pendant thioether coordinates to one of the iron centers and a similar Fe(II)Fe(I) structure as for the active site with one bridging CO has been observed spectroscopically.[73,74]

Another difference is that most synthetic models feature all ligands in terminal positions (eclipsed structure), while the [FeFe]-H_2ase active site contains one bridging CO (rotated structure) (Scheme 1.3).[75,76] Using a bidentate rigid phosphine[77] or bulky imidazole ligands,[78] rotated structures of synthetic models that formed upon one electron oxidation could be stabilized. In Paper II of this thesis, complexes containing phosphines that are tethered to the bridging dithiolate ligand were prepared and the effect on rotational energy barriers was investigated.

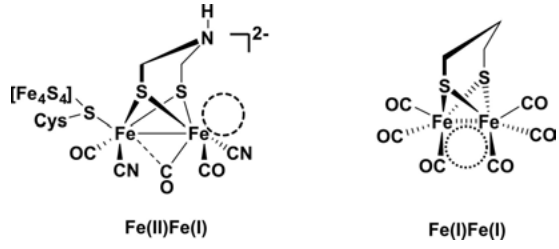

Scheme 1.3. Right: Active site of the [FeFe]-H_2ase (rotated structure). Dashed circle indicates the open coordination site. Left: Model complex $Fe_2(pdt)(CO)_6$ (eclipsed structure). Dotted circle represents the bridging position between the two iron centers.

Moving towards functional models, there have been many studies focusing on tuning and studying redox properties and protonation of model complexes in order to understand the catalytic mechanism. The most common technique that has been used for studying catalytic intermediates of [FeFe]-H_2ase active site models is cyclic voltammetry. Reduction behavior and potentials of different model complexes were investigated. Addition of acids yields informa-

tion about protonated intermediates. There are a number of different pathways of hydrogen formation with synthetic models. In general, at least two reduction and two protonation steps are necessary. In some cases, the complex is activated by an initial reduction.[79] The reaction pathway depends on experimental conditions (e.g. acid strength) and electronic properties of the complex. Bourrez et al. have investigated catalytic intermediates of proton reduction with the model complex $Fe_2(adt)(CO)_6$ (adt = azadithiolate) by use of electrochemistry and DFT.[80] Similar to the enzyme active site, the nitrogen in the adt bridge can be protonated with sufficiently strong acids (chloroacetic acid). Upon reduction, the proton is transferred to one iron center. Catalytic turnover continues from there either via protonation followed by reduction, or the reverse. In a similar fashion, the bdt-analog $Fe_2(bdt)(CO)_6$ has been investigated by Lichtenberger and coworkers.[81] The bdt-bridge allows delocalization of electrons and thus promotes a different electrochemical behavior than pdt- and adt-bridged complexes: The reduction of the bdt-complexes is a two-electron process, is electrochemically reversible, and occurs at milder potential. In Paper I of this thesis, we could identify the structure of the singly-reduced complex and obtain kinetic information about its protonation.

In nature, the formation of a terminal hydride at the open coordination site on Fe_d and rapid continouus reaction with an additional proton are enabled by interactions with the protein matrix.[64,82] Stabilization of terminal hydrides in synthetic models is still a challenge. So far, bulky and rigid phosphine ligands have been used to stabilize terminal hydrides at low temperatures.[83–85] In most studies, the thermodynamically favored bridging hydride remains however the primarily observed intermediate.[66,86]

Catalytic activity of [FeFe]-H_2ase model complexes has initially been investigated by electrochemical techniques in presence of acids. As a first example, Gloaguen presented electrochemical proton reduction of the pdt-bridged complex $Fe_2(pdt)(CO)_4(PMe_3)(CN)$.[87,88] Three years later, Ott et al. could show that the overpotential for proton reduction by $Fe_2(adt)(CO)_6$ is shifted 230 mV less negative, if the bridge contains a nitrogen (adt) instead of carbon (pdt).[89] As described above, adt can be protonated and function as a proton relay like in the enzyme active site. More synthetic model complexes containing pendant amines have been prepared. DuBois has introduced P_2N_2 ligands that work quite well as proton relays in nickel complexes for electrochemical proton reduction.[45] Similar PNP-ligands were used for Fe_2-complexes to investigate the influence of a pendant base on protonation.[90] Mononuclear iron complexes with PNP-ligands were active in electrochemical hydrogen production with acetic acid at low overpotentials.[91]

Photochemical hydrogen formation with an [FeFe]-H_2ase model complex was first demonstrated by Sun and coworkers.[92] They used $[Ru](bpy)_3Cl_2$ as photosensitizer and an adt-bridged model complex containing two $P(Py)_3$ ligands. The highest TON was achieved with a 10:1 (catalyst:photosensitizer) ratio. Much better yields (TON 200) were achieved by our group in 2010

employing $Fe_2(bdt{-}Cl_2)(CO)_6$ and $[Ru](bpy)_3Cl_2$.[93] The better performance was attributed to the electrochemically reversible reduction of this complex at milder overpotential.

Most of the previously described model complexes are water-insoluble and catalysis studies were performed in MeCN or DMF/H_2O mixture. A valuable future catalyst for hydrogen production should however be operating in purely aqueous media. There were prior approaches to make [FeFe]-H_2ase model complexes water soluble; for example by introducing hydrophilic ligands[94] or embedding a complex sulfonated at the bridgehead into cyclodextrines.[95] In the work of this thesis, water solubility was achieved by introducing two COOH groups in ortho-position to the thiols in the bdt-bridged model complex $Fe_2(bdt)(CO)_6$. Water solubility allowed for performing photocatalytic hydrogen production in aqueous buffer solutions (Paper III). Also the heterogenous MOF-catalysts prepared in this thesis all work in water (Paper III, IV and chapter 5).

1.2 Metal-Organic Frameworks – MOFs

Metal-Organic Frameworks (MOFs) are crystalline and highly porous materials with very high surface areas.[96] They are built up from organic molecules (linkers) with two or more binding groups (e.g. COOH, pyridyl, or imidazolium) that are coordinating metal ions or clusters. Depending on the connectivity of linkers and metals, two-dimensional sheets or three-dimensional structures are formed.[97,98] An overview over most commonly used linkers used in MOFs is presented in Scheme 1.4.

The large variety of metals and organic linkers that can be used to form MOFs allows for structural and functional design according to desired application.[99] They are used for gas storage and separation,[100–103] chemical sensing,[104] drug delivery,[105] and catalysis.[106–108] As the field is constantly growing at high speed, many more applications are under development.

The first stable, three-dimensional MOF has been described by Yaghi et al. as MOF-5 in 1999.[109] It consists of Zn_4O tetraedric knots connected via 1,4-benzene dicarboxylate (BDC). Every edge of the tetraeder connects one carboxylate group, forming $[Zn_4O(CO_2)_6]$ clusters as sub-building units (SBUs). MOF-5 features a surface area of 2900 $g^2\,cm^{-1}$ at a density of 0.59 $g\,cm^{-3}$. This means that about 80 % of the crystal volume represents pores that can be filled with solvent or other small guest molecules. MOF-5 is the most important candidate of a series of MOFs with isoreticular structure.

Other well-known MOFs that have been used in this thesis are MIL-101 (MIL = Materials Institute Lavoisier, no. 101)[110,111] and the UiO-series (UiO = University in Oslo).[112,113]

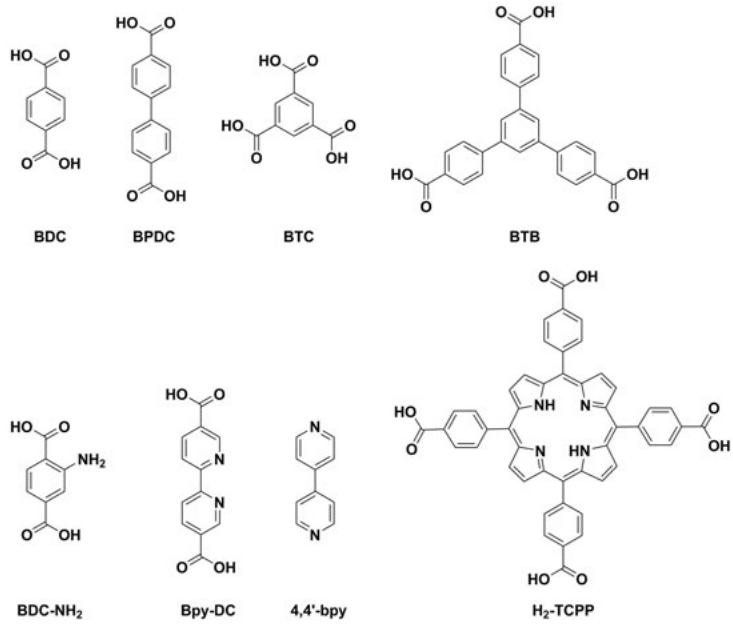

Scheme 1.4. Overview over commonly used organic linkers in MOFs.

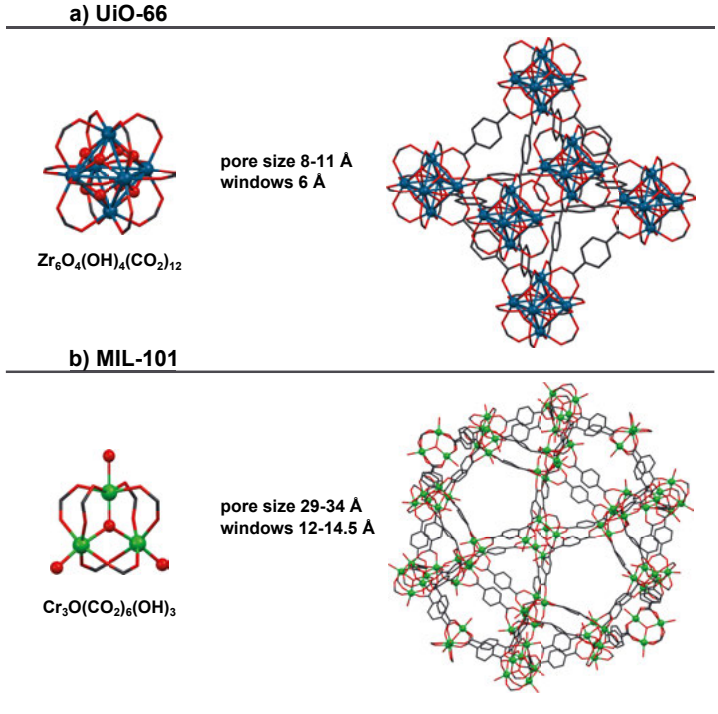

Figure 1.4. SBU and pore structures of a) UiO-66[112,114] and b) MIL-101.[111]

In Papers III, V, and VI of this thesis, UiO-66(Zr) was employed for immobilization of an [FeFe]-H_2ase active site model complex. In Paper IV, MIL-101(Cr) was utilized. Figure 1.4 presents the structures of the two. UiO-66 comprises octahedral and tetrahedral pores that are built up from Zr-clusters of the structure $Zn_6O_4(OH)_4(CO_2)_{12}$ as SBUs connected by BDC linkers. MIL-101 is based on $Cr_3O(CO_2)_6(OH)_3$-clusters that are linked by BDC and has spherical pores.

In chapter 5, UiO-67 was used for dual functionalization. UiO-67(Zr) is the analog of UiO-66 with larger BPDC linkers. Another MOF that has been used in chapter 5 is pcn-700(Zr) (pcn = porous coordination network).

1.2.1 MOF Synthesis and Post-Synthetic Functionalization

Typically, MOFs are prepared via solvothermal synthesis, i.e. the metal precursor is dissolved together with the organic linker in a suitable solvent (often DMF) and the mixture is heated in an oven for 24 – 48 h. For the preparation of certain MOFs (e.g. UiO-66), modulator reagents such as acetic or benzoic acid are additionally used, helping to form the metal-clusters during the synthesis.[98]

For the preparation of functional MOFs, in many cases alternative (post-synthetic) strategies have to be used if the desired function cannot be introduced solvothermally. The following methods have been developed throughout the years:

1. Post-synthetic modification (PSM) on the organic linkers of the pristine MOF (e.g. amino-functionalized linkers).[115] Another form of PSM is the post-synthetic metalation of open coordination sites such as 2,2'-bpy.[116]
2. Post-synthetic linker exchange (PSE) of linkers with matching size.[117]
3. Post-synthetic linker insertion (PSI) of linkers that fit into open pockets in the pre-formed framework.[117]

Figure 1.5 presents an overview over the different strategies that have been used in this thesis for functionalizing different MOFs with catalysts mimicking the [FeFe]-H_2ase active site. In Paper III, UiO-66 has been functionalized via PSE (*a)*). MIL-101 has been modified post-synthetically via amide coupling of the catalyst to the amino-functionalized linkers in Paper IV (*b)*). Direct solvothermal synthesis has been employed for functionalizing UiO-67 with the photosensitizer [Ru](dcbpy)$(bpy)_2(Cl_2)$ in chapter 5 (*c)*). A similar bifunctional material was obtained via post-synthetic metalation of open bpy-sites with [Ru]$(bpy)_2(Cl_2)$. And post-synthetic linker insertion was tested on pcn-700 in chapter 5 (*d)*).

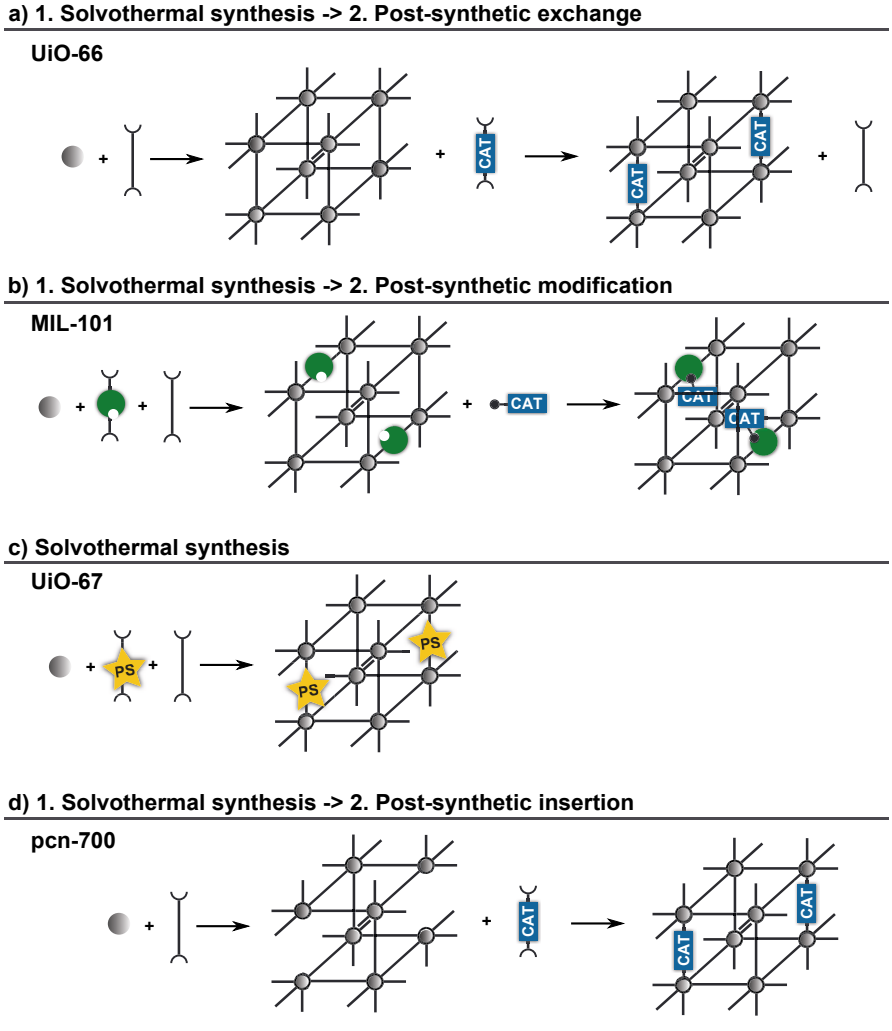

Figure 1.5. Functionalization of the different MOFs used in this thesis with catalysts and photosensitizers during solvothermal synthesis and via post-synthetic methods. Grey circles are metal-clusters. Green circle is either a functional group (amino) or an open metal-binding site (bpy) in case of metalation with photosensitizer. CAT = catalyst, PS = photosensitizer.

1.2.2 MOFs in Artificial Photosynthesis

MOFs possess defined pores and channels that are reminiscent to the situation in enzymes.[118] A large variety of organic linkers can be used and functionalized, allowing for fine-tuning of the MOF's interior properties. They seem thus ideal scaffolds for incorporation of molecular enzyme active site models, as they potentially could mimic effects of the outer coordination sphere (=

protein matrix). In this thesis, the potential of MOFs as hosts for molecular catalysts will be evaluated (chapters 4 – 8).

MOFs have been utilized for artificial photosynthesis. Mostly, proton reduction catalysts of molecular or heterogenous nature have been introduced to MOFs.[119] More recently, examples for water oxidation[120–126] and CO_2 reduction[127–131] were presented in the literature.

For use in artificial photosynthesis, the MOFs are required to be stable under catalysis conditions. This means in aqueous solution or aqueous/organic solvent mixtures at a range of different pH. Burtch et al. have summarized water-stable MOFs and their properties in a review in 2014.[132] Both the strength of the metal-to-ligand bond and the connectivity of the metal-cluster are important for the MOF's water stability. The bond strength depends on the linkers' basicity and the Lewis-acidity of the coordinating metal. An example for a highly thermodynamically stable MOF is ZIF-8, which consists of imidazolium linkers (pK_a 18.6) that are connected to the hard Lewis acid Zn^{2+}.[133] $Zr_6(OH)_4O_4$-clusters that are SBUs of the UiO-series contribute to the frameworks' kinetic water stability due to their ability to coordinate 12 COOH-linkers.[113] In this thesis, PSE of a molecular catalyst into UiO-66 is performed in water (Paper III). It is somewhat surprising that these "water-stable" MOFs can undergo this process, which is actually facilitated by water molecules that fill up open coordination sites during the course of linker exchange. PSE takes advantage of the higher acidity of the linkers compared to solvent molecules. When a linker dissociates, the open position can temporarily be replaced by a solvent molecule (e.g. H_2O or DMF). Since the framework is kinetically stabilized by all other linkers that are connected to the cluster, it stays intact and the incoming linkers take up the positions of weakly attached water molecules. A similar mechanism is used in post-synthetic linker insertion, where there are open positions in the framework after synthesis. Solvent molecules cover these positions until an incoming linker replaces them to form a kinetically more stable structure.[117]

In artificial photosynthesis, most commonly used MOFs have been UiO-66 and UiO-67 (both Zr-based),[112] MIL-53 (Al and Cr),[110] MIL-101 (Cr),[111] and MIL-125 (Ti)[134] as well as porphyrine-based MOFs.[135] They all are exceptionally water-stable and also find applications in other fields of catalysis.

1.3 Fundamentals and Methods

In this thesis, a variety of techniques has been used to characterize catalysts and study mechanistic aspects. The following sections will briefly describe the most important concepts and methods. For further information about experimental details, the reader is referred to the supporting information of the papers attached to this thesis.

1.3.1 Infrared Absorption Spectroscopy – IR

Vibrational infrared (IR) spectroscopy is a valuable technique for investigating iron carbonyl complexes, since the CO ligands give rise to characteristic absorption bands around 2000 cm^{-1}. Vibrations of the CO ligands (ν_{CO}) arise from absorption of light in the mid-IR-region. Since the resulting vibrations of the molecule cause a change in dipole moment, they are visible in the IR spectrum. The wavenumber of the respective frequency ν_{CO} is a sensitive indicator for the electron density in the metal center. In Figure 1.6, the three different metal-CO interactions are shown. The most important is the π^*-backbonding interaction that pushes electron density from filled metal-d-orbitals into the antibonding π^*-orbital of the CO ligand. The more electron density is present in the metal, the larger is this effect, and the weaker the CO bond becomes. This is represented by a shift of the vibrational frequency towards lower wavenumbers.

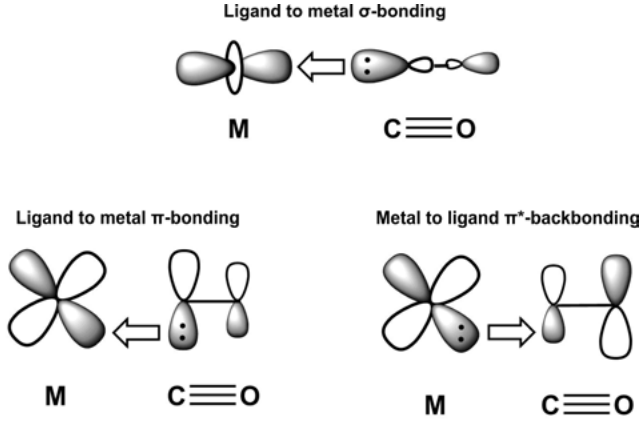

Figure 1.6. Metal-CO bond interactions that influence electron density in the metal center. π^*-backdonation weakens the C–O bond and decreases vibrational stretching frequencies ν_{CO}.

The number of ν_{CO} bands depends on the symmetry of the complex and the number of CO ligands. Figure 1.7 shows the assignments of ν_{CO} stretching frequencies in the [FeFe]-H_2ase model complex $Fe_2(bdt)(CO)_6$. The given spectrum is obtained experimentally in MeCN and assignments are taken from DFT calculations (Paper I). The shape of the spectrum is representative for most of the complexes studied in this thesis; electronic effects that are evoked by modifications of the complex are displayed by shifts of the wavenumbers. Structural changes are respesented by a change in the number of absorption bands or the shape of the spectrum. Also the difference between terminal and bridging CO ligands is quite clear. Since bridging CO ligands interact with both metals, π^*-backbonding becomes stronger and the corresponding absorption bands occur at lower wavenumbers compared to terminal CO ligands.

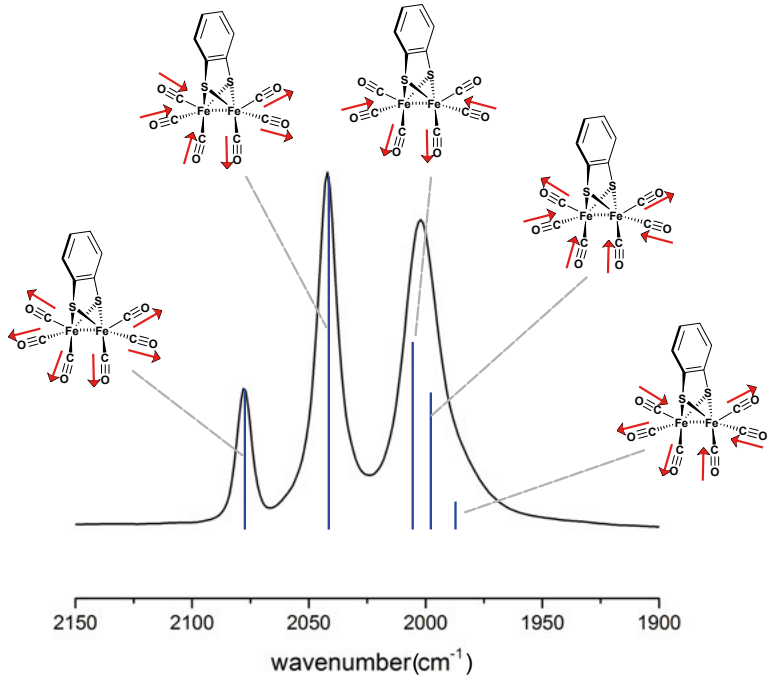

Figure 1.7. IR stretching frequencies of the CO ligands on the example of $Fe_2(bdt)(CO)_6$. The experimental spectrum in MeCN is shown. Assignments of the bands are obtained from DFT calculations.

1.3.2 Density Functional Theory – DFT

In Papers I and II of this thesis, DFT calculations have been used to identify the structures of catalytic intermediates and transition states as well as for the calculation of vibrational frequencies, and reduction potentials. All calculations were performed with the TURBOMOLE Program Package (version 6.3).[136]

For most calculations, the BP-86 (Becke-Perdew 86) exchange-correlation functional has been used.[137,138] In DFT, the energy of a system can be computet with a functional that considers the electron density alone.[139] E.g. BP-86 uses a gradient of the electron density for the calculation. BP-86 has been employed previously for transition metal complexes mimicking the [FeFe]-H_2ase active site and has shown good agreement with experimental data (X-ray crystal structures and IR frequencies).[140–142]

In Paper II also the B3-LYP (Becke, 3-parameter, Lee-Yang-Parr) functional has been used.[143–145] B3-LYP is a hybrid functional that includes 20 % of exact Hartree-Fock exchange together with the exchange-correlation func-

tion.

As basis set def2-TZVP was used for all atoms in all calculations, which is a large triple-zeta basis set containing polarization functions. Def2-TZVP is comparable to 6-311G** that is commonly used in the Gaussian program.[146]

All the presented structures are geometry optimized in gas-phase. As a starting geometry, the crystal structure coordinates of complexes **1** or **2** (Fe_2(mcbdt)$(CO)_6$) were used and the other complexes were constructed with the molecular builder *TMoleX* based on the structure of **2**. For the calculation of the reduction potentials in chapter 2, structures in solution were calculated using the conductor-like screening model (COSMO).[147] Gibbs free energies were obtained from vibrational frequency calculations at 298 K. IR frequencies were obtained by analytical evaluation of the second derivative of the DFT energy expression (*aoforce* program in Turbomole). The lack of negative eigenvalues for all structures confirmed that they are true minima. Transition state structures were calculated based on an intitial guess that was optimized until the analytical vibrational frequency calculation resulted in only one imaginary frequency.

1.3.3 Photocatalysis

Photocatalysis is used in Paper III, IV, and chapter 5 of this thesis to investigate the performance of the different catalysts. Since iron carbonyl complexes themselves are usually not photocatalytically active, a photosensitizer is used to drive the reaction. The photosensitizer (PS) employed in this thesis is [Ru](bpy)$_3$Cl$_2$, which has an absorption maximum of around 450 nm in aqueous solution. This absorption corresponds to a metal-to-ligand charge transfer (MLCT). Photoreduced $[Ru(bpy)_3]^+$ has a sufficiently high reduction potential to reduce the catalysts used in this thesis.[93][148] A typical photocatalysis scheme is drawn in Scheme 1.5. The mechanism is adapted from Schmehl et al.[149] Excited photosensitizer ($[Ru(bpy)_3]^{*2+}$) is reductively quenched by the sacrificial electron donor ascorbate (Asc) to form $[Ru(bpy)_3]^+$. The reduced photosensitizer transfers one electron to the catalyst to form the singly-reduced catalyst (Cat^-). A second reducing equivalent is produced by excitation and reduction of another PS molecule and the catalyst is reduced once again (Cat^{2-}). The doubly-reduced catalyst finally produces one molecule of hydrogen.
In this thesis, hydrogen has been detected either with a solid state H_2-sensor (Paper III) or with a gas chromatograph (GC, Paper IV).

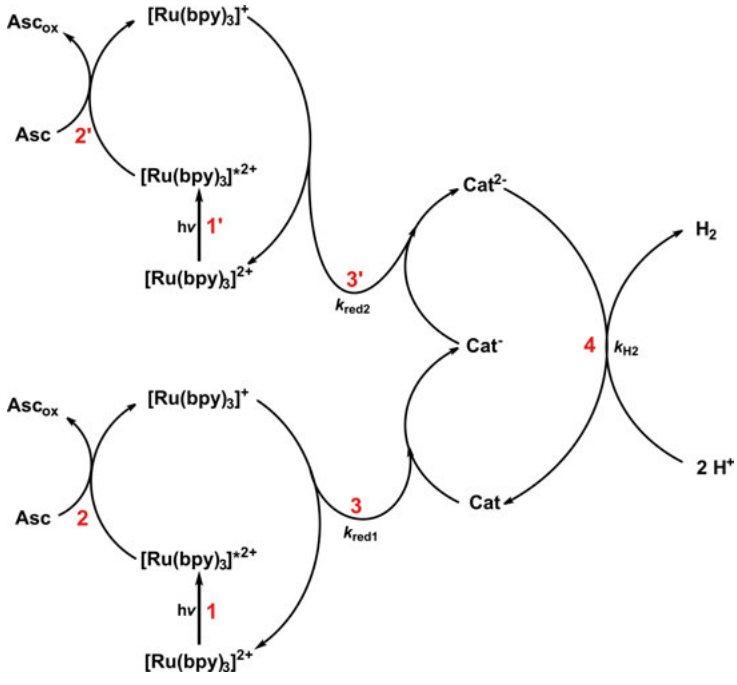

Scheme 1.5. Schematic overview of photochemical hydrogen production as used in this thesis. Two reducing equivalents need to be generated for producing one molecule of hydrogen. The scheme is inspired by Schmehl et al.[149]

1.3.4 Characterization of MOF-Catalysts

Many techniques for the characterization of MOFs have already been established. For structural analysis, typically powder X-ray diffraction (PXRD) and scanning electron microscopy (SEM) are used. The surface area is determined by a method developed by Brunauer-Emmet-Teller (BET). Composition of the MOFs can be identified by elemental analysis (EA), thermogravimetric analysis (TGA), ^{1}H-NMR of digested samples, and others.

IR spectroscopy as described above is straightforward for solid samples when an ATR-IR (ATR = attenuated total reflectance) spectrometer is available. ATR-IR can be used to study dry powder samples. In Paper IV and VI of this thesis, liquid IR spectroscopy has been used to follow reactions of the incorporated catalyst in-situ. For this, suspensions of MOF-catalysts were added to the liquid IR cell. Thanks to the strong absorption bands of the CO ligands, light scattering by MOF particles did not have a major influence on the quality of resulting spectra.

In this thesis, also (spectro-) electrochemical methods have been used that are rather unconventional for analysis of MOFs. While they are well estab-

lished for the study of homogenous catalysts, the heterogenous nature of MOF-catalysts accounts for difficulties that had to be overcome. UiO-66 that is mainly used in this thesis is insulating due to the fact that both the highest occupied crystal orbital (HOCO) and the lowest occupied crystal orbital (LUCO) are located at the organic linkers.[150] Thus, charge transfer between the linkers and the metals is not facilitated. A method for electrochemical analysis of powder UiO-66 has been developed recently by our group.[151]

1.4 Outline of this Thesis

Main questions to be answered in this thesis are:

1. What is the best strategy to mimic outer coordination sphere effects of the [FeFe]-H_2ase active site?
2. Are MOFs good scaffolds for incorporating molecular proton reduction catalysts and what design features are critical?
3. How do different MOFs influence catalyst accessibility and reaction mechanisms?

In Paper I, catalytic intermediates of $Fe_2(bdt)(CO)_6$ are identified. Data obtained from this project is used as a reference throughout the thesis.

In Paper II, extended ligand design is probed as a path to mimic interactions of amino acid residues with CN^- ligands in the [FeFe]-H_2ase active site. A new series of active site model complexes is introduced featuring phosphine ligands that are tethered to the bdt-bridge. Thereyby, they are increasing the rotation energy barrier of the $Fe(CO)_2(PL_3)$-subunit.

In Paper III, a new model complex with two carboxylates in the bdt bridge is prepared and introduced to the UiO-66 framework by PSE. Photochemical hydrogen production with the new material is investigated.

In Paper IV, a second model complex with only one carboxylate group in the bdt bridge is prepared and coupled to amino-groups in MIL-101. Catalyst accessibility in this material is studied by chemical reduction with cobaltocene and compared to UiO-66.

In Paper V, thin films of UiO-66 on conducting FTO glass are prepared and functionalized with the catalyst. An electrochemical study with these electrodes is performed.

In Paper VI, [FeFe]-H_2ase model chemistry inside UiO-66 is studied.

This thesis also contains unpublished results. In chapter 5, functionalization of UiO-67 with both catalyst and photosensitizer is investigated as well as post-synthetic linker insertion in pcn-700. In chapter 6, a follow-up study on catalyst accessibility in UiO-66 is presented, using spectro-electrochemistry.

The structure of the thesis does not strictly follow the numbering of the papers. Developed methods and new insights obtained from the different studies are summarized in topical chapters.

2. Preparation and Characterization of Dinuclear Functional Models of the [FeFe]-H_2ase Active Site

In this chapter the preparation and characterization of two new model complexes $Fe_2(dcbdt)(CO)_6$ (**1**, dcbdt = 1,4-dicarboxylbenzene-2,3-dithiolate) and $Fe_2(mcbdt)(CO)_6$ (**2**, mcbdt = 1-monocarboxylbenzene-2,3-dithiolate) of the [FeFe]-H_2ase active site are described (Scheme 2.1). In addition, complex $Fe_2(bdt)(CO)_6$ (**3**, bdt = 1,2-benzenedithiolate) that is used as a reference throughout the thesis will be presented. A detailed study on catalytic intermediates of photocatalytic proton reduction with **3** is also described in this chapter.

2.1 Introduction

More than 200 model complexes resembling structural features of the [FeFe]-H_2ase active site have been prepared within the last decades.[68,69] While in the beginning the challenge mainly lay in the preparation and characterization of organometallic complexes that were as accurate structural mimics of the active site as possible,[74,87,152,153] functional properties came more into focus later on.[81,93] In these studies, it became clear that the enzyme's activity could not be reproduced by simply mimicking the organometallic diiron center with its surrounding set of carbonyl, cyanide, and dithiolate ligands. A closer look into the protein structure[56,82] revealed interactions of the carbonyl and cyanide ligands with amino acid residues of the protein matrix that further fine-tune the active site's reactivity. It is only through these interactions that the enzymes function at high rates and low overpotential. From this observation it is clear that model complexes need to be integrated into larger systems which either control the rotational freedom of the complexes in solution or that are able to interact with the complex and thus mimic the outer shell in the protein.

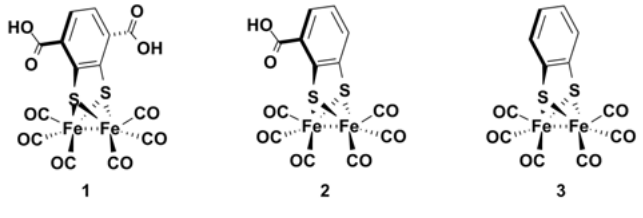

Scheme 2.1. [FeFe]-H_2ase active site mimics used in this thesis.

In our group and others,[70,72,81] complex **3** has been synthesized and extentially characterized. It is both a structural and a functional mimic of the [FeFe]-H_2ase active site and thus a good candidate for integration into larger systems. Throughout this thesis, **3** will be mainly used as a reference complex. In Paper I it is further used for the study and characterization of catalytic intermediates of photochemical hydrogen production schemes.

Two new model complexes **1** and **2** that are based on **3** but bear carboxylates were prepared in this thesis. The choice of carboxylates was motivated by the following:

1. Installation of carboxylates in ortho-position to the thiolates in the bridge of the complex does not significantly change its structure. Small changes of the electronic properties due to functionalization might occur, but will most likely not dramatically alter the reactivity.
2. Carboxylates can easily be functionalized by amines. Amide coupling was used in Paper II to extend the ligand framework, as well as in Paper IV for anchoring complex **2** into amino-functionalized MIL-101.
3. 1,4-benzene dicarboxylic acid (BDC) is a commonly used linker in MOFs and is a structural part of complex **1**. The latter could therefore be used in Paper III for incorporation into UiO-66.
4. Carboxylates can further serve as anchoring groups on surfaces. Complex **2** was used for sensitizing NiO and ZnO. These studies will not be further discussed in this thesis; the interested reader is referred to the respective papers.[52,154]

The two complexes **1** and **2** were characterized by single-crystal X-ray diffraction, ^{1}H-NMR, IR-spectroscopy, and electrochemistry. Furthermore, DFT calculations were used for the identification of reduced catalytic intermediates of complex **3** and to determine the reduction potentials of its first and second reduction.

2.2 Synthesis

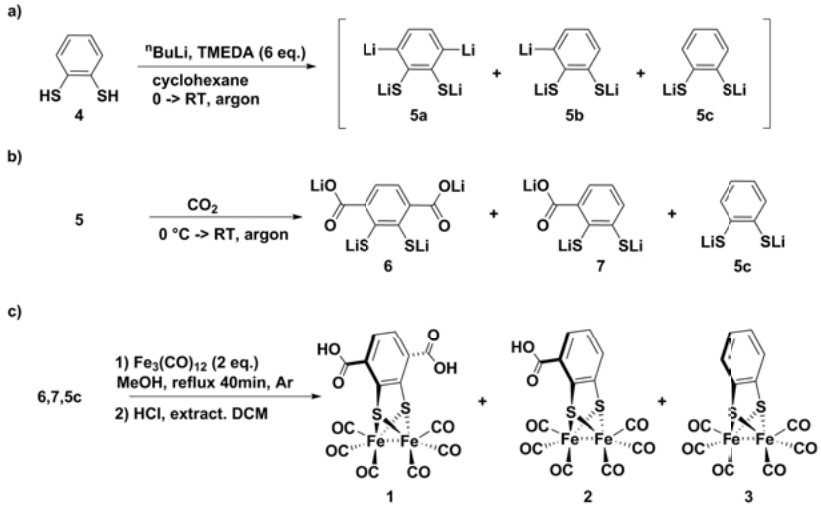

Scheme 2.2. Synthesis of the three [FeFe]-H_2ase active site mimics.

2.2.1 Preparation of **1** and **2**

The two ortho-functionalized carboxylate complexes **1** and **2** are prepared in a three step one-pot reaction starting with the lithiation of 1,2-benzene dithiol (**4**), followed by CO_2 insertion and finally complexation with $Fe_3(CO)_{12}$ (Scheme 2.2). The procedure is based on the work of Hahn and Sellmann,[155–157] with a few modifications. Addition of **4** to a mixture of *n*-butyllithium and TMEDA in excess at 0 °C followed by stirring at room temperature for 3 d are the best conditions to prepare the fourfold lithiated product (**5a**). Subsequently, CO_2 gas dried over P_2O_5 is led into the mixture at 0 °C. Since partial protonation of **5a** during the long reaction time cannot fully be prevented,[158] the first two steps yield a mixture of the di- and monocarboxy-ligands (**6** and **7**) as well as unfunctionalized starting material (**5c**), which are difficult to separate. Thus, complexation is done on the crude ligand mixture before acidification and resulting complexes can be readily separated by column chromatography. The final products are acidified with diluted HCl and extracted with Et_2O to obtain the carboxylic acids. Optimized yields of about 40 % for **1** and 30 % for **2** can be afforded with this procedure. About 10 % **3** is obtained as byproduct. If the reaction time of the lithiation is limited to 4 h, the yield for **2** can be increased to 60 %, but no **1** complex is afforded. Single crystals of **1** and **2** were prepared by two-layer crystallization with methanol:pentane in a ratio of 20:80 at ambient temperature under inert gas. Crystal structures are very similar to **3** and other model complexes reported in literature.[72] The complexes feature the characteristic butterfly structure with all CO ligands in terminal positions (Figure 2.1). All three complexes are used in the various projects discussed in

this thesis. Later on, Fei and Cohen developed an alternative strategy to produce the dicarboxylate dithiolate ligand from the corresponding dicarboxylate catechol, based on a Newman-Kwart rearrangement.[159]

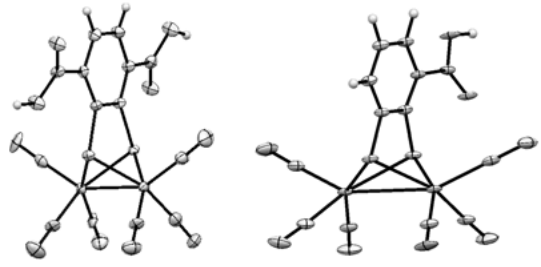

Figure 2.1. ORTEP plots of **1** and **2** (probability level 50 %). Data were collected by Dr. Andreas Orthaber.

2.2.2 Amide Coupling

The reactivity of the two carboxylate complexes **1** and **2** towards amines was investigated in order to evaluate further functionalization. Two strategies for amide coupling were tested:
The first route relies on activation of the acid functionality to an acyl chloride which is subsequently reacted with amines. For acid chloride formation, two different reagents, oxalylchloride and thionyl chloride, were tested. Using oxalylchloride, the acyl chloride product could be obtained in good yields and characterized by IR spectroscopy. Thionyl chloride did not work for the reaction, most likely due to decomposition of the complex. The second step, reacting the acyl chloride with amines was unsuccessful. A number of reaction conditions were tested without success including different solvents (THF and dioxane), reaction time (2 – 30 h) and temperature (24 – 66 °C).

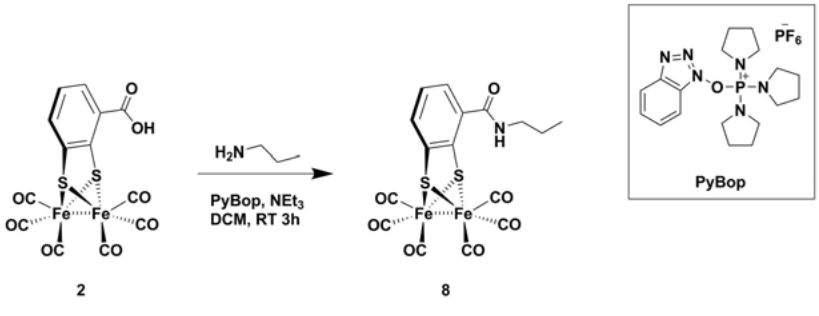

Scheme 2.3. Amide coupling using PyBop as coupling reagent.

The second route employs the amide coupling reagent PyBop (benzotriazol-1-yl-oxytripyrrolidinophosphonium hexafluorophosphate). This reaction can

be performed in common solvents (e.g. DCM), proceeds at room temperature for 2 – 3 h, and affords the product in decent yields. Scheme 2.3 shows an example for the reaction. Installation of a range of amines on complex **2** works very well, including branched amines and the bulkier amino-phosphine-ligands used in Paper II. Also complex **3** could be functionalized by this procedure.

2.3 Characterization

2.3.1 IR Frequencies

IR spectra of the three complexes were recorded in MeCN solutions. Since **1** is not very well soluble in MeCN, the three spectra in Figure 2.2 are normalized to the largest absorption band. The spectra show the ν_{CO} stretching frequencies for the three complexes. They are all very similar in shape and wavenumber (Table 2.1) and only small shifts towards higher frequencies are observed for complexes **1** and **2** compared to the reference **3**. The reason for the small shift is the electron withdrawing effect of the carboxylate groups leaving less electron density in the diiron center of the complexes. Less electron density causes a weaker backdonation from iron to the antibonding π^*–orbitals of CO ligands, which is reflected by higher wavenumbers.

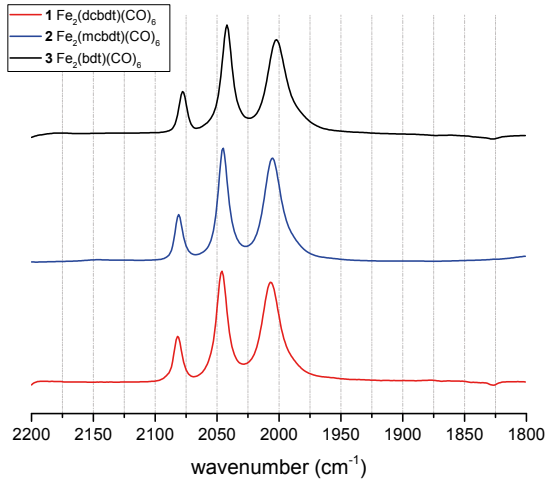

Figure 2.2. Normalized IR spectra of the three complexes.

Table 2.1. *ν_{CO} frequencies of the three complexes recorded in MeCN.*

complex	IR frequencies (cm^{-1}) in MeCN
1	2082, 2046, 2007
2	2081, 2045, 2005
3	2078, 2042, 2002

2.3.2 Electrochemistry

Complex **3** undergoes a reversible two-electron reduction with a half-wave potential of $E_{1/2} = -1.32$ V vs. ferrocene in MeCN.[81] The relatively low reduction potential of this complex compared to e.g. the pdt-bridged analog is explained by electronic communication between the bdt bridge and the diiron center. Delocalization of electron density between the two minimizes the energy needed for reduction of the complex. The reduction is a two-electron process as a result of inverted potentials of the $Fe_2^{0/-}$ and $Fe_2^{-/2-}$ redox couples. In other words, the second reduction is thermodynamically more favored than the first, giving rise to an overal two-electron reduction that is observed in the CV. Until our study in Paper I the two-electron reduction could not be separated experimentally. Using DFT, we calculated individual reduction potentials for the first and second reduction of $E_1 = -1.42$ V and $E_2 = -1.21$ V vs. ferrocene in MeCN, giving an average potential close the the experimentally observed one.

Reduction potentials versus the ferrocene/ferrocenium redox couple were calculated as the sum of the Gibbs free energy differences according to the thermochemical cycle depicted in Scheme 2.4.

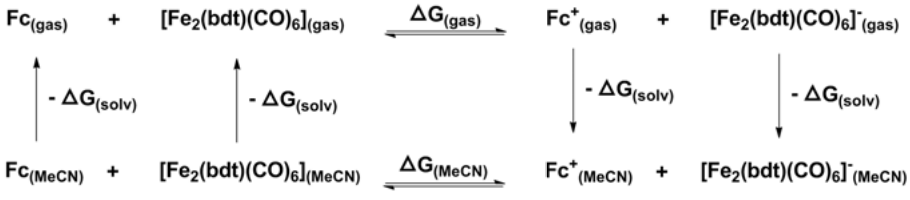

$$\Delta G_{(MeCN)} = \Delta G_{(gas)} + \Delta\Delta G_{(solv)}$$

$$\Delta G_{(gas)} = G(Fc^+)_{(gas)} + G([Fe_2(bdt)(CO)_6]^-)_{(gas)} - G(Fc)_{(gas)} - G([Fe_2(bdt)(CO)_6])_{(gas)}$$

$$\Delta\Delta G_{(solv)} = \Delta G(Fc^+)_{(solv)} + \Delta G([Fe_2(bdt)(CO)_6]^-)_{(solv)} - \Delta G(Fc)_{(solv)} - \Delta G([Fe_2(bdt)(CO)_6])_{(solv)}$$

Scheme 2.4. Thermochemical cycle for calculation of reduction potentials ($E^\circ = \Delta G/F$). Fc = ferrocene

Cyclic voltammograms of all complexes **1-3** (1 mM solutions) were recorded in different solvents with $TBAPF_6$ (0.1 M) as electrolyte and the observed re-

duction potentials are summarized in Table 2.2. The data are referenced against ferrocene/ferrocenium.

1 and **2** show different electrochemical behavior than the reference complex **3**; the carboxylates disturb the reversibility of reduction in MeCN. **2** shows a relatively large peak separation between the reduction ($E_{p,c} = -1.35$ V) and the oxidation peaks ($E_{p,a} = -1.02$ V) (Figure 2.3 c)). Both occur at less negative potentials than those in the reference **3**, which is attributed to the electron withdrawing effect of the carboxylate groups. This shift is also consistent with the shift in IR absorption bands described before. Converting the carboxylate to an amine affords the complex $Fe_2(mabdt)(CO)_6$ (**8**, mabdt = 1-monoamide-2,3-benzenedithiolate). The reduction of **8** is chemically reversible, which is shown by equal cathodic and anodic peak currents (Figure 2.3 d)). The large peak separation for **8** compared to **3**, however indicates that the reduction is electrochemically not fully reversible.

1 is not soluble enough in MeCN. Therefore a mixture of MeCN/MeOH (2:1) was used to record the CV (Figure 2.3 b)) and the complex gets reduced irreversibly at $E_{p,c} = -1.56$ V. Addition of MeOH does not affect the reduction of **3**; in the same solvent mixture the complex shows unchanged behavior compared to the CV recorded in pure MeCN (Figure 2.3 a)).[160] In DMF the reduction of **1** is chemically reversible (Figure 2.3 e)), however with a larger peak separation than expected for electrochemical reversibility.

Table 2.2. *Reduction potentials of the different complexes.*

complex	$E_{p,c}$	$E_{p,a}$	solvent
3	−1.37 V	−1.26 V	MeCN/MeOH 2:1
1	−1.56 V	−1.36 V −0.77 V	MeCN/MeOH 2:1
2	−1.35 V	−1.02 V	MeCN
8	−1.38 V	−1.05 V	MeCN
1	−1.35 V	−1.10 V	DMF

2.4 Key Catalytic Intermediates of **3**

In Paper I, a combined study of time-resolved spectroscopy and DFT was performed to reveal the identity of the singly-reduced species. As mentioned before, complex **3** usually undergoes a two-electron reduction due to the inverted reduction potentials. This means that the second reduction occurs at lower potential than the first one and a structural rearrangement was suggested to be the reason for this phenomenon.[81] The molecular structure of the singly-reduced state $\mathbf{3}^-$ had prior to our investigation only been proposed on grounds of theoretical work. Our aim was to investigate this first intermediate using time-resolved infrared-transient absorption spectroscopy as experimental tool in combination with theoretical analysis by DFT.

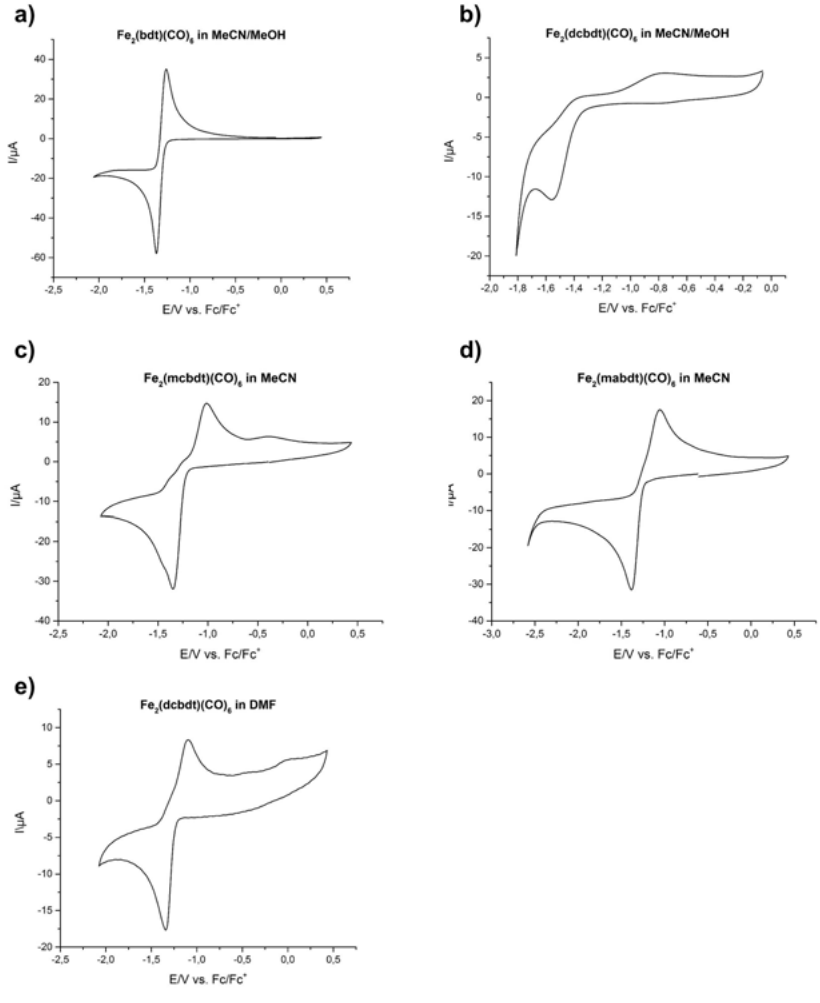

Figure 2.3. Cyclic voltammograms **a) 3** (1 mM) and **b) 1** (1 mM) recorded in MeCN/MeOH 2:1 mixture. **c) 2** (1 mM) and **d) 8** (1 mM) recorded in MeCN and **e) 1** (1 mM) recorded in DMF. In all samples, 0.1 M $TBAPF_6$ was present as electrolyte, the scan rates were 100 mV s^{-1} and all spectra are referenced against the ferrocene/ferrocenium redox couple.

As mentioned before, electrochemical reduction produced exclusively the doubly-reduced complex. Figure 2.4 a) shows the IR spectrum for this reduction obtained by spectro-electrochemistry. A frequency shift of about 120 $cm^{-1}$to lower wavenumbers compared to the groundstate characterizes this species. In order to separate the two reduction steps, time-resolved transient absorption spectroscopy was used. In this system, a photosensitizer (ruthenium-tris-(dimethylbipyridine)) is excited by a laser pulse, reductively quenched by a sacrificial electron donor (tetrathiafulvene, TTF) and the reduced sensitizer transfers selectively one electron to the catalyst, which is also present in solution. This process happens 1 – 2 μs after excitation and the reaction product – the singly-reduced catalyst – can be detected and characterized by recording IR spectra at this time (Figure 2.4 b)).

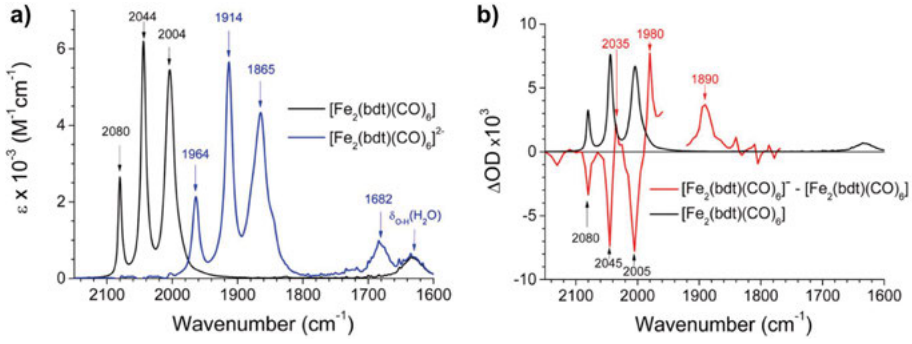

Figure 2.4. IR spectra of a) doubly-reduced $\mathbf{3}^{2-}$ recorded with spectro-electrochemistry and b) singly-reduced $\mathbf{3}^{-}$ obtained from transient absorption spectroscopy. Reprinted with permission from reference [160]. Copyright © 2014.

The resulting IR spectrum is then compared to the spectra obtained from DFT calculations of different possible geometry optimized structures. In literature, a structure with a bridging carbonyl ligand and one broken Fe-S bond had been proposed prior to this study.[81] The same was also found as possible candidate in our own analysis. In addition, a structure was found in which all CO ligands remain in a terminal position, while one Fe-S bond breaks (Figure 2.5). In fact, this structure showed to be a few kJ/mol lower in energy than the first one. Direct comparison with the experimental IR spectrum proved that the latter structure is a better fit, as no IR absorption band for a bridging CO was observed in the experimental data.

Next, protonation of the singly-reduced species was tested experimentally. For this, the singly-reduced species was generated in presence of different acids and an acid strength of the protonated and reduced complex between $9 \leq pK_a \leq 11$ was estimated. The protonation results in a shift in the IR spectrum back to higher wavenumbers, which is well in accordance with the calculated values for the complex with a bridging hydride.

Scheme 2.5 gives an overview over the different intermediates that have been investigated in this project.

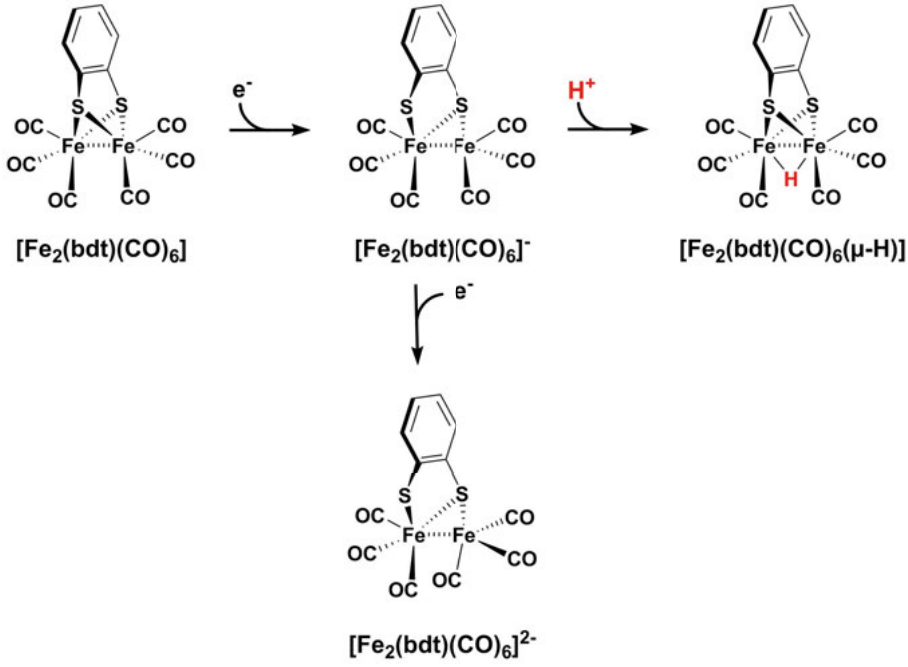

Scheme 2.5. Key intermediates of **3**. After the first reduction, $\mathbf{3}^-$ was either be protonated or reduced again.

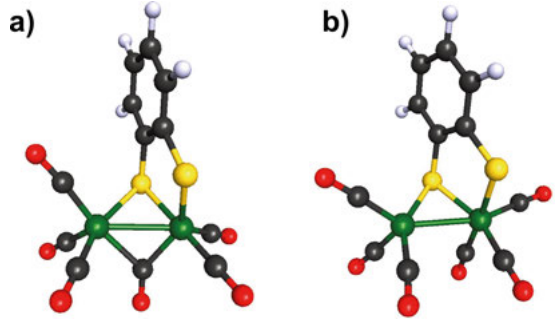

Figure 2.5. Geometry optimized structures of a) singly-reduced $\mathbf{3}^-$ with bridging CO and b) lower energy structure of $\mathbf{3}^-$ with all terminal CO. Reprinted with permission from reference [160]. Copyright © 2014.

Table 2.3. *Computed IR vibrational frequencies (in gas phase) compared to experimental data (in MeCN). Given are the resulting maxima of overlapping computed bands. No scaling was applied to computed frequencies.*

Ox. state	exp. / cm^{-1}	calc. /cm^{-1}
$Fe_2(bdt)(CO)_6$	2080, 2044, 2004	2064, 2033, 1997
$Fe_2(bdt)(CO)_6^-$	2035, 1980, 1890	2012, 1960, 1908
$Fe_2(bdt)(\mu{-}CO)(CO)_5^-$	n.d.	1997, 1960, 1934, 1793
$Fe_2(bdt)(CO)_6^{-2}$	1964, 1914, 1865, 1682	1939, 1903, 1861, 1725

2.5 Summary and Conclusion

In conclusion, two new model complexes for the [FeFe]-H_2ase active site containing carboxylate groups have been prepared and characterized. They are electronically relatively similar to their parent complex without carboxylate in the bdt linker as shown by IR spectroscopy. In MeCN, the new complexes feature irreversible electrochemical reductions in contrast to the parent complex **3**. Covering them with small amide functions or working in DMF improves chemical reversibility during the redox process. It can thus be assumed that the electrochemical behavior of both complexes when incorporated into MOFs or bound on surfaces is similar to the parent complex. In the following chapters of this thesis, the complexes will be used for the functionalization of MOFs. Complex **2** will further be used in chapter 3 to tether phosphine ligands to the bridging ligands.

3. Restricted Rotation in Biomimetic Molecular Model Complexes of the [FeFe]-H_2ase Active Site

In this chapter, a new series of [FeFe]-H_2ase active site model complexes is prepared, containing tethering phosphine ligands that are covalenty attached to the bridging dithiolate ligand (Paper II). Monofunctionalized complex **2** serves as precursor for the new complexes. Together with synthesis and characterization, a theoretical investigation of effects on the rotational energy barriers of the $Fe(CO)_2(PL_3)$-subunit resulting from tethering ligands is presented.

3.1 Introduction

As mentioned before, [FeFe]-H_2ase enzymes are among the most powerful catalysts for conversion of protons into molecular hydrogen. Figure 3.1 depicts the active site and its coordination spheres. One of the CO ligands occupies a bridging position between the two iron centers, leaving an open coordination site at Fe_d, i.e. the iron that is distal to the [4Fe4S] cluster. This so-called *rotated structure* is stabilized by interactions with the amino acid residues.[64,82] Thus, it is clear that the surrounding protein matrix plays a crucial role for the enzyme's activity.

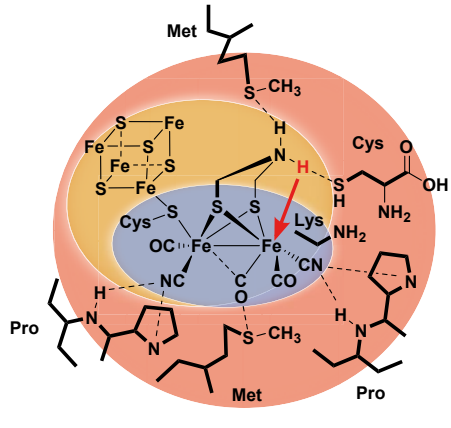

Figure 3.1. Three coordination spheres around the [FeFe]-H_2ase active site. The proton coming in during the catalytic cycle is highlighted in red.

Molecular model complexes of the [FeFe]-H_2ase active site usually lack these interactions since their structral simplicity does not allow to include such effects. Therefore all CO ligands and their substitutes (e.g. phosphine ligands or CN^-) are located in terminal positions since the *relaxed* or *eclipsed structure* is thermodynamically favored over the rotated structure with a bridging CO ligand. Consequently, there is no open coordination site present as on Fe_d in the enzyme.[69] In the enzyme, terminal hydrides are generated at the open coordination site and rapidly react further with another proton to form molecular hydrogen. In a theoretical study Hall and coworkers suggested that molecular model complexes could indeed form terminal hydrides.[65] By DFT calculations they showed that the first protonation on their model complex forms a terminal hydride that rapidly transforms into the thermodynamically more stable bridging hydride.

On the synthetic front, efforts have been made in order to stabilize terminal hydrides in model complexes.[83,84,161–163]

In the model complexes, spectroscopic characterization of terminal hydrides was achieved by introducing bulky, chelating phosphine ligands that could make the diiron center basic enough for rapid protonation and that could stabilize the terminal hydride temporarily. However, these intermediates are only observed at low temperatures. At room temperature they transform rather quickly into the thermodynamically favored bridging hydride. The structural rearrangement necessary for the conversion of a terminal into a bridging hydride is essentially a rotation of the $Fe(CO)_2(PL_3)$-subunit by 60° (Figure 3.6).

In this chapter, the design of a new series of model complexes containing tethered phosphine ligands will be described. The phosphine ligand contains a carbon chain that is attached to the bdt bridge by an amide bond. Thereby, the phosphines are not just coordinating to the iron center; they are also covalently linked to the bdt bridge to obtain a more rigid structure. Through this tethering effect, the rotation of the $Fe(CO)_2(PL_3)$-subunit is attempted to be hindered. The hypothesis is that structural rearrangements of the complex after protonation could potentially be prevented or at least drastically slowed down as compared to the situation in previous model complexes.

Scheme 3.1 presents the proposed series of model complexes with three different tethering ligands and an electronically comparable reference compound with a similar set of ligands. In Paper II the synthesis and characterization of these complexes is described and complemented with a detailed DFT study on rotation energy barriers achieved by the tethering effect.

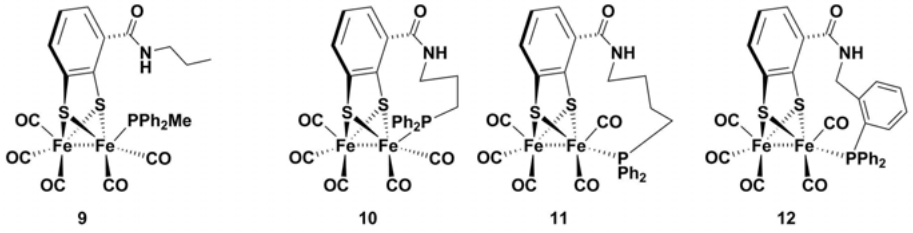

Scheme 3.1. Series of model complexes with tethered phosphine ligands.

3.2 Experimental Part

3.2.1 Synthesis

Scheme 3.2 provides an overview over the synthesis of the propyl-tethered complex (**10**) as an example. Briefly, starting with **2**, the amine-phosphine ligand is coupled by the peptide linking reagent PyBop to the carboxylic acid on the bridging dithiolate ligand. Continuous stirring for about 5 h at room temperature (complex **10** and **11**) leads to substitution of one carbonyl ligand at the iron center. In case of the aromatic tethered complex **12**, refluxing the reaction mixture for 12 h leads to partial formation of the product as indicated by IR. Due to the steric bulk of this ligand, full conversion was impossible. The anticipated by-product is the hexacarbonyl complex where the phosphine ligand is connected via the amide to the bridge without coordination to the iron center. It has not been possible to fully isolate the target complex with coordinated phosphine from this by-product. Reference compound **9** was synthesized in two steps, starting with amide coupling of propylamine to the carboxylic acid and subsequent ligand exchange. In order to selectively introduce only one $P(Ph)_2Me$ ligand, one equivalent Me_3NO as decarbonylation reagent was added to the reaction. All complexes where characterized by IR, ^{31}P-NMR and complexes **9** and **10** with HR-MS.

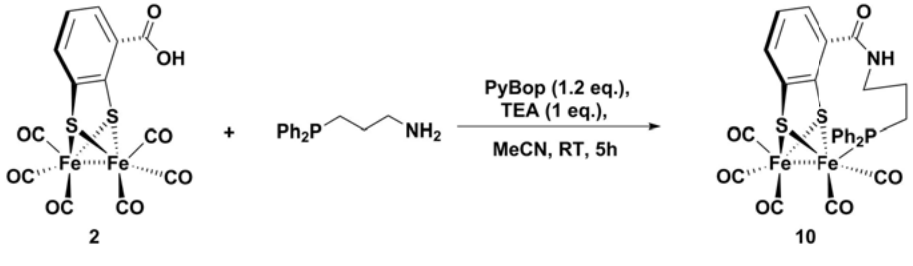

Scheme 3.2. Synthesis of the propyl-tethered complex.

3.2.2 IR Absorption Spectroscopy

Coordination of the tethered phosphine ligands is clearly indicated by a shift of the ν_{CO} stretching frequencies by about 30 cm^{-1} to lower wavenumbers. Figure 3.2 shows an overview over the IR spectra for all complexes **9-12** together with the precursor complex **2**. Table 3.1 summarizes all ν_{CO} stretching frequencies.

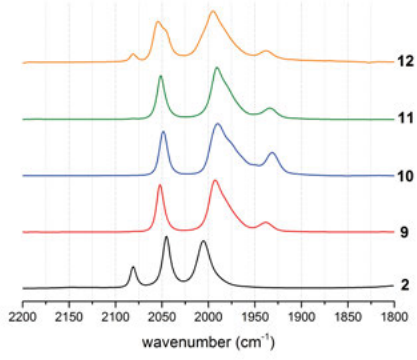

Figure 3.2. IR spectra of the synthesized complexes. All spectra were recorded in MeCN.

Table 3.1. *ν_{CO} stretching frequencies of **2** and **9-12** and corresponding calculated values.*

Compound	ν_{CO} (cm^{-1})	calculated
2	2081, 2045, 2005	2061, 2030, 1998
9	2052, 1993 (broad), 1938	2037, 1984, 1939
10	2048, 1989 (broad), 1931	2039, 1986, (1965), 1930
11	2051, 1992 (broad), 1934	2035, 1989, (1975), 1933
12	2081 (small), 2055, 1996 (broad), 1938	n.d.

3.3 DFT Calculations

Gas phase geometry optimizations were conducted with the BP-86 functional in combination with the def2-TZVP basis set for all different substitution isomers in order to identify the thermodynamically most favored structures. This method has been shown to yield accurate data for the precursor complex **2** compared with the crystal structure. All optimized structures were minima as indicated by vibrational frequency analysis. In addition, calculations were also performed with B3-LYP/def2-TZVP.

3.3.1 Vibrational Frequency Analysis

Vibrational frequency analysis was performed and the results compared to experimental data in order to obtain information about which structural isomer was formed. In general, the calculated data fit very well to the experimental data in number of absorption bands and shift of the wavenumber. In the structure of **2**, on each iron atom there are two basal CO ligands in plane with the two sulfurs and iron. The apical CO is the ligand pointing out of the plane (see structures in Figure 3.5). The phosphine in complexes **9-11** can either substitute an apical or a basal CO ligand. Comparison of the calculated IR spectra of **9**, **10**, and **11** with the experimental spectra (Figure 3.3 and Table 3.1), suggests that both apical and basal isomer are present in equillibrium. The spectra presented are therefore 1:1 mixtures of the calculated spectra obtained for the apical and the basal isomers.

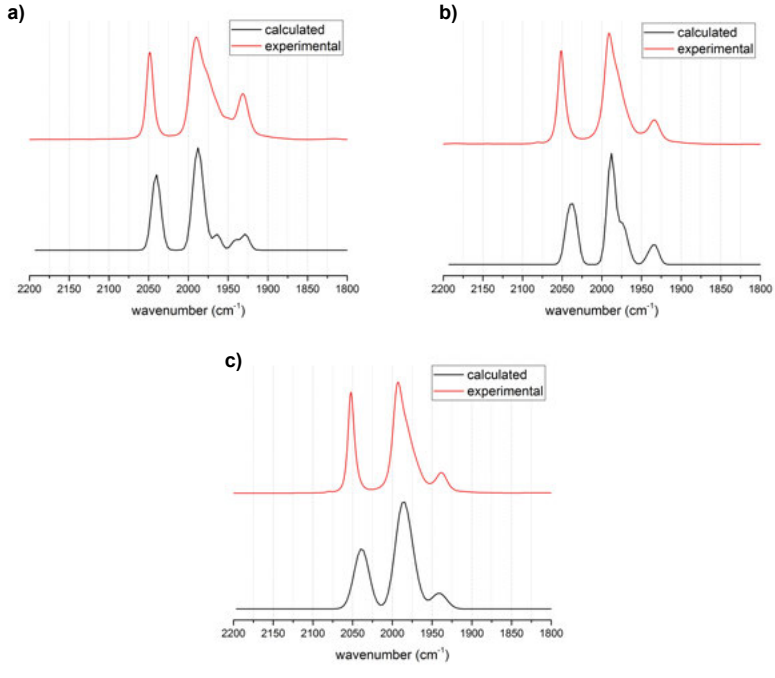

Figure 3.3. Comparison of calculated (black) and experimental (red) spectra of a) complex **10**, b) complex **11**, and c) complex **9**. The calculated spectra are obtained from vibrational frequency analysis using BP-86 without scaling factor. Spectra of apical and basal isomers are mixed in a ratio of 1:1.

3.3.2 Lowest Energy Isomers

In addition to the synthetically derived complexes **9-12**, the computational analysis of the series was complemented by ethyl- (**13**) and pentyl-tethered (**14**) analogs. Geometry optimized structures for the whole series with increasing chainlength from 2-5 carbon atoms were investigated (Figure 3.4). For computational efficiency, the PMe_2 analogs were used, as they gave very similar results (isomer preference and IR spectra) compared to the PPh_2 complexes **10** and **11**. In the following, the PMe_2-substituted structures will be denoted as **9b**, **10b**, and **11b**.

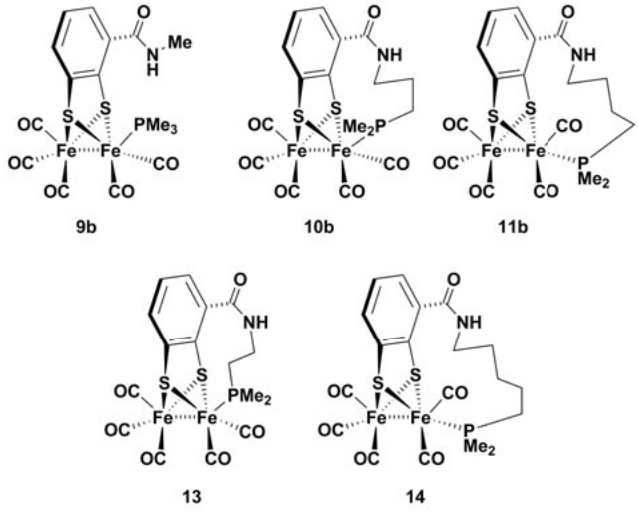

Figure 3.4. Calculated structures for comparison of lowest energy isomers.

Figure 3.5 shows the two different structural isomers for complex **10b** as an example. The apical isomer is lower in energy due to less strain caused by the propyl-chain in this form compared to the basal isomer. For complex **13** an optimized structure was only found for the apical isomer; the basal structure is not existent since the carbon chain between N and P is too short. For complex **14**, both structures were found.

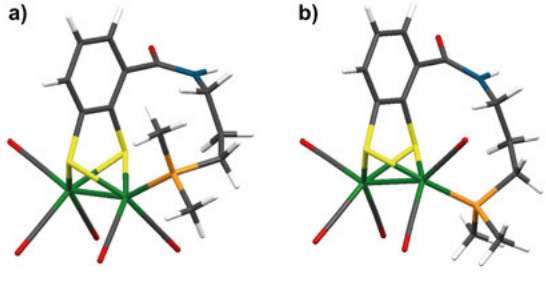

Figure 3.5. Geometry optimized structures of **10b** a) apical and b) basal.

Table 3.2 provides an overview over calculated differences in energy for all geometry optimized structures. There appears to be no trend in preferred structure (apical versus basal) aligned with increased chainlength. While **10b** and **14** have lower energy apical structures, the basal form is preferred for complex **11b**. The reason for this is differently strong strain caused by the carbon chains. The higher strain in the propyl chain in the basal isomer of **10b** is the reason for the apical isomer being favored. In **14**, the chain becomes sterically demanding and still prefers the apical isomer, while the butyl chain in **11b** causes less strain for the basal form.

Table 3.2. *Lowest energes (ΔE = E(apical) - E(basal)) between apical and basal forms of all calculated complexes.*

Complex	BP86 (kJ mol^{-1})	B3-LYP (kJ mol^{-1})
9b	-3.0	-7.7
10b	-5.6	-12.8
11b	11.0	8.2
13	n.d.	n.d.
14	-9.4	-14.9

3.3.3 Transition States

Energy barriers for the rotation of the $Fe(CO)_2(PL_3)$-subunit were calculated by a transition state search. The transition state is resulting from the movemement of the phosphine ligand from an apical to a basal position. In the literature, for the hexacarbonyl complex a 60° rotation of the three ligands is suggested for this rearrangement, whereby one of the carbonyl ligands moves to a semi-bridging position (top in Figure 3.6).[164] This structure was used as a starting point and transition states were calculated for **2**, **9b**,**10b**, and **11b**. All optimized structures were identified as transition states containing only one imaginary frequency in the vibrational frequency analysis corresponding to the concerted rotation of the $Fe(CO)_2(PL_3)$-subunit. The transition state of **9b** is the only exception. Two additional imaginary frequencies were found in the transition state structure that were located at the amide in the bridging ligand. These could not be removed yet and therefore, only preliminary values are given for this compound. Figure 3.6 shows the energy profile for rotation in complex **10b** as an example. Interestingly, this complex yields the highest energy barrier for the rotation. This can be explained by a higher strain of the 3 carbon chain compared to the 4 carbon chain in complex **11b** and compared to the non-linked ligands in complexes **2** and **9b** that can rotate more freely.

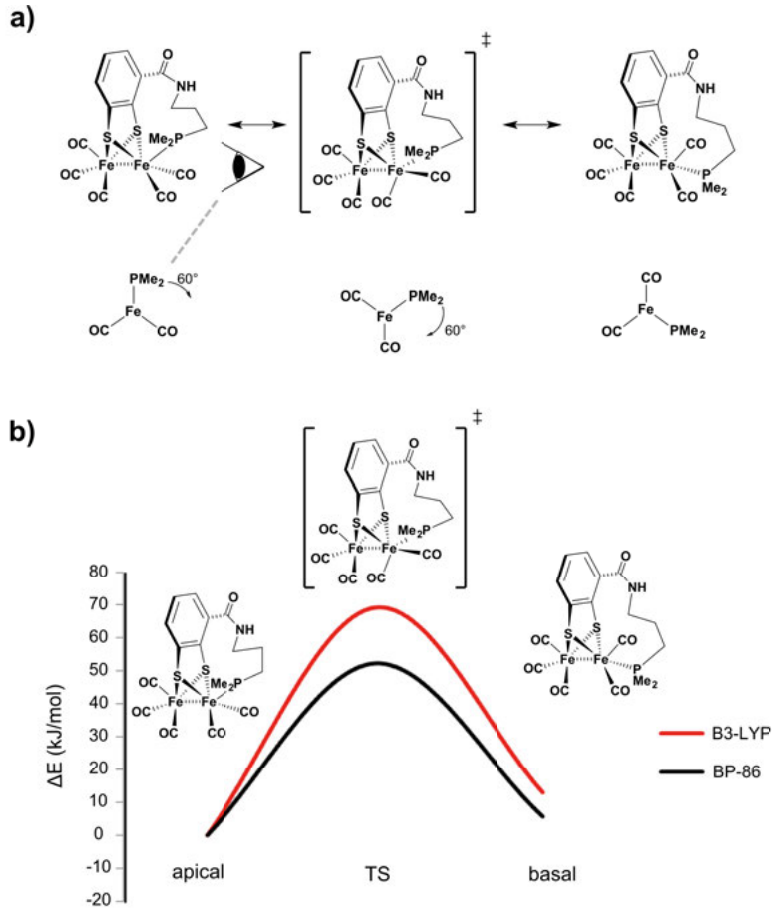

Figure 3.6. a) Rotation of the $Fe(CO)_2(PL_3)$-subunit from apical via transition state (TS) to basal conformation. b) Energy profile for complex **10b**.

Table 3.3. *Calculated energy differences (*$kJ\,mol^{-1}$*) between the apical and basal starting states and the found transition states. For* ***9b*** *preliminary data are given.*

method	**2**	**9b**	**10b**	**11b**
apical-TS (BP86)	26.56	33.08	52.18	23.49
basal-TS (BP86)	26.56	35.44	46.52	34.61

3.4 Summary and Conclusion

In this chapter, three new model complexes of the [FeFe]-H_2ase active site have been synthesized and characterized. Two of them contain a tethering ligand with chainlength of 3 and 4 carbon atoms, the third is a reference compound electronically similar but lacking the link between bdt-bridge and iron center. The complexes have been characterized by IR absorption spectroscopy as well as ^{31}P-NMR and HR-MS.

A theoretical investigation employing DFT revealed that both the apical and the basal isomers exist in equillibrium as comparison of experimental IR spectra with calculated data showed. In a more detailed study, two additional complexes with 2 and 5 carbon atoms in the chain were investigated in order to identify the effect of the chain length on the lowest energy of apical vs. basal isomers. For this, the PMe_2 analogs of the synthetic complexes were used. The complex with a chain-length of 4 carbon atoms prefers the basal conformation, while all other structures show lower energies for the apical isomers. For the shortest carbon chain (ethyl), only the apical isomer was found, since the chain was too short for the phosphine to reach the basal position.

To study the effect of tethering ligands on the rotation of the $Fe(CO)_2(PL_3)$-subunit, a transition state search was performed on the complexes with 3 (**10b**) and 4 (**11b**) carbon atoms in the chain. Both the hexacarbonyl complex **2** and the phosphine-substituted non-linked complex **9b** were used as references. The propyl-tethered complex **10b** yielded the highest energy barrier of all structures and is thus the most promising candidate for investigating protonation and the formation of a terminal hydride. Restricting the rotational freedom of the complex can potentially lead to the stabilization of the reactive terminal hydride, which is considered to be an important intermediate in the catalytic cycle. Experimental studies on the protonation of **10** should be done in future in order to confirm this hypothesis.

4. Enhanced Photochemical Hydrogen Production with [FeFe]-H_2ase Active Site Model Complexes by Incorporating them into Metal-Organic Frameworks

In this chapter the incorporation of $Fe_2(dcbdt)(CO)_6$ **1** and $Fe_2(mcbdt)(CO)_6$ **2** into two different MOFs and a detailed structural and functional study of the resulting systems will be described. Since the complexes are thermally unstable and do no withstand the harsh conditions of solvothermal MOF synthesis (e.g. high temperature), alternative methods had to be used. In the first project presented (Paper III), post-synthetic linker exchange in UiO-66 with complex **1** is used for incorporation. In the second, MIL-101 is modified post-synthetically in order to introduce complex **2** (Paper IV). Photochemical hydrogen production with both resulting MOF-catalyst systems is described.

4.1 Introduction

In the previous chapter, a series of tethered phosphine ligands was installed on [FeFe]-H_2ase active site model complex **2**, in order to mimic the interaction of the protein matrix with cyanide ligands in the structure of the natural enzyme.[64] In a theoretical study an increased rotational barrier was observed for the tethered complexes compared to the reference, indicating restricted rotation. The focus of the current chapter lies on the placement of both model complexes **1** and **2** into a defined environment, similar to the pocket the [FeFe]-H_2ase active site is sitting in.[82] MOFs represent in several ways an ideal platform for incorporating organometallic complexes:[165]

1. Like enzymes, MOFs feature defined pores and channels that can host and deliver substrates of specific size.
2. The organic-inorganic hybrid nature of MOFs allows for tunability of their structure by changing type and connectivity of metal clusters involved and (post-synthetic) functionalization of the organic linkers.
3. MOFs provide a pocket of defined size and a specific chemical environment around the active catalysts that could potentially stabilize reactive intermediates.

4. Furthermore, higher coordination sphere effects could be studied by introducing additional functionalities to the framework (e.g. proton relays).

In Paper III, complex **1** is introduced into UiO-66 by post-synthetic linker exchange (PSE). Paper IV presents post-synthetic modification (PSM) as alternative strategy to functionalize MIL-101 with complex **2** via amide coupling. In both papers, the resulting materials are extensively characterized by PXRD, SEM, EXAFS, IR spectroscopy, and other techniques in order to confirm structural integrity of the complexes as well as of the MOFs. In addition, a functional study on photochemical hydrogen production for each of the systems is presented.

4.2 Post-Synthetic Linker Exchange in UiO-66

4.2.1 Preparation of UiO-66-**1**

Post-synthetic linker exchange (PSE), also referred to as solvent-assisted linker exchange (SALE), is a strategy to introduce new functionalities to the MOF by taking advantage of matching linker sizes.[166] This phenomenon has been observed for a number of highly robust and water-stable MOFs such as UiO-66, MIL-53 and ZIFs.[167–169] The process relies on solvent assisted de-coordination of the precursor linker and exchange with the new linker that is present in high concentration in the surrounding solution. The great advantage of this procedure is that thermally unstable linkers, which cannot be introduced directly during solvothermal synthesis, are readily incorporated post-synthetically into the framework.

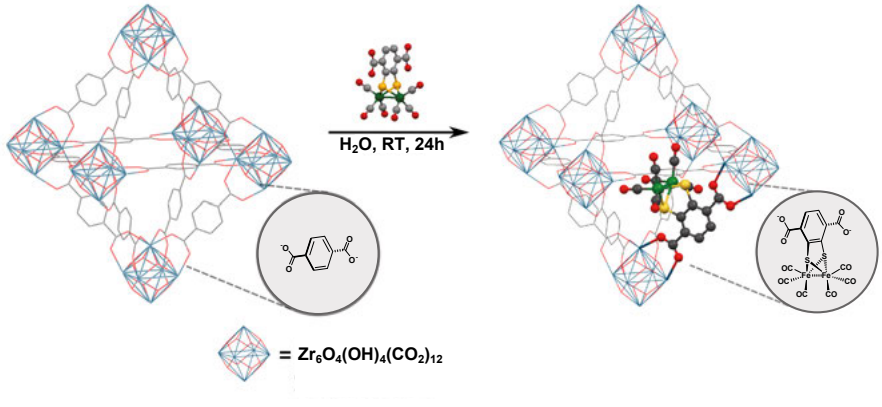

Figure 4.1. Post-synthetic linker exchange on UiO-66 with **1**.

Using this strategy, complex **1** was introduced successfully into UiO-66(Zr) (Figure 4.1). Briefly, a concentrated solution of **1** in water was added to the MOF and the suspension was sonicated for 10 min in order to disperse the MOF particles. Then the reaction vessel was placed on a shaker for 24 h at room temperature. After extensive washing with MeOH until the liquid layer remained clear, the sample was left to soak in MeOH for 3 d, while the solvent was exchanged every 24 h. The degree of exchange in the resulting UiO-66-**1** was determined to be 14 % by a combination of ^{1}H-NMR of the digested sample and EDX-analysis. The MOF structure remained unchanged after functionalization with complex **1** as indicated by SEM (Figure 4.2) and PXRD (Figure 4.3 a)). Structural integrity of the complex after incorporation was confirmed by IR and EXAFS (extended X-ray absorption fine spectroscopy – Figure 4.3 b) and Figure 4.4).

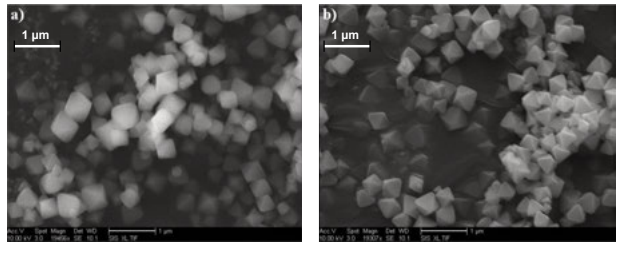

Figure 4.2. SEM images of a) blank UiO-66 and b) UiO-66-**1**. Reprinted with permission from reference[170] Copyright ©2013.

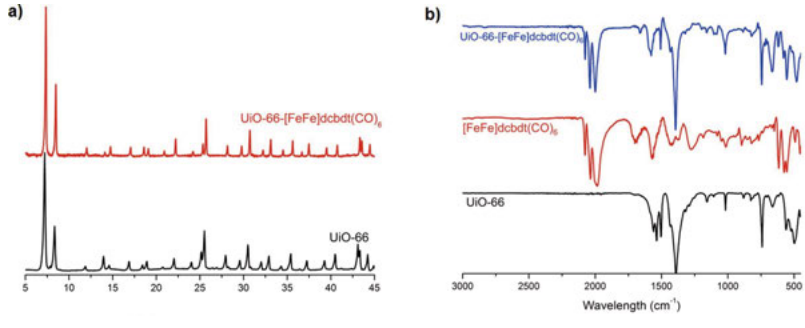

Figure 4.3. a) PXRD pattern of the UiO-66 before (black) and after (red) incorporation of **1**. b) IR spectra of homogenous complex **1** (blue), blank UiO-66 (black), and UiO-66-**1** (red). Reprinted with permission from reference [170]. Copyright © 2013.

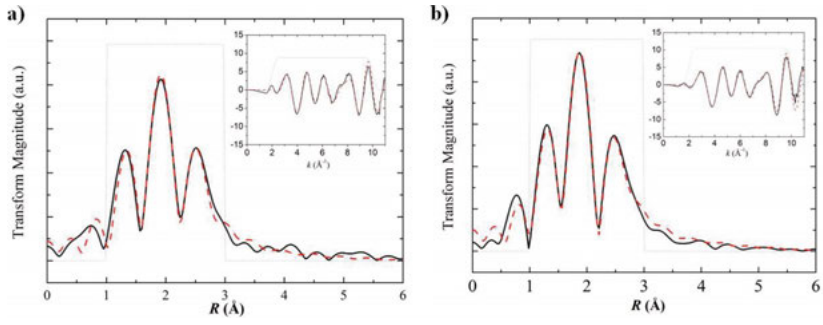

Figure 4.4. EXAFS of a) **1** and b) UiO-66-**1**. Reprinted with permission from reference [170]. Copyright © 2013.

In order to proof a true PSE process, UiO-66 was added to a solution of complex **3** that is lacking the two carboxylates, and treated under the same conditions as described for PSE above. After wasing the material, no ν_{CO} bands were observed in the IR spectrum. This is a clear indication that the complex is not just trapped in the pores.

4.2.2 Photochemical Hydrogen Production with UiO-66-**1**

In order to test the functionality of UiO-66-**1**, photochemical hydrogen production was carried out and compared to the homogenous complex **1** using the same catalyst concentration. The MOF-catalyst was suspended in aqueous acetate buffer at pH 5 with $Ru(bpy)_3Cl_2$ as photosensitizer and ascorbate as sacrificial electron donor. The suspension was placed inside a reaction vessel attached to a solid state hydrogen sensor and irradiated with a blue LED (475 nm) for 3 h. Figure 4.5 shows the amount of hydrogen produced over time. For UiO-66-**1** (blue), about 3 μmol hydrogen were produced after 2 h. After that, hydrogen production increases only very slowly. In contrast, the mixture with homogenous catalyst **1** (red) produced only 1 μmol hydrogen. From literature it is known, that irradiation of $(Fe)_2(bdt{-}Cl_2)(CO)_6$, an analog of **1**, leads to destruction of the complex after 20 min.[93] The same was observed in the present case: Hydrogen formation by **1** in solution ceases after less than 20 min and no more hydrogen is produced afterwards. Furthermore, recording an IR spectrum of the solution after the experiment does not show any remaining ν_{CO} frequencies. The recovered UiO-66-**1** on the other hand still contains a large amount of intact catalyst as shown by IR spectroscopy (Figure 4.5 b)). Experiments with blank UiO-66 (black) or no catalyst at all (grey) did not yield any formation of hydrogen.

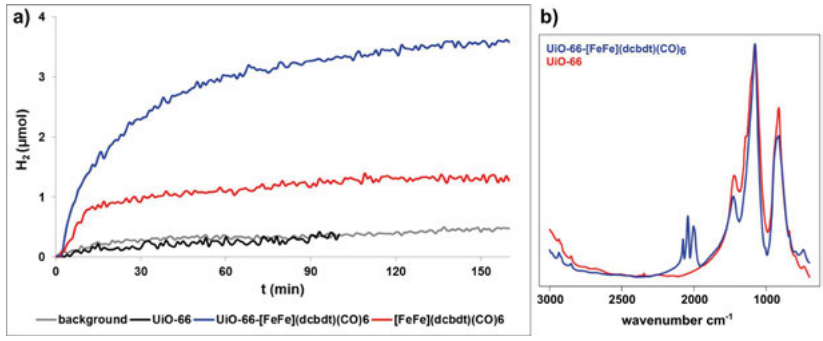

Figure 4.5. a) Hydrogen production with UiO-66-**1** and homogenous **1** in pH 5 acetate buffer (1 M) in presence of photosensitizer $Ru(bpy)_3Cl_2$ (0.5 mM) and sacrificial donor ascorbic acid (100 mM) under irradiation of blue light (475 nm). b) IR spectra recorded after the experiment. Adapted with permission from reference [170]. Copyright © 2013

This first project is a proof of concept. **1** could be introduced into UiO-66 and the resulting heterogenous catalyst showed to be more active and durable than the homogenous analog in solution. The superior performance of the new material is attributed to stabilization of catalytic intermediates by the framework and the presence of ν_{CO} bands in the IR spectrum recorded after photocatalysis supported this notion. Advantageous with UiO-66 as scaffold is the relatively easy preparation and straightforward introduction of the catalytic sites by PSE. UiO-66 is highly robust to chemical modifications and water stable, which are important features for proton reduction and further manipulation of the catalyst and its chemical environment. However, there are a few drawbacks coming along with UiO-66 as matrix: The pores of UiO-66 are relatively small (8 – 11 Å) and the windows are about 6 Å in size,[112] resulting in some limitations regarding accessibility of the incorporated catalyst. In addition, UiO-66 is an insulating material[171,172] and therefore does not facilitate electron transport between the catalyst sites. All these drawbacks lead to the question whether all immobilized catalysts are taking part in hydrogen production or if catalysis is limited to the surface of the UiO-66 particles. We therefore extended the scope of MOFs to MIL-101, in order to circumvent some of the limitations of UiO-66. At the same time a different strategy was used for catalyst immobilization that is called post-synthetic modification. This is described in the following section.

4.3 Post-Synthetic Modification in MIL-101-NH_2

4.3.1 Preparation of MIL-101-**2**

Post-synthetic functionalization and modification (PSM) of MOFs has been investigated extensively over the past years.[115] While simpler functional groups

can already be introduced during the solvothermal synthesis process, many more complex or thermally labile functionalities would not survive the harsh synthesis conditions. Therefore, Hupp, Cohen, and others have developed PSM as a powerful strategy. The most common starting materials are amino-functionalized linkers that can be introduced via solvothermal synthesis to many MOFs. Via amide-coupling, a variation of smaller molecules has successfully been introduced to those MOFs in reasonably good yields.[173] Post-synthetic metalation of open coordination sites such as bipyridine linkers[174] is another strategy of incorporating more complex units into MOFs. These are just two of many examples and more are discussed in review articles by Cohen.[115,117]

In Paper IV, complex **2** was introduced into the MIL-101(Cr) framework. MIL-101 is known for its high stability in water and even strongly acidic media.[111] In comparison to UiO-66, the pores (29 – 34 Å) and windows (12 – 14.5 Å) are much bigger. Thus, MIL-101 seemed to be a good candidate for immobilizing the proton reduction catalyst **2**. MIL-101 was prepared solvothermally and then functionalized with amino groups in two steps via nitration with concentrated HNO_3 and subsequent reduction with $SnCl_2 * 2\,H_2O$ at 70 °C according to literature procedures.[175,176]

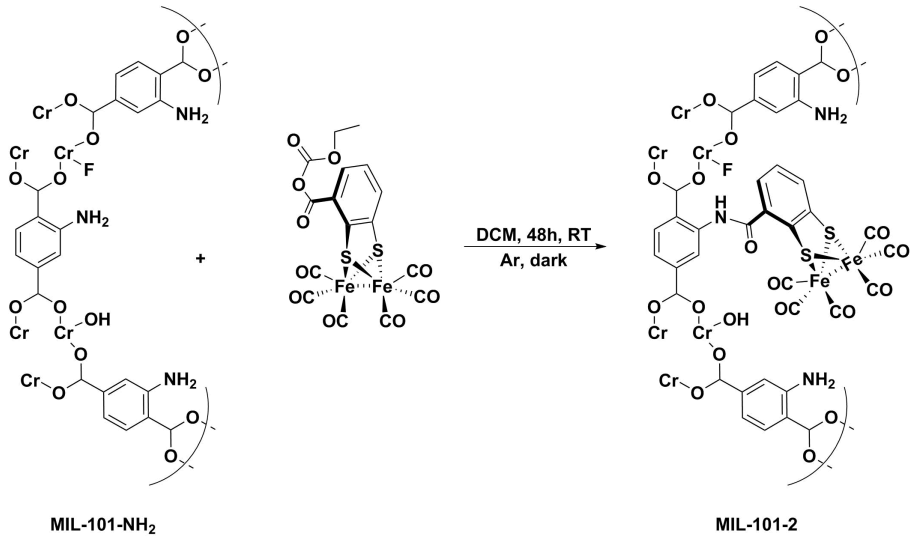

Scheme 4.1. Post-synthetic modification on MIL-101-NH_2 with **2**. Adapted from reference [177] by permission from The Royal Society of Chemistry.

Complex **2** was first transformed into the anhydride and then reacted for 48 h at RT with amino-functionalized MIL-101 (see Scheme 4.1). It should be noted, that the previously established procedure for functionalizing homogenous **2** using PyBop as coupling reagent did not work well in MIL-101. Elemental analysis of MIL-101-**2** suggested an incorporation yield of 5.28 wt.-%,

which corresponds to 24.3 % of all the linkers. Lowering the reaction time to 36 h and 16 h leads to yields of 2.35 wt.-% (9.4 %) and 0.59 wt.-% (2.2 %), respectively. The resulting materials were characterized by PXRD and SEM to prove unchanged crystallinity of the MOF. IR spectroscopy and EXAFS showed that the catalyst remains in its original form. A small shift in IR frequencies indicated successful formation of the amide bond and incorporation of catalyst **2**.

4.3.2 Photochemical Hydrogen Production with MIL-101-**2**

Photochemical hydrogen production was carried out under the same conditions as described for the UiO-66 system. All three materials with varying loadings were compared (Figure 4.6). Since the pores of MIL-101 are large enough for penetration of the photosensitizer $Ru(bpy)_3Cl_2$, it can be assumed that all immobilized catalysts are accessible to photo-reduced $[Ru(bpy)_3]^{2+}$ and thus will be participating in catalysis. TONs were calculated for the individual experiments (inset in Figure 4.6). Comparison of the three different materials showed that hydrogen production is proportional to catalyst loading. IR spectra of the solids after photocatalysis showed that most of the catalyst had decomposed. As catalysis is ultimately terminated by catalyst degradation, this observation is a proof that the majority of catalysts are involved in catalysis.

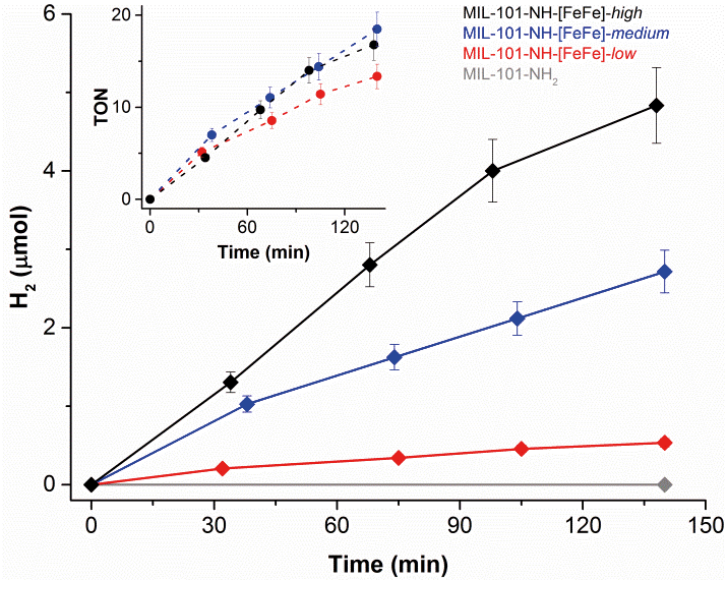

Figure 4.6. Photocatalysis with MIL-101-**2**. Conditions: MOF samples were suspended in a mixture of pH 5 acetate buffer (1 M), $Ru(bpy)_3Cl_2$ (0.5 mM) and ascorbic acid (100 mM). The mixture was irradiated with blue light (475 nm). Reproduced from reference [177] by permission from The Royal Society of Chemistry.

4.4 Summary and Conclusion

In this chapter, the preparation of two MOF-catalysts containing the two [FeFe]-H_2ase active site models **1** and **2** was presented. Structural integrity of both MOFs and incorporated catalysts was confirmed by a variety of methods. Both MOF-catalysts yielded higher amounts of hydrogen under photocatalysis conditions compared to the homogenous system. The superior performance was explained by stabilization of catalytic intermediates through the surrounding framework. In the case of MIL-101, all immobilized catalysts showed to be active in hydrogen production. For UiO-66, it is questionable how large the active portion really is. In chapter 7, a detailed study on catalyst accessibility in the two MOFs will be presented.

5. Combining Catalyst and Photosensitizer in One MOF

In this chapter, two new MOFs – UiO-67 and pcn-700 – will be introduced briefly, and their potential for functionalization with complex **1** will be evaluated. In addition, functionalization of UiO-67 with both **1** and a photosensitizer as well as the hydrogen formation activity of the resulting materials will be presented. All these are preliminary results that have not been published yet.

5.1 Introduction

Functionalization of UiO-66 and MIL-101 as discussed in the previous chapter led to stabilization of catalytic intermediates and thus increased hydrogen production activity of the MOF-catalysts. In both photocatalysis systems, $Ru(bpy)_3Cl_2$ was added to the solution as external photosensitizer. The aim of this chapter is to investigate the potential of MOFs for hosting both the catalyst and the photosensitizer. If both functionalities are immobilized next to each other in the framework, electron transfer between them should be more efficient than in the heterogenous/homogenous junctions described in chapter 4.

Two examples of dual functionalization with molecular catalysts and photosensitizers incorporated in one MOF have been described in the literature. The first example was presented by Hou and coworkers.[178] They used UiO-67 as platform to co-incorporate $Pt(dcbpy)Cl_2$ (dcbpy = 5,5'-bipyridyl dicarboxylate) as catalyst and $Ru(dcbpy)_3Cl_2$ as photosensitizer during the solvothermal synthesis of the framework. UiO-67 is the extended version of UiO-66 with larger 4,4'-dicarboxy biphenyl (= BPDC) linkers. Like in our Paper III, the authors were taking advantage of the matching sizes of the biphenyl and bipyridyl linkers for the preparation of the material. The resulting MOF was employed for photochemical hydrogen formation in acetate buffer at pH 5 with EDTA-2Na as sacrificial donor under visible light. Indeed, hydrogen production rates increased compared to all homogenous control experiments and this was attributed to the proximity of catalysts and photosensitizers. The authors, however, did not compare the bifunctional material to the corresponding MOF with only catalyst incorporated and photosensitizer in solution. A second example was shown by Feng and his group.[135] They used an analog of our complex

1 as catalyst. This complex is bridged by an adt-linker containing a terminal pyridyl group. The pyridyl was used as an anchor to coordinate the complex to the central Zn atom of porphyrine linkers the MOF was built up from. The catalyst was introduced post-synthetically by soaking the MOF in a solution of the complex for 2 d. Photocatalysis was tested under the same conditions as our system (pH 5 acetate buffer and ascorbate as sacrificial donor) and showed increased performance compared to the homogenous control.

The aim of the projects described in this chapter was to find suitable MOFs for incorporating complex **1** together with suitable photosensitizers.

5.2 Dual Incorporation in UiO-67

UiO-67 is an analog of the previously used UiO-66, containing BPDC linkers instead of BDC. With the larger linker size it offers the possibility of co-incorporating the photosensitizer $Ru(dcbpy)(bpy)_2Cl_2$ together with catalyst **1**. There are four possible strategies that have been used previously for incoporating molecular complexes:

- Functionalization directly during solvothermal synthesis has been the most common method.[120,121,178,179]
- Post-synthetic modification as described in Paper IV.
- Post-synthetic metalation, where open coordination sites on linkers in the framework are saturated by soaking the MOF in metal-salt solution.[129,159,174]
- Post-synthetic linker exchange as descibred in Paper III.

It is difficult to predict the best conditions for incorporating a new functionality into the MOF. As post-synthetic exchange showed to be a good way for incorporating **1** into UiO-66, the same method was used in this project. For the incorporation of the photosensitizer, two different strategies were tested, as described in the following sections.

5.2.1 Solvothermal Synthesis Approach

Solvothermal synthesis with $Ru(dcbpy)(bpy)_2Cl_2$ in the reaction mixture followed by post-synthetic linker exchange with the catalyst was explored first (Scheme 5.1). Solvothermal incorporation of $Ru(dcbpy)(bpy)_2Cl_2$ had been reported before[120] and therefore seemed to be a good starting point.

UiO-67-[Ru] was prepared according to the literature procedure:[120] A mixture of $Ru(dcbpy)(bpy)_2Cl_2$, BPDC, $ZrCl_4$ and acetic acid as modulator was suspended in 5 mL DMF in a screw cap vial. After sonication for a few minutes, the vial was placed into a preheated oven at 120 °C and heated for 24 h. After extensive washing and soaking in MeOH for 3 d, the samples were dried in

vacuum. Typically, this procedure yields incorporation of 3 wt.-% Ru, which corresponds to 1.5 % of all linkers.

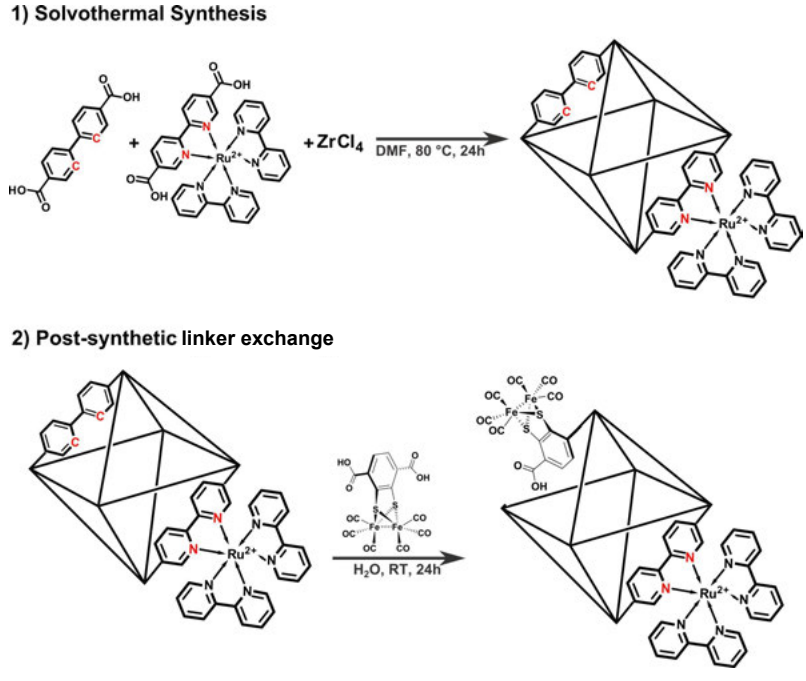

Scheme 5.1. Preparation of UiO-67-[Ru]-**1** via stepwise solvothermal synthesis and linker exchange.

In the second step, catalyst **1** was introduced by post-synthetic linker exchange. For this, UiO-67-[Ru] was placed into an aqueous solution of **1**. After sonication for 5 min, the suspension was placed onto a shaker for 24 h at RT. After extensive washing and soaking in MeOH for 3 d, the powder was dried in vacuum for further characterization. Successful incorporation of the complex could be shown by IR spectroscopy (Figure 5.1 a)). The content of catalyst was less than 2 % of all the linkers, as the ^{1}H-NMR spectrum of the digested material suggested. It should be noted that there is a size-mismatch between the linkers in UiO-67 and catalyst **1**. Only one of the two carboxylates coordinates to a Zr-cluster, leaving a defect site at the opposite cluster. This could be one reason for low catalyst incorporation. Another reason is the relatively poor crystallinity of solvothermally synthesized UiO-67-[Ru] compared to pure UiO-67, as indicated by SEM (Figure 5.1 b)).

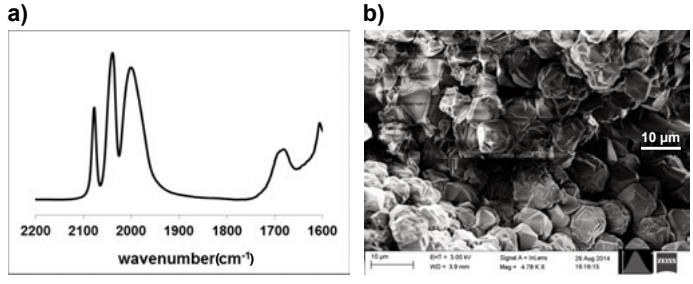

Figure 5.1. a) IR spectrum and b) SEM image of UiO-67-[Ru]-**1**.

Photocatalysis was tested under the same conditions as before. The new bifunctional material UiO-67-Ru-**1** did indeed show hydrogen formation when suspended in pH 5 acetate buffer with ascorbate as sacrificial donor. The overall yield was very low (0.3 μmol) (Figure 5.2). It should however be noted that the incorporation yield of the catalyst was significantly lower than in UiO-66 and that there was no excess of photosensitizer present. Crystallinity probably plays a crucial role in the PSE process as well as in catalysis. The poor crystallinity of UiO-67-[Ru] probably results in blocking of pores and channels and thus makes large fractions of the MOF inaccessible to substrates. Higher crystallinity should lead to increased exchange rates and thus a higher degree of incorporation of both photosensitizer and catalyst. Higher loading of the two functionalities would most likely increase overall hydrogen production.

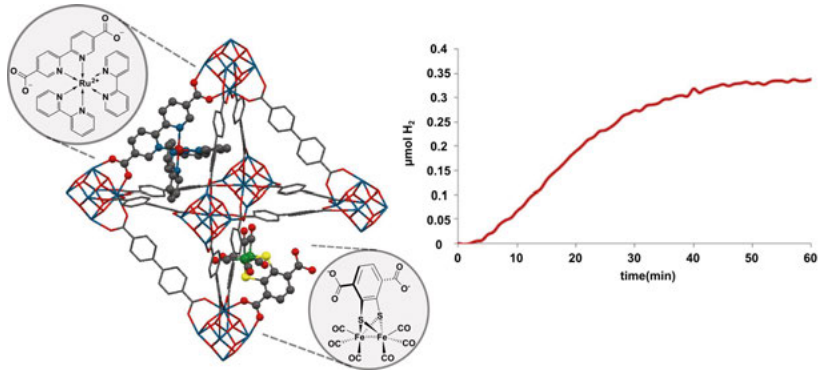

Figure 5.2. Photocatalysis with UiO-67(biphenyl)-[Ru]-**1** in pH 5 acetate buffer (1 M) in presence $Ru(bpy)_3Cl_2$ (0.5 mM) and ascorbic acid (100 mM) under irradiation of blue light (475 nm)

5.2.2 Post-Synthetic Metalation Approach

In order to increase incorporation yields, a different approach was used to functionalize UiO-67 with Ru by post-synthetic metalation. For this, UiO-67(bpy)

was prepared, which is an analog of UiO-67 containing unmetalated DC-bpy (DC-bpy = 2,2'-bipyridyl 5,5' dicarboxylate) linkers. The solvothermal synthesis of this material allows introduction of free bpy-ligands in a range of 36 – 73 % of all linkers as shown by Fei and Cohen before.[174] UiO-67(bpy) retains its high crystallinity and the open bpy sites can readily be metalated afterwards. In this project, UiO-67(bpy) was first metallated with $[Ru(bpy)_2]^{2+}$, followed by post-synthetic linker exchange with catalyst **1**.

First, UiO-67 containing 25 % bpy linkers was prepared solvothermally according to the literature procedure.[174] Subsequent metalation with $[Ru(bpy)_2]^{2+}$ yielded 72 % filling of all bpy-sites as shown by ICP-OES analysis. This corresponds to 18 % of all linkers in the MOF.

After PSE with complex **1**, an average Ru-content of 17 % and for **1** of 4.2 % in relation to linkers was obtained as ICP-OES revealed. IR spectra showed that complex **1** was intact after PSE (Figure 5.3 a)).

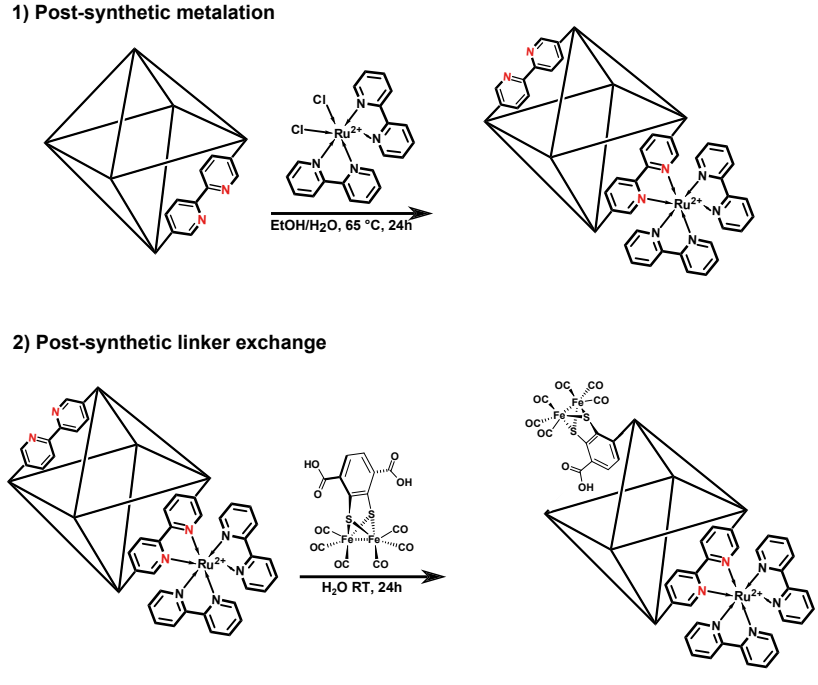

Scheme 5.2. Preparation of UiO-67(bpy)-[Ru]-**1** via stepwise post-synthetic metalation and linker exchange.

Crystallinity of both UiO-67(bpy)-[Ru] and UiO-67(bpy)-[Ru]-**1** is comparable to pristine UiO-67 as PXRD shows (Figure 5.3 b)). In comparison to the previously described materials, the overall Ru-content could be increased with this procedure. Incorporation of **1**, on the other hand, improved only slightly. Due to the size-mismatch of the linkers, incorporation of **1** is not as much

favored as it is in UiO-66, where both carboxylate groups are connected to Zr-clusters.

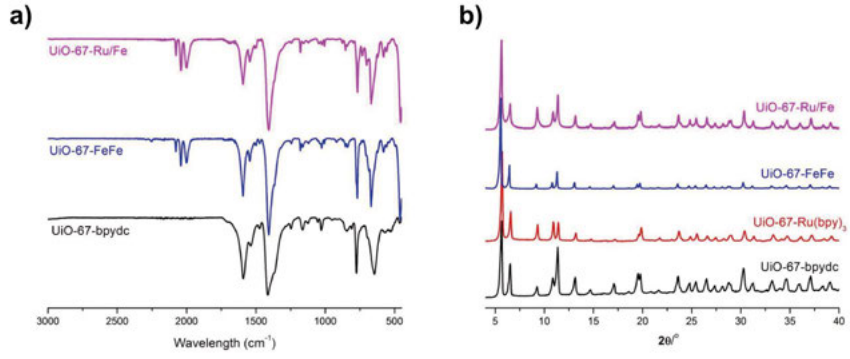

Figure 5.3. a) IR spectra and b) PXRD of UiO-67(bpy), functionalized with $Ru(bpy)_2Cl_2$ and **1**.

Photochemical hydrogen production experiments yielded surprising results: No hydrogen could be observed at all. Even when UiO-67(bpy) was only functionalized with **1** and $Ru(bpy)_3Cl_2$ was added to the solution, no hydrogen was produced (Figure 5.4).

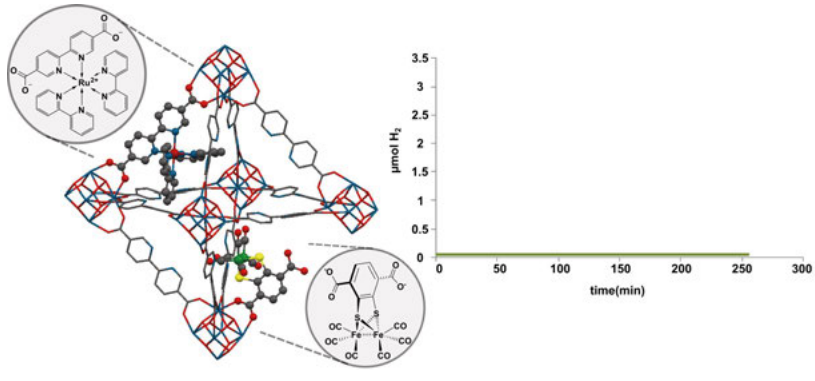

Figure 5.4. Photocatalysis with UiO-67(bpy)-[Ru]-**1** in pH 5 acetate buffer (1 M) in presence $Ru(bpy)_3Cl_2$ (0.5 mM) and ascorbic acid (100 mM) under irradiation of blue light (475 nm).

The hypothesis is that open bpy-sites in the material cause the problem. In pH 5 acetate buffer, they can be protonated upon reduction and this way act as trap states for electrons. In order to proof this hypothesis, electrochemical analysis of the free bpy ligand was carried out. Due to its low solubility in H_2O, the experiment was carried out in MeCN and the carboxylates were protected with methyl groups. The CV of dm-bpy (dm-bpy = dimethyl-[2,2'-bipyridyl] 5,5' dicarboxylate) in MeCN with 0.1 M $TBAPF_6$ as supporting electrolyte shows two electrochemically reversible reductions at $E_{a,1/2} = -2.03$ V

and $E_{b,1/2} = -1.75$ V (Figure 5.5). If acetic acid is added to the solution, the wave transforms into one redox event with less negative reduction potentials ($E_{p,c} = -1.60$ V and $E_{p,a} = -1.29$ V). This potential is within reach of photoreduced $[Ru(bpy)_3]^+$. Thus, the reducing equivalents that are photo-generated within the MOF remain on the protonated bpy ligands since there is only a very small driving force for electron transfer to the catalyst.

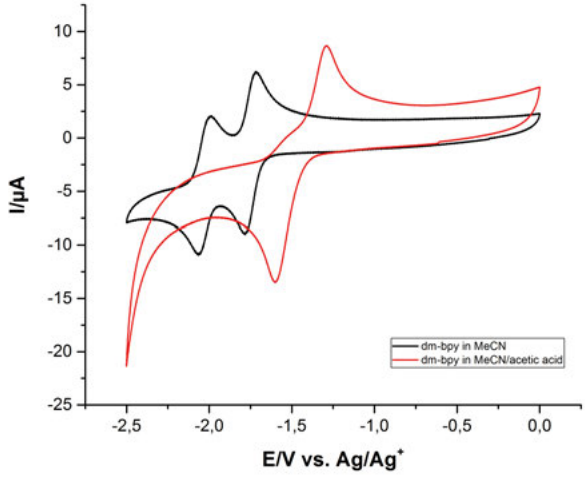

Figure 5.5. Cyclic voltammogram of dm-bpy in MeCN (black) and in presence of acetic acid (35 mM) (red). The spectra were recorded at a scan rate of 100 mV s^{-1} and 0.1 M $TBAPF_6$ was present as supporting electrolyte.

5.2.3 Proposed Structures of Catalysts with Matching Linker Size

The low incorporation yield of complexes **1** into UiO-67 is most likely due to the size mismatch between BPDC and dcbdt. Therefore, the synthesis of alternative catalyst-linkers with a biphenyl backbone would be desirable (Scheme 5.3). The two proposed structures have not been synthesized yet. A brief description of a synthesis plan is given as an outlook. The first alternative considered would be Fe_2(dcbpdt)$(CO)_6$ (dcbpdt = 4,4'-dicarboxyl biphenyl 2,2'-dithiolate, **15**). A similar Fe_2 complex, lacking the two carboxylates, has been prepared and characterized in our group before.[180] In this complex, the two phenyl rings are twisted due to the position of the thiolates. Such a twisted linker would not be optimal for incorporation into UiO-67, since it might disturb the connectivity of the linker with two Zr-clusters. In the next section, twisted linkers were used to build up a new zirconium based MOF with a different structure than UiO-67.

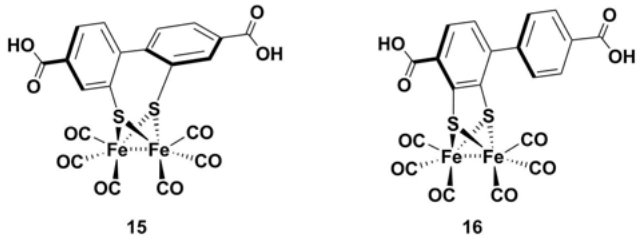

Scheme 5.3. Alternative complexes based on biphenyl-linker.

A better ligand would probably be the unsymmetric complex **16**, where the dithiolate is located on one of the phenyl rings. The synthesis of this complex could proceed via cross-coupling of 4-bromo-benzoic acid and 4-bromo-2,3-dihydroxybenzoic acid, followed by Newman-Kvart rearrangement to form the dithiolate.

5.3 Post-Synthetic Linker Insertion in pcn-700

A very recent development is the synthesis of MOFs with unsaturated coordination bonds on the metal-cluster. First examples were presented by Hupp and coworkers, who designed a MOF with 8-coordinated Zr-clusters that they called NU-1000 (NU = northwestern university).[166,181] The open coordination sites are initially occupied by terminal OH^- ligands that can post-synthetically be replaced by organic linkers. This strategy allows the formation of MOFs with mixed linkers and directed insertion of functional units (e.g. ferrocene) to make the framework redox active.[182] Another example is pcn-700 (pcn = porous coordination network), prepared by Zhou and coworkers and used for sequential linker installation.[183] It is prepared from 2,2'-dimethylbiphenyl-4,4'-dicarboxylic acid and $ZrCl_4$. Due to the methyl substitution in the 2,2' positions, the dihedral angle of the two phenyl rings changes, leading to a different coordination pattern compared to conventional UiO-67. Also here, 8-coordinated Zr-clusters are obtained and the framework structure features two different emtpy pockets to be filled sequentially by other ligands. The smaller pocket is about 7 Å in size, which corresponds roughly to the length of a BDC linker. The larger one is 16.5 Å long; that is equivalent to the length of terphenyl dicarboxylic acid. Encouraged by this study a collaboration partner of ours, Dr. Le Wang, suggested to use pcn-700 as a platform for incorporating catalyst **1** together with a larger dye molecule in order to obtain a bifunctional system. In this thesis, an initial study on introduction of **1** into pcn-700 is presented.

Crystals of pcn-700 were prepared by Dr. Le Wang. In constrast to UiO-66 and MIL-101, these samples are much larger in crystal size (about 50 μm, Figure 5.6). Insertion of complex **1** was tested both in H_2O and MeOH. The crystals were carefully suspended in concentrated solutions of complex **1** and left

under argon at RT. After 24 – 48 h the liquid phase was removed with a pipette and the crystals were washed with MeOH until the liquid layer remained clear. Since the crystals are so large, they can be examined under an optical microscope. A color change from white to orange after insertion of the complex indicated successful incorporation of **1** (Figure 5.6). IR spectroscopy revealed that the best incorporation yield was achieved with 48 h in MeOH (Figure 5.7). IR frequencies are identical in number and shift to the homogenous complex, indicating that the catalyst keeps its original structure. Single crystal X-ray analysis was used in order to confirm placement of the catalyst inside the smaller pockets. Results were however inconclusive. Further experiments will be required in order to proof correct placement of the catalyst inside the framework and to show the overall yield of insertion.

Initial photocatalysis experiments with functionalized pcn-700 yielded detectable amounts of hydrogen (Figure 5.7 b)). Since the catalyst loading was unknown, these results are not quantitative. However, they show that pcn-700-**1** is a potent catalyst and the insertion of a suitable photosensitizer will probably allow the preparation of a bifunctional MOF-photocatalyst.

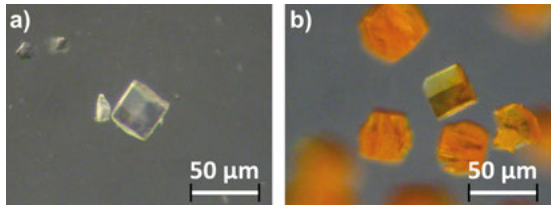

Figure 5.6. Optical images of a) pcn-700 and b) pcn-700-**1**.

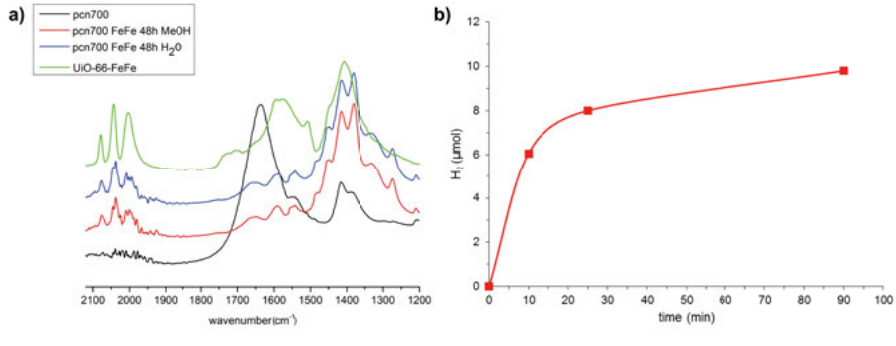

Figure 5.7. a) IR spectra of pcn-700 blank (black), pcn-700-**1** prepared in MeOH (red) and H_2O (blue) and the homogenous complex **1** (green). b) Photocatalysis in 1 M acetate buffer at pH 5 with $Ru(bpy)_3Cl_2$ (0.5 mM) and ascorbic acid (100 mM) under irradiation of blue light (475 nm)

5.4 Summary and Conclusion

In summary, two new MOFs have been investigated for their potential to incorporate complex **1**. UiO-67 is the biphenyl-analog of UiO-66 and the co-incorporation of **1** and Ru(dcbpy)$(bpy)_2Cl_2$ was successful. However, incorporation yields for both were very low when the hybrid material was prepared by a combination of solvothermal and PSE functionalization. Hydrogen formation with this material was observed, but did not substantially improve compared to the heterogenous/homogenous UiO-66 system. The alternative route, via post-synthetic metalation of open bpy-sites in UiO-67 with Ru and subsequent PSE with **1** yielded higher incorporation of the photosensitizer. However, due to the presence of open bpy-sites that act as trap states during photocatalysis, the material did not perform as catalyst at all. A possible strategy would be to execute repeated cycles of metalation on UiO-67(bpy) until all open bpy-sites are filled up.

Main reason for the low incorporation of **1** into UiO-67 is the difference in linker size. The synthesis of new catalysts with biphenyl backbones would be necessary in order to improve incorporation into UiO-67.

In the second part, the incorporation of **1** into pcn-700 was tested. Initial experiments showed successful incorporation of the complex and therefore high potential for this material to serve as a platform for bifunctional catalysis. In order to advance the project, a terphenyl-dicarboxylate-based photosensitizer with matching redox potential would need to be designed and co-incorporated into pcn-700 together with the catalyst.

6. Probing Accessibility of **1** and **2** in UiO-66 and MIL-101

In this chapter, chemical reduction of MIL-101-**2** and UiO-66-**1** with cobaltocene will be used in order to explore catalyst accessibility in the two frameworks (Paper IV). In addition, spectro-electrochemistry is used to investigate UiO-66-**1**.

6.1 Introduction

In previous chapters the performance of MOF incorporated catalysts **1** and **2** in photocatalysis schemes has been described. Overall, higher yields of hydrogen production were obtained compared to the homogenous system. This finding suggests higher stability of catalytic intermediates which is achieved by the surrounding framework. However, it remained unclear whether all catalyst units in the MOF crystals were participating in catalysis, or if the functionality was restriced to the outer layers. For UiO-66 it is reasonable to believe that not all catalysts can be active, because the pore windows (approx. 6 Å) are not large enough to let $Ru(bpy)_3Cl_2$ molecules penetrate into the framework. At the same time, electron transport through the framework is probably very slow since the large $Zr_6(OH)_4O_4$-clusters are insulating.[171] In the case of MIL-101, pore windows are presumably large enough (12 – 14.5 Å) for the dye molecules to come in. In this chapter, the chemical reductant cobaltocene will be used to study catalyst accessibility inside both MOFs.

6.2 Chemical Reduction of MIL-101-**2** and UiO-66-**1** with Cobaltocene

Chemical reduction of the two different MOF-catalysts was conducted using cobaltocene. The reduction potential of cobaltocene (-1.33 V vs. Fc/Fc^+) suggests a driving force of 150 m V for the reduction of both catalysts **1** and **2**. Figure 6.1 shows the resulting IR spectra. In MIL-101-**2**, a large fraction of the catalyst could be reduced as indicated by the formation of three new absorption bands in the IR spectrum at 1882, 1928, and 1978 cm^{-1}, as well as a synchronous decrease of the three initial ν_{CO} bands. This is consistent with the formation of the doubly-reduced state observed in spectro-electrochemical experiments (Paper I) with reference complex **3**.

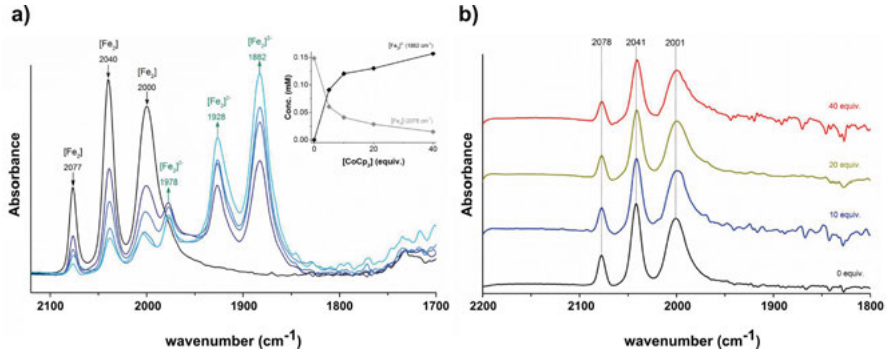

Figure 6.1. Chemical reduction of a) MIL-101-**2** and b) UiO-66-**1** with cobaltocence in MeCN. Reproduced from reference [177] by permission from The Royal Society of Chemistry.

Addition of up to 40 eq. cobaltocene led to reduction of 82 – 90 % of all incorporated catalysts, depending on the catalyst loading. This number is well in accordance with the previously observed degradation of the catalyst under photochemical hydrogen evolution as described in chapter 4: After the experiments, intensity of IR bands was 80 – 85 % lower compared to the starting material, suggesting that this fraction had taken part in catalysis.

For UiO-66-**1**, no change in the IR spectrum was observed, even after addition of 40 eq. cobaltocene (Figure 6.1 b)). Since cobaltocene is very similar in size as the pore windows of UiO-66 (about 6.6 Å corrected for van der Waals radii)[177] penetration of cobaltocene into UiO-66 might simply be disfavored. The other hypothesis is that oxidized cobaltocene and reduced catalyst at the surface of the particles form stable ion pairs that are blocking the entrance for further cobaltocene molecules. Thus, the interior of the particles remains unreduced. Either way, it is now clear that large amounts of catalyst incorporated in UiO-66 do not participate in catalysis. Since $Ru(bpy)_3Cl_2$ is too large to enter the pores of UiO-66, only the catalysts on the particle surface will be reduced during photocatalysis. Electron transfer between the different catalysts immobilized in the framework is not occuring as shown by these chemical reduction experiments.

6.3 Spectro-electrochemical Reduction of UiO-66-**1**

In order to circumvent insufficient chemical reduction by cobaltocene and to test whether the size exclusion argument holds, a spectro-electrochemical experiment was carried out.

A suspension of UiO-66-**1** (1 mg) in 1 mL of a stock solution of cobaltocenium hexafluorophosphate (2 mM) and $TBAPF_6$ (0.1 M) in dry MeCN was prepared in the glove box and left to soak for 10 min. This way, cobaltocenium should be distributed all inside UiO-66 (if it can enter the pores) and

thus be close to all immobilized catalyst units. 100 μL of the suspension was drop-casted onto a Pt-mesh, which is functioning as working electrode in the liquid-IR spectroelectrochemical cell (IR-SEC cell).

Figure 6.2 shows a schematic of the IR-SEC-cell as well as SEM images of drop-casted UiO-66-**1** onto Pt-mesh. Some of the particles are directly attached to the Pt electrode, while other particles are in close proximity between the mesh. After the solvent had evaporated, the cell was assembled and filled with electrolyte/cobaltocenium stock solution. In addition to the Pt-working electrode, the cell was equipped with a Pt counter electrode and a Pt wire as quasi-reference electrode. The cell was connected to a potentiostat and placed into an IR spectrometer. A potential of -1.5 V was applied, which should be sufficiently negative to reduce all cobaltocenium rapidly. At the same time, IR spectra were recorded to follow up on the reduction of the catalyst. Figure 6.3 shows the IR spectrum of UiO-66-**1** together with the difference spectrum after applying -1.5 V over 10 min.

A large fraction of the catalyst is reduced (approx. 50 %), which is indicated by the bleach of the three bands at 2073, 2038, and 1997 cm^{-1}. Two new IR absorption bands occurred at 1918 and 1882 cm^{-1}. The shift of about 120 cm^{-1} indicates the formation of the doubly-reduced species UiO-66-**1**$^{2-}$ and is similar to the reduction product of chemically reduced MIL-101-**2**$^{2-}$. Table 6.1 summarizes the data for reduced UiO-66-**1**, MIL-101-**2** and homogenous **3**.

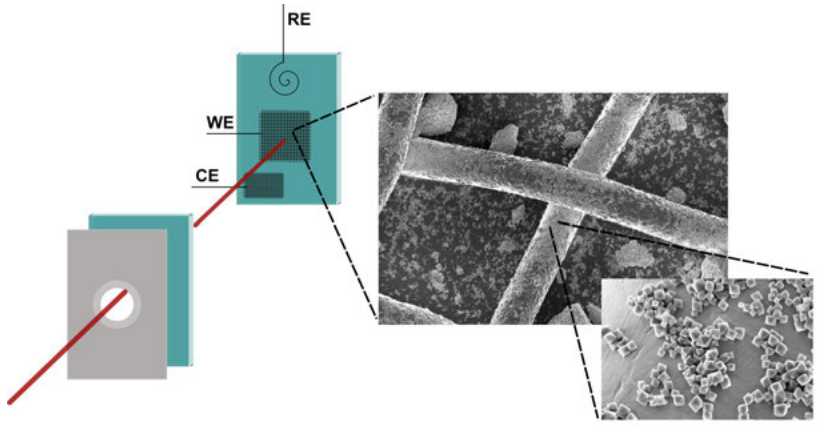

Figure 6.2. Setup of the liquid-IR spectro-electrochemical cell (IR-SEC cell). The inset shows the SEM image of dropcasted UiO-66-**1** on a Pt-mesh similar to the working electrode of the cell.

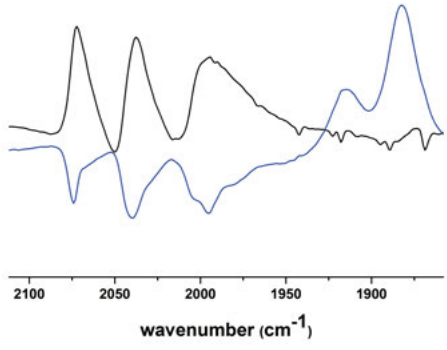

Figure 6.3. IR spectrum (in MeCN) obtained from spectro-electrochemical reduction of UiO-66-**1** soaked in cobaltocenium and electrolyte.

Table 6.1. *IR frequencies of the reduced states of UiO-66-**1**, MIL-101-**2**, and the molecular reference **3**.*

Species	**IR frequencies** (cm^{-1})	**Method**
UiO-66-**1**	2073, 2038, 1997	
UiO-66-$\mathbf{1}^{2-}$	1918, 1882	spectro-electrochemistry
MIL-101-**2**	2077, 2040, 2000	
MIL-101-$\mathbf{2}^{2-}$	1978, 1928, 1882	chemical reduction
3	2080, 2044, 2004	
$\mathbf{3}^{1-}$	2035, 1980, 1890	IR transient absorption laser spectroscopy
$\mathbf{3}^{2-}$	1964, 1914, 1865, 1682	spectro-electrochemistry

6.4 Summary and Conclusion

In this chapter, accessibility of the MOF-catalysts to chemical reductant cobaltocene was explored. MIL-101-**2** is readily reduced when an excess of the reductant is added and the yield can be quantified by IR spectroscopy. Interestingly, the amount of reduced catalyst in MIL-101 (82 – 90 %) is equivalent to the amount of degraded catalyst in the photochemical hydrogen evolution experiments described in chapter 3. These findings are consistent with the hypothesis that the majority of MIL-101 incorporated **2** is active in catalysis. The resulting product is the doubly-reduced form MIL-101-$\mathbf{2}^{2-}$ that is similar to doubly-reduced reference $\mathbf{3}^{2-}$. In contrast, the majority of catalyst in UiO-66-**1** is not available for reduction when cobaltocene is directly added to the MOF suspension. However, soaking UiO-66-**1** prior to electrochemical reduction in cobaltocenium solution allowed for circumventing the limitations

in the redox titration. A doubly-reduced species (UiO-66-**1**$^{2-}$) was observed in the IR-spectro-electrochemical experiment. This observation indicates that not the size of cobaltocene prevented reduction of catalysts in the interior of UiO-66-**1**; the reason might instead lie in the formation of stable ion pairs between reduced catalysts on the particle surface and oxidized cobaltocene. For photochemical hydrogen evolution, it can be concluded that in UiO-66-**1**, only the catalysts at the crystal surface are active since the dye molecules are too large to enter the MOF pores and electron transfer between the catalyst units is not facilitated.

7. Preparation and Study of UiO-66-**1** Thin Films on Conducting Glass Electrodes

In this chapter, the preparation and functionalization of UiO-66 thin films on conducting FTO glass electrodes is described. The films are functionalized with **1** via PSE and characterized structurally as well as electrochemically (Paper V).

7.1 Introduction

MOFs are often introduced with the notion that they potentially serve a lot of applications such as drug delivery,[101,102] chemical sensing,[104] gas storage,[105,184] catalysis,[106–108] and others. Also in artificial photosynthesis, MOFs have gained more and more interest.[165,185,186] The potential use of MOFs in artificial photosynthesis requires not only their functionalization with catalysts and photosensitizers, but also the development of integrated systems. It is therefore important to develop MOF-functionalized electrodes that can be implemented as a part of a solar fuel generating device as described in chapter 1 of this thesis. Preparation of pristine MOF thin films has been explored before and there are different methods to be used: Direct solvothermal synthesis, layer-by-layer preparation, electrochemical methods, and also the immobilization of preformed MOFs onto surfaces.[187,188] Until Paper VI was published, there had only been few studies on the preparation of functionalized MOF thin films.[189,190] Thereafter several studies followed, all aiming for catalysis applications of the resulting functionalized MOF thin films.[126,191,192]

7.2 Synthesis of UiO-66 Thin Films on FTO and Functionalization with **1**

In the presented study (Paper VI), UiO-66 thin films were grown solvothermally on FTO conducting glass substrates. For the successful preparation, a self-assembled monolayer (SAM) of BDC was pre-assembled by soaking the clean FTO glass substrate in a 1 mM solution of BDC in DMF. The exact concentration of the solution showed to be crucial for optimal film growth: higher

concentrations led to the formation of films very weakly attached to the surface, and without pre-treatment no films were obtained at all. SAM-FTO substrates were then added to vials containing the reaction mixture for solvothermal UiO-66 preparation and heated in an oven for 24 h at 120 °C. Varying the concentration of BDC in relation to $ZrCl_4$ and the modulator benzoic acid allowed controllable thickness of the films. Cross-section SEM images revealed that thick films of 20 μm and thinner films of 2 – 5 μm were obtained (Figure 7.1). The resulting films are homogenous and free of cracks, and they adhese strongly to the FTO substrate. The particle size was comparably large for the thicker films (2 μm) and similar to powder UiO-66 for the thinner ones (0.5 – 1 μm). Also PXRD confirmed that the crystallinity of the films is comparable to powder UiO-66 (Figure 7.2a)).

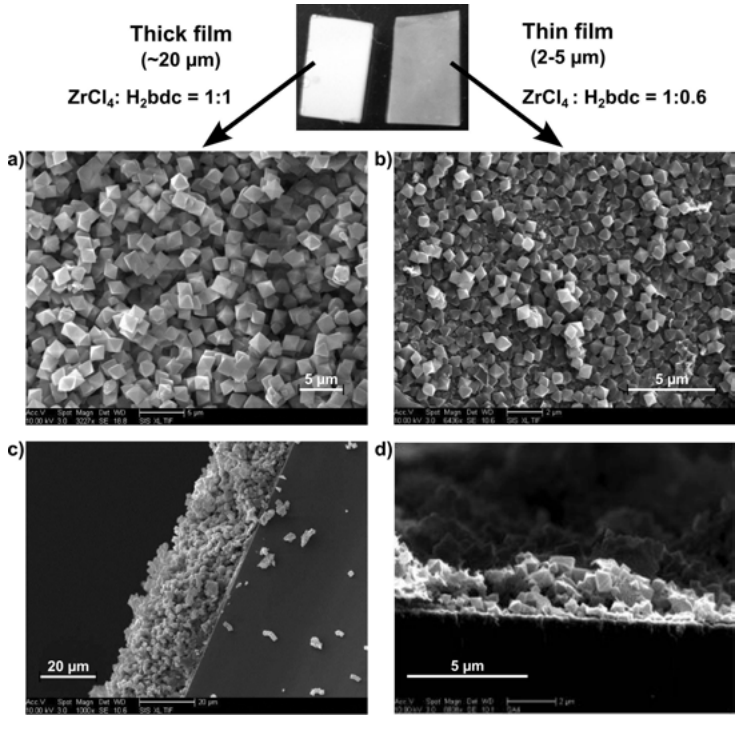

Figure 7.1. Preparation of UiO-66 thin films with different thickness. Reproduced from reference [193] by permission from The Royal Society of Chemistry.

Functionalization with **1** was achieved with small deviations to the conventional PSE method. The UiO-66-FTO substrates were placed in a vial with 20 mM aqueous solution of **1** for 72 h without stirring. After extensive washing and soaking in MeOH, the films were carefully dried under vacuum. After the treatment, the color of the films had changed clearly from white to orange, which is an indication for successful incorporation. The crystallinity of both films remained stable and prominent ν_{CO} stretching frequencies of **1** were ob-

served in the IR spectra (Figure 7.2). Interestingly, ^{1}H-NMR and EDX analysis suggested 32 – 35 % incorporation of complex **1** inside films of both thicknesses. This is substantially higher than for the powder UiO-66-**1**, where only up to 14 % of all linkers were replaced after PSE. The reason for increased incorporation yield might be the controlled arrangement of MOF particles within the films on the FTO glass substrate. In contrast, bulk powder MOF crystals often stack together. A control experiment with **3**, which is lacking the COOH groups, in the PSE solution yielded no IR bands in the CO region or color change after washing. This simple test shows that the complex **1** is not just simply trapped in the pores.

In addition to the described functionalization with **1**, PSE could also be demonstrated with a catechol ligand, which in an additional step could even be metalated with $FeCl_3$. The method is thus applicable to incorporation of other functionalities.

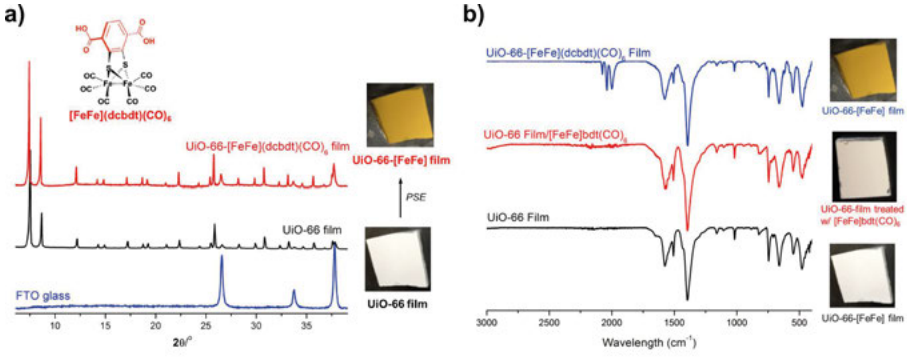

Figure 7.2. a) PXRD of the different UiO-66 thin films and b) corresponding IR spectra. Reproduced from reference [193] by permission from The Royal Society of Chemistry.

7.3 Electrochemical Analysis of UiO-66-**1** Thin Films

Electrochemical analysis of both films was conducted in DMF with 0.1 M $TBAPF_6$ as supporting electrolyte. Unfunctionalized UiO-66 films did not show any reduction event in a range between −2.5 – 0.5 V. Reference complex **1** shows a chemically reversible reduction $E_{p,c} = -1.35$ V and reoxidation $E_{p,a} = -1.10$ V. A formal half wave potential of $E_{1/2} = -1.18$ V is assigned to this redox event. However, as indicated by a large peak separation, the redox process is not electrochemically reversible. Electrochemical response of the UiO-66-**1**-films showed to be dependent on the film thickness. For the thicker films, electrochemical analysis did not show any detectable features. However, the whole CV was tilted. In the CV of the thinner films, two clear features could be observed: A reduction wave at $E_{p,c} = -1.45$ V and an oxidation event at $E_{p,a} = -0.8$ V, giving rise to a formal $E_{1/2} = -1.13$ V that is

very similar to **1** in solution. Both peaks were quite broad. The large peak separation and peak broadening can be explained by the insulating property of UiO-66 resulting in slow electron transfer kinetics.[171,172] Control experiments with FTO substrate soaked in a solution of **1** and treated in the same way as thin films after PSE did not give any response in the CV. This is a clear proof that the electrochemical response observed for the thinner films comes from UiO-66-**1**. Most likely, only the catalysts both close to the particle surface and close to the electrode are reduced. Therefore, the peak currents are relatively small compared to homogenous **1** in solution. The fact that no electrochemical response was observed for the thicker films, speaks for a gradient of PSE in UiO-66 films on FTO resulting in very low amounts of catalyst present close to the electrode surface in the 20 μm thick films.

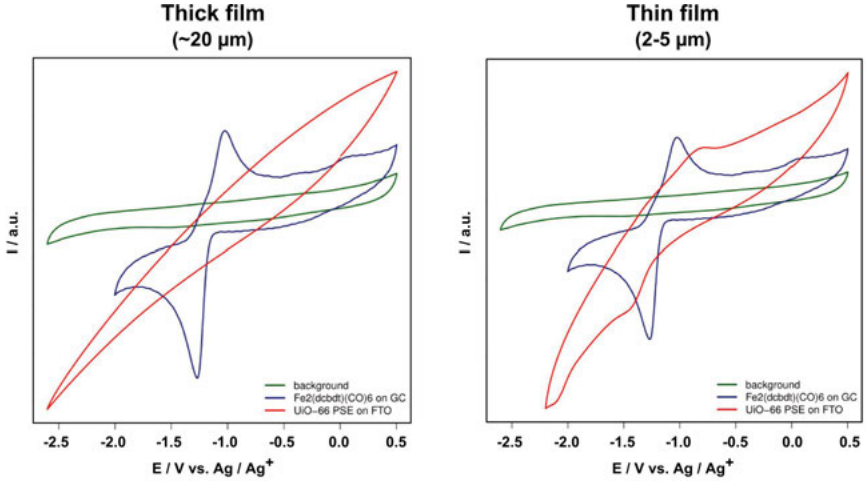

Figure 7.3. Cyclic voltammograms UiO-66-**1** (red) and blank UiO-66 (green) thin films as well as homogenous **1** (blue) in DMF with 0.1 M $TBAPF_6$ as electrolyte. CVs were recorded at a scan rate of 100 mV s^{-1}. Reproduced from reference [193] by permission from The Royal Society of Chemistry.

7.4 Summary and Conclusion

In summary, a facile method has been developed to prepare functional UiO-66-**1** thin films. By varying the BDC concentration during solvothermal preparation of the films, their thickness could be tuned. The electrochemical response of the UiO-66-**1** films showed to be highly dependent on the film thickness, because UiO-66 itself is insulating and thus prevents efficient electron transfer between incorporated catalysts. A future path following up on this project would be the preparation of very thin films that are built up from only a single layer of MOF particles. A first step towards such a design has already been

achieved in our group.[194] For this, UiO-66 films consisting of particle monolayers were solvothermally grown on Si-wafers. The crucial point was to turn the wafers upside-down inside the synthesis vials and thus prevent stacking of settling particles that were formed in solution. An initial aim of Paper VI was also the electrochemical characterization of UiO-66-**1** by immobilizing the material on an electrode. A simpler and faster alternative to growing and functionalizing films on the electrode is the preparation of MOF coatings e.g. by dropcasting a suspension of the particles. Our group has developed a set of techniques for this approach and could receive qualitatively good CVs. The interested reader is referred to the article [151], which is not discussed further in this thesis.

8. [FeFe]-H_2ase Active Site Model Chemistry in a UiO-66 Metal-Organic Framework

In this chapter, the reactiviy of **1** in UiO-66 towards phosphines is investigated and compared to homogenous reference complex **3** (Paper VI).

8.1 Introduction

In chapters 4 to 6, catalytic performance and catalyst accessibility of UiO-66-**1** and MIL-101-**2** were the main focus. Now, the interest lies in the study of chemical reactivity of UiO-66 incorporated [FeFe]-H_2ase active site mimic **1** compared to its homogenous analog **3**. MOFs are seen as an ideal platform for incorporation of organometallic complexes that are mimicking enzyme active sites, because their hybrid nature offers the possibility of chemical fine-tuning of both inner and outer coordination sphere.[36,165] In this context, the inner coordination sphere is referred to as the set of ligands directly coordinated to the active metal center. The outer sphere represents the surrounding pocket. Both can in principle be designed and constructed in MOFs to mimic specific functions of enzymes.

Research on [FeFe]-H_2ase active site model chemistry on the other hand, has not only focused on the catalytic performance of the model complexes; also structure-function relationships and mechanistic aspects of these organometallic complexes have been of interest.[195,196]

In Paper VI, the reactivity of complex **1** in UiO-66 towards a series of phosphine ligands was investigated and compared to homogenous reference **3**. The results are presented in this chapter.

8.2 Reactivity of UiO-66-**1** Towards Phosphines

Figure 8.1 presents the series of three phosphines with increasing size, namely PMe_3, PEt_3, and PPh_3. While the two former should fit into the pores of UiO-66, the latter one is too large. The reaction of homogenous complex **3** with phosphines has been explored on the example of PMe_3 before.[72] There are two synthetic strategies, leading to the same reaction products: The first one is to reflux a solution of **3** and PMe_3 in hexane for 4 h. This reaction yields a dinuclear, disubstituted product $Fe_2(bdt)(CO)_4(PMe_3)_2$ (**17**) together with a

mononuclear species $Fe(bdt)(CO)_2(PMe_3)_2$ (**18**) in a ratio of 2:1.[72] The same result can be achieved using Me_3NO as decarbonylation reagent and working in MeCN at room temperature.[66]

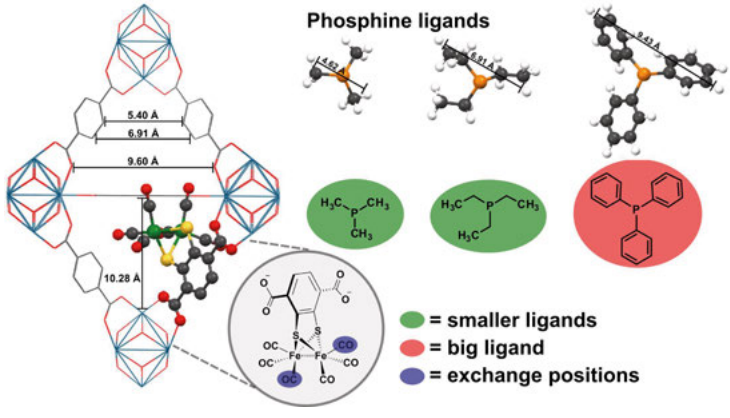

Figure 8.1. CO → phosphine ligand exchange on **1** in UiO-66. Reproduced from manuscript submitted to *Chemical Communications* (Paper VI) by permission from The Royal Society of Chemistry.

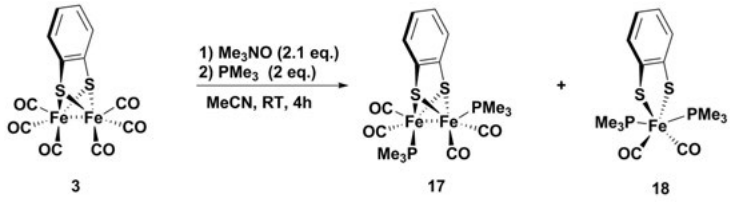

Figure 8.2. CO → phosphine ligand exchange in homogenous phase on the example of **3**. Reproduced from manuscript submitted to *Chemical Communications* (Paper VI) by permission from The Royal Society of Chemistry.

In the presented project, the second strategy was used and an example of the reaction with PMe_3 in solution is given in Figure 8.2. The reactivity of UiO-66-**1** towards the different phosphines was tested under the same conditions: 5 mg of UiO-66-**1** and 1 mg Me_3NO were suspended under argon in 5 mL dry MeCN and stirred for 10 min. Then 1 mL of a 1.0 M solution of the respective phosphine ligand in THF was added. After stirring for 1 – 5 d, the solid MOFs were separated and extensively washed with MeCN. Progress of the reaction was followed by IR specstroscopy. Figure 8.3 shows the resulting spectra for the reaction of UiO-66-**1** with PMe_3 and PEt_3 compared to homogenous reference complexes. The best results were achieved after 24 h for PMe_3 and about 80 % of the starting material was converted. The crystallinity of UiO-66 remains unchanged as shown by PXRD and SEM (Figures 8.4 and 8.5).

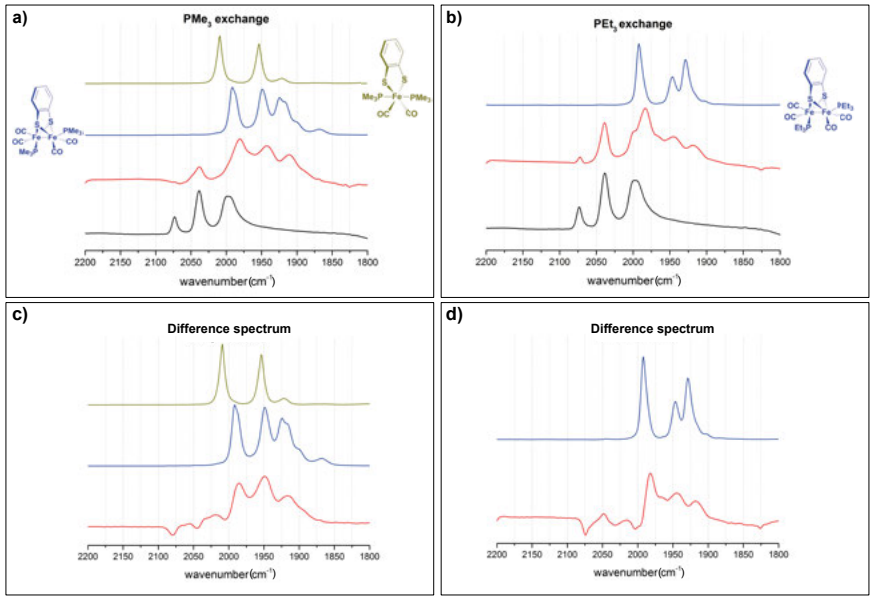

Figure 8.3. IR spectra of UiO-66-**1** (black) and reaction products (red) after treatment with a) PMe_3 and b) PEt_3. In blue are the disubstituted Fe_2 reference complexes (**17**) and in gold the mononuclear reference complex (**18**). c) and d) show the respective difference spectra (red) from substraction of the spectrum of the reaction product minus the spectrum of UiO-66-**1**. Reproduced from manuscript submitted to *Chemical Communications* (Paper VI) by permission from The Royal Society of Chemistry.

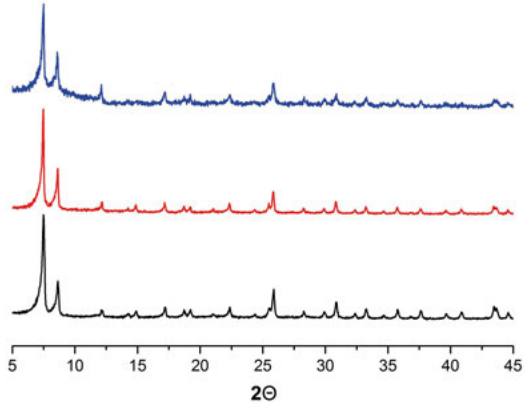

Figure 8.4. PXRD pattern of UiO-66 (black), UiO-66-**1** (red), and after reaction with PMe_3 (blue). Reproduced from manuscript submitted to *Chemical Communications* (Paper VI) by permission from The Royal Society of Chemistry.

Interestingly, in UiO-66 the only reaction product is the doubly-substituted, dinculear complex of the formula $Fe_2(dcbdt)(CO)_4(PMe_3)_2$ (**17b**) with IR frequencies of 1980, 1942, and 1911 cm^{-1} that are similar to those of **17**. This finding suggests a different reactivity of the incorporated complex compared to that in solution. Even though conversion in UiO-66 is not complete, the product that contains approx. 80 % of the substituted complex and 20 % unreacted **1**, will hereafter be referred to as UiO-66-**17b**.

The proposed mechanism for the homogenous reaction proceeds via cleavage of an Fe-S bond, along with the formation of a dinuclear species bridged by two dithiolate ligands to form the mononuclear species **18**. Both are probably hindered by the the surrounding UiO-66. Reaction with PEt_3 yielded IR absorption bands at 1983, 1945, and 1918 cm^{-1} and about 50 % conversion. The lower yield is explained by larger steric bulk of the ligand compared to PMe_3 leading to more severe pore blocking. When the reaction was performed with PPh_3, no new product was observed, even after 5 d. Clearly, the larger size of this ligand prevents its diffusion into the pores. This together with high yielding of exchange with smaller PMe_3 is an obvious indication for a homogenous distribution of the catalyst throughout the whole UiO-66 particle. If catalysts would mainly reside at the particle surface, the reaction with PPh_3 would have shown at least some substituted product. The high yield of the reaction with PMe_3 further suggests that the reaction is a true PSM-process.

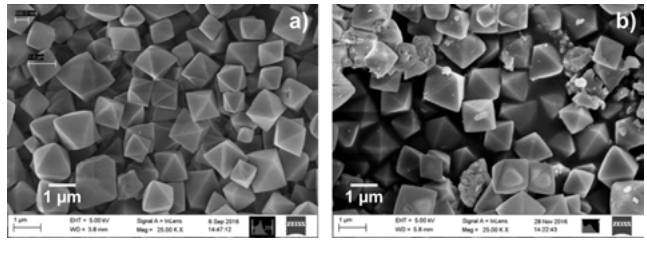

Figure 8.5. SEM images of UiO-66-**1** a) before and b) after exchange with PMe_3. Reproduced from manuscript submitted to *Chemical Communications* (Paper VI) by permission from The Royal Society of Chemistry.

8.3 Electrochemistry

The shift of IR absorption bands to lower wavenumbers of the phosphine-subsituted complexes points to an increased electron density at the iron centers, which is a result of the electron donating properties of phosphine ligands. This effect can also be studied by cyclic voltammetry. For this, UiO-66 samples were suspended together with carbon black (1:4) in 2-propanol solution containing 0.5 vol.-% Nafion®. This suspension was drop-casted onto glassy carbon electrodes and dried in air over 24 h. This method has shown to produce the best CVs for non-conductive MOFs.[151]

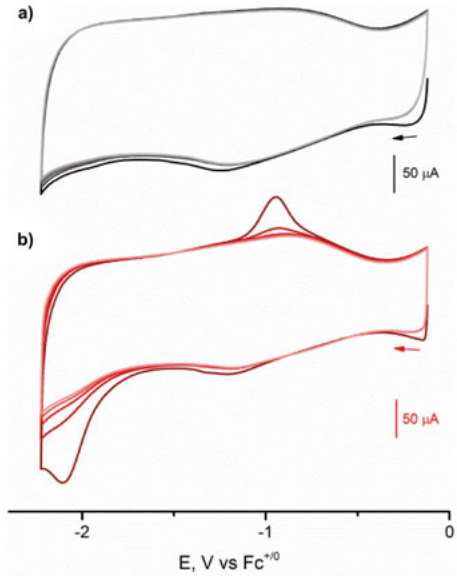

Figure 8.6. CVs (1st to 5th scan) of a) UiO-66-**1** and b) after reaction with PMe_3 (UiO-66-**17b**). The first five scans are visualized. All CVs were recorded in MeCN with 0.1 M $TBAPF_6$ at a scan rate of 1 Vs^{-1}. Reproduced from manuscript submitted to *Chemical Communications* (Paper VI) by permission from The Royal Society of Chemistry.

Reference UiO-66-**1** displays a partially reversible redox process at a formal $E_{1/2} = -1.05$ V ($E_{p,c} = -1.18$ V and $E_{p,a} = -0.91$ V (Figure 8.6 a)). As described in the previous chapter, this feature is ascribed to the reduction of incorporated **1** and the low electrochemical response compared to CVs in homogenous solution is a result of the insulating UiO-66.

After reaction with PMe_3, the cathodic reduction potential $E_{p,c}$ for UiO-66-**17b** moves to -2.05 V, as expected. The higher electron density due to phosphine substitution is the reason for the shift towards more negative reduction potential. This redox event is irreversible and corresponds to the reduction of $Fe_2(dcbdt)(CO)_4(PMe_3)_2$ (**17b**) in UiO-66. Due to irreversibility, the reduction feature at -2.05 V looses intensity over consecutive scans (Figure 8.6 b)). In addition to the new redox event, also the reduction wave for **1** is observed in the CV of UiO-66-**17b**. Since UiO-66 is non-conductive, the observed electrochemical response only comes from redox active species at the surface of the particles. The fact that redox features for both **1** and the substitution product $Fe_2(dcbdt)(CO)_4(PMe_3)_2$ are observed in the CV suggests that full conversion to the disubstituted product is not only prevented in the interior of the particle, but also in its periphery. The unsubsituted, surface-near fraction of complex **1** might reside in the tetrahedral pores of UiO-66 that leave less space for ligand substitution.

8.4 Protonation of UiO-66-**17b**

A higher electron density in the diiron center should also facilitate direct protonation of the complex. In order to test protonation, UiO-66-**17b** was suspended in a solution of triflic acid (11.3 mM) in MeCN and IR spectra were recorded. The samples with regular size of UiO-66 particles (800 nm) gave inconclusive results, because the particles settled rapidly in the liquid cell. Therefore, smaller crystals were grown using acetic acid as a modulator instead of benzoic acid. These crystals were about 300 nm in size. PSE and the reaction with PMe_3 were performed according to the described procedures without deviation and yielded in a similar material in terms of CO $\rightarrow$ phosphine ligand exchange yield, with the particle size as only difference. When these smaller UiO-66-**17b** crystals were suspended in the triflic acid solution, the protonation of **17b** inside UiO-66 could be followed by IR spectroscopy. Over a timescale of minutes, the absorption bands of **17b** transformed into two new peaks at ν_{CO} = 2054 and 2016 cm^{-1}. These are similar to characteristic bands for the protonated species of complex $Fe_2(bdt)(CO)_4(\mu{-}H)(PMe_3)_2$.[72] The formed hydride occupies a bridging position between the two Fe atoms. Very slow formation of the hydride species inside UiO-66 is a sign for hindered excess of the acid due to bulkyness of phosphine substituted complexes inside the pores. It is also the reason for complicated analysis of the protonation of UiO-66 in regular size, as the particles settle within the timescale of protonation.

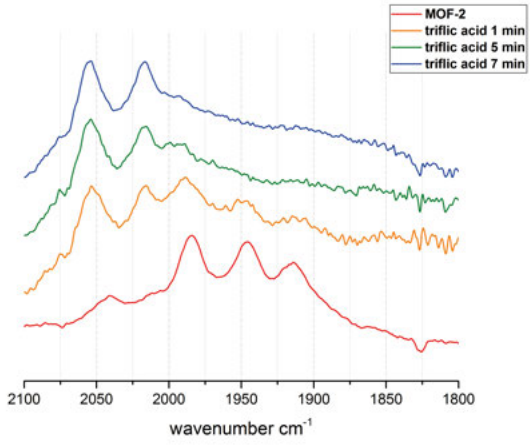

Figure 8.7. Protonation of UiO-66-**17b** with triflic acid (11.3 mM) in MeCN. For this experiment, smaller crystals of UiO-66-**17b** were prepared, as the traditional samples gave inconclusive results. Reproduced from manuscript submitted to *Chemical Communications* (Paper VI) by permission from The Royal Society of Chemistry.

8.5 Summary and Conclusion

In this chapter, the reactivity of UiO-66-**1** towards phosphine ligands was investigated. The two smaller phosphines PMe_3 and PEt_3 could successfully replace two CO ligands on the incorporated complexes. The smallest phosphine, PMe_3, gave the highest yield (80 %) and the doubly-substituted dinuclear complex **17b** was obtained as only product inside UiO-66. This demonstrates different reactivity compared to solution, were a mononuclear species is obtained as byproduct. The difference in reactivity can be attributed to the surrounding framework, which hinders rearrangements of the complex that are necessary to form the mononuclear product. UiO-66-**17b** behaves similar to other homogenous phosphine substituted [FeFe]-hydrogenase active site model complexes in terms of electrochemistry and protonation. The reduction potential shifts towards more negative potentials due to electron donating phosphine ligands and becomes irreversible. Protonation with triflic acid quantitatively forms the μ-hydride species $Fe_2(dcbdt)(CO)_4(\mu{-}H)(PMe_3)_2$ inside the MOF on the timescale of minutes. The long timescale is attributed to slow access to the interior of UiO-66.

9. Summary, Conclusion, and Outlook

In this thesis, a number of new model complexes of the [FeFe]-H_2ase active site have been prepared and characterized. Scheme 9.1 summarizes all the relevant structures.

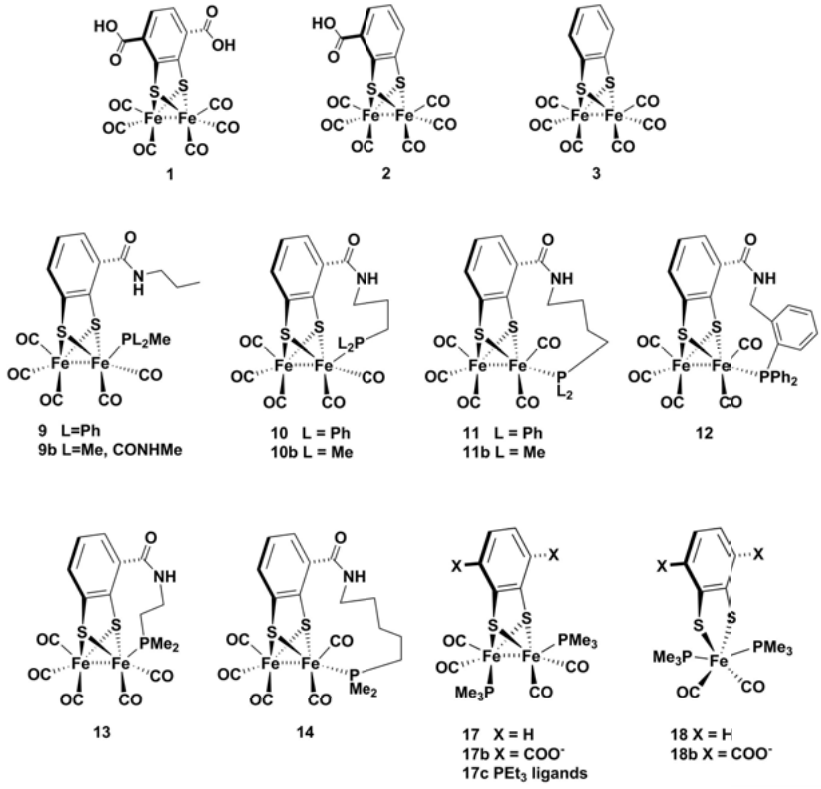

Scheme 9.1. Overview over all complexes prepared and discussed in this thesis.

In chapter 2, two new complexes with one (Fe_2(dcbdt)$(CO)_6$, **1**) or two (Fe_2(mcbdt)$(CO)_6$, **2**) carboxylic acid functions were introduced that are analogs of Fe_2(bdt)$(CO)_6$ (**3**). The carboxylates in ortho-position to the dithiolates in the bdt-bridge did not have a strong influence on the electron density in the diiron center as they show similar IR absorption bands. The reversibility of electrochemical reduction is however affected by the introduction of the carboxylates.

In Paper I, catalytic intermediates of complex **3** were investigated. Specifically, the structures of the singly-reduced complex $\mathbf{3}^{-}$ and its protonated form could be identified. The challenge for this was that the complex usually undergoes a reversible two-electron reduction that is facilitated by an inverted reduction potential of the second compared to the first reduction. A combination of transient absorption IR spectroscopy and DFT calculations allowed the distinct assignment of a singly-reduced structure with all CO ligands in terminal position with one Fe-S bond elongated.

In Paper II, the series of new model complexes was extended to complexes **10-14** holding phosphine ligands that are covalently linked to the bdt-bridge and coordinated to one iron center. The effect of these tethering ligands was analyzed in a theoretical investigation and compared to reference complex **9** holding a phosphine ligand that is not linked to the bdt-bridge. Comparison of experimental IR spectra with data obtained from the theoretical vibrational frequency analysis disclosed that the apical and the basal isomers of all complexes are present in equillibrium. Depending on the strain caused by the carbon chain between N and P in the thethering ligands, either the apical or the basal form is the lowest energy isomer. In order to study the effect of tethering ligands on the rotation of the $Fe(CO)_2(PL_3)$-subunit, a transition state search on the conversion of the apical into the basal isomer was performed for complexes **10** and **11**. The results were compared to the calculated rotational energy barriers of the reference **9** and the hexacarbonyl complex **2**. The result was that the propyl-tethered complex **10** features the largest energy barrier for the rotation. In the catalytic reduction of protons with such model complexes, a terminal hydride forming at the more basic iron center is presumed to be the most reactive intermediate. Since a terminal hydride is thermodynamically disfavored compared to a hydride in a bridging position between the two iron centers, the protonated complexes usually convert quickly into the latter form. This rearrangement is described by a rotation of the protonated $Fe(H)(CO)_2(PL_3)$-subunit. Therefore, it is an advantage to slow down the rotation by tethering phosphine ligands as they could potentially stabilize the terminal hydride. In the work presented, the protonation has not been studied yet. A combined experimental and theoretical investigation on the protonation is therefore proposed to be a future project. Another follow-up study should be performed on the singly-oxidized complex in the Fe(I)(II) redox state, which would be a closer mimic for the [FeFe]-H_2ase active site.

Chapters 4 to 8 of this thesis deal with the incorporation of model complexes **1** and **2** into metal-organic frameworks and the study of resulting MOF-catalysts.

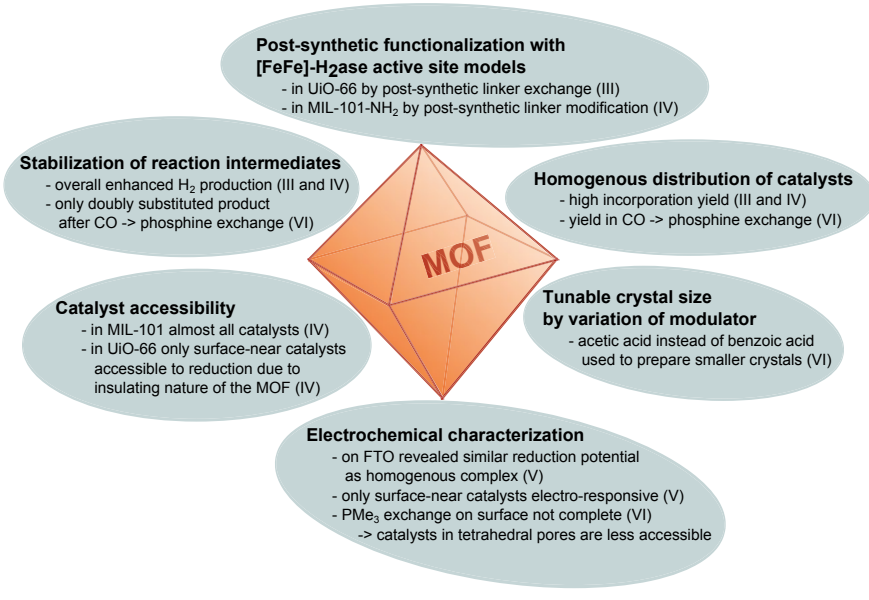

Figure 9.1. Overview over the most important findings on MOF-catalysts from the work of this thesis. References to the papers are given in (Roman numerals).

Figure 9.1 summarizes the most important findings from this work. Two different MOFs, UiO-66 and MIL-101, were chosen as hosts for catalysts **1** and **2**, respectively. In Paper III, catalyst **1** was introduced to UiO-66 by post-synthetic linker exchange. The resulting MOF-catalyst showed increased photochemical hydrogen production compared to the homogenous reference. Similar to this, larger hydrogen production yields were observed when catalyst **2** was incorporated into MIL-101 by post-synthetic functionalization of amino-groups on the linkers in the MOF (Paper IV). Enhanced photochemical hydrogen production is in both cases attributed to stabilization of catalytic intermediates by the surrounding MOF framework. Mimicking the stabilizing effect on the active site that is enabled by the protein matrix in the [FeFe]-H_2ase enzyme was one of the main objectives of this thesis work.

In chapter 5, the dual functionalization of UiO-67 with both catalyst and photosensitizer was investigated. Different methods for the preparation of the bifunctional material were tested. Due to a size-mismatch of linkers, incorporation of the catalyst was disfavored and occured only at low yields. Two structures of catalysts with matching size to the biphenyl linkers in UiO-67 are proposed in chapter 5. The synthesis of those and their incorporation into UiO-67 is a potential future project. Interestingly, functionalized UiO-67 containing open bpy-sites did not show any hydrogen formation. In contrast, UiO-67 based on biphenyl linkers and functionalized with catalyst **1** and pho-

tosensitizer turned out to be an active photocatalyst. It seems that open bpy sites function as trap-states for electrons. Protonation along with reduction was observed in electrochemical analysis of the linker. If this happens under photocatalysis conditions, electrons will be prevented from being transfered to the catalyst, since non-metalated bpy-linkers are readily reduced by the photosensitizer and keep the electrons.

Post-synthetic linker insertion of **1** into pcn-700, yet another MOF, was also tested in chapter 5. Initial studies showed that pcn-700 is a promising candidate for co-incorporating catalyst and photosensitizer as it offers free pockets for the post-synthetic insertion of linkers with two specific sizes. In order to promote this project, a dye based on terphenyl-dicarboxylic acid with matching reduction potential to the catalyst needs to be designed.

In a detailed study, catalyst accessibility in MIL-101 and UiO-66 was investigated in chapter 6. For this, chemical reduction of the MOF-catalysts with cobaltocene was performed and followed by IR spectroscopy. In MIL-101, the majority of incorporated catalysts (approx. 80 %) could be reduced. In addition to this finding, also almost all catalysts were degraded after the photochemical hydrogen evolution experiment in Paper IV. Together, these findings allow the conclusion that in MIL-101 almost all catalysts are accessible to reduction and thus participate in catalysis. MIL-101 possesses relatively large pores that enable diffusion of both cobaltocene and photoreduced $[Ru(bpy)_3]^+$ into the pores. In contrast, UiO-66 has much narrower pore windows that definitely do not allow penetration of the photosensitizer. In the redox-titration with cobaltocene, no change in IR absorption bands could be observed for UiO-66-**1** (Paper IV). This indicates that the majority of incorporated catalysts could not be reduced. It can be concluded, that the catalysts are homogenously distributed over the crystal and only surface-near catalysts are redox-active. The fraction of those was too small to be detected in the in-situ IR chemical reduction experiment. Electron transfer between incorporated catalysts is disfavored due to the insulating nature of UiO-66. Electrochemical analysis of UiO-66-**1** thin films (Paper V) supported this notion. Only a low electrochemical response could be observed in cyclic voltammograms of the films.

A follow-up study on the redox-titration experiment was presented in chapter 6. For this, UiO-66-**1** was soaked in a cobaltocenium solution and drop-casted on the Pt-net working electrode of a spectro-electrochemical cell. When a potential that is sufficiently negative to reduce cobaltocenium was applied to the cell, a shift in the IR spectrum of UiO-66-**1** to lower wavenumbers was observed. The resulting spectrum corresponds to the doubly-reduced complex $\mathbf{1}^{2-}$. In this experiment, approx. 50 % of the complexes could be reduced, indicating that cobaltocenium can penetrate the pores of UiO-66 and function as a redox-shuttle to reduce catalysts buried deeper in the crystals. The reason that reduction of the majority of catalysts is not observed when cobaltocene

was added in the redox titration is most likely the formation of stable ion-pairs of oxidized cobaltocene and reduced catalyst. These are formed when cobaltocene reduces surface-near catalysts and they block further cobaltocene molecules from entering the interior of the crystal.

Finally, [FeFe]-H_2ase active site model chemistry inside UiO-66 was investigated in chapter 8 (Paper VI). CO $\rightarrow$ phosphine ligand exchange has been explored for homogenous model complexes before. For bdt-bridged complexes like **3**, two reaction products are typically observed: The dinculear, disubsituted complex $Fe_2(bdt)(CO)_4(PMe_3)_2$ **17** along with the mononuclear species $Fe(bdt)(CO)_2(PMe_3)_2$ **18**. In contrast to this, UiO-66 around complex **1** prevents the formation of the mononuclear species and only the disubstituted product **17b** is formed. It is concluded that the reaction mechanism is influenced by the surrounding framework. For the formation of the mononuclear species, structural rearrangements of the complex along with the formation of a dimer have been suggested in literature. These are apparently prevented when the complex is incorporated in UiO-66. In terms of reduction potential and protonation behavior, UiO-66-**1** features similarities to the homogenous complex. Due to the electron-donating effect of phosphines, the reduction potential of **17b** shifts to more negative values and the reduction becomes irreversible. At the same time, protonation with triflic acid is enabled and yields the μ-hydride species $Fe_2(bdt)(\mu{-}H)(CO)_4(PMe_3)_2$. From the cyclic voltammogram recorded of the phosphine-exchanged material it is clear that not all catalysts at the crystal surface are accessible to the reaction. The structure of UiO-66 consists of both octrahedral and tetrahedral pores. The non-reactive catalysts probably occupy the tetrahedral pores that leave less space for chemical modification.

An interesting finding in Paper VI was that variation of the modulator during solvothermal synthesis of UiO-66 has an influence on its crystal size. When acetic acid was used instead of benzoic acid, three times smaller crystals were obtained. PSE and CO $\rightarrow$ phosphine exchange on the smaller crystals yielded comparable products as the crystals of regular size. In a future project, it could be interesting to prepare even smaller UiO-66 crystals, functionalize them with the catalyst and study the influence of crystal size on photocatalysis. The hypothesis that only surface-near catalysts are active in UiO-66 predicts that the MOF-catalyst with smallest crystal size would be most active, since the active catalyst portion will increase with decreasing crystal size.

An alternative strategy would be the development redox-active MOFs. For increasing the "conductivity" of MOF-catalysts, they should be built up exclusively from redox active linkers and possibly contain smaller metal-clusters such as the chromium-cluster of MIL-101. Such a design would allow electron transport (probably through a hopping mechanism) between the linkers.

In prior research, porphyrine linkers have been used for creating redox-active MOFs. In chapter 5 of this thesis it was found that open bpy-sites in UiO-67 are trapping electrons. Since the reduction potential of the co-incorporated catalyst is very close to the potential of the protonated and reduced bpy linker, further electron transport is disfavored. If a catalyst with lower overpotential would be used instead of catalyst **1**, a bpy-functionalized UiO-67 MOF could potentially provide sufficient conductivity to allow redox accessibility of all incorporated functionalities. This is another future project that should be considered.

The potential of redox-shuttles for increasing catalyst accessibility to reduction has been shown by the spectro-electrochemical experiment on UiO-66-**1** in chapter 6. Similar to this, redox-shuttles could be used in non-conductive MOFs with larger pore size (e.g. UiO-67). Also the preparation of MOFs with dual functionality (catalyst plus photosensitizer) as initialized in chapter 5 should be followed up. Especially pcn-700 seems to be an interesting platform for dual functionalization since it allows the stepwise insertion of linkers with a specific size to its empty pockets.

Several important steps have been made towards a MOF-catalyst based photoelectrochemical cell as decribed in the introduction of this thesis. This includes the functionalization of various MOFs with catalyst and photosensitizers. The successful preparation and functionalization of UiO-66 thin films (Paper V) is a promissing example of how a MOF-catalyst can be interfaced with an electrode. Summarizing all the experiments and results of this thesis suggests the development of thin films of a bifunctional MOF containing both a catalyst and photosensitizer. In order to achieve good redox-accessibility, the MOF crystals should be as small as possible and the film should only consist of a monolayer of MOF crystals. Such a system would combine all the best properties a MOF-photocatalyst can deliver.

The aim of my thesis was to contribute to a better understanding of how molecular model systems of the [FeFe]-H_2ase active site can more closely mimic the effects of the outer coordination sphere. The two strategies for mimicking the outer coordination sphere effects presented in this thesis are likely applicable to other enzyme model systems. There are still several unanswered questions and many proposed projects to follow up on this work. I hope that my thesis will serve as inspiration for future research in enzyme active site model chemistry and in the development of MOF-catalysts.

10. Acknowledgements

My PhD work has been supported by many people and I would like to thank everyone who has been involved in the one or another way. Special thanks go to the following people:

My main supervisor Sascha Ott for giving me so much trust and freedom throughout the years. With all the conferences, research trips, lunches, and conversations we had, this PhD has been so much more colorful than just hard work in the lab. You have been a great guide for me in many ways and I enjoyed very much working together with you. Thank you also for proof-reading my thesis while being at the Pacific Ocean in San Diego.

My co-supervisor Matthias Stein for teaching me how to perform DFT calculations and all the support he gave me later on. Thank you for proof-reading parts of my thesis. Thank you also for being such a great and generous host the many times I have visited Magdeburg.

Reiner Lomoth, for being my second co-supervisor and supporting me with all questions around electrochemistry and (academic) life in general.

Seth M. Cohen, our long-term collaborator on many of the MOF projects. All the discussions and meetings with you have been very inspirational and I enjoyed my stay in San Diego visiting your lab very much. Also thank you, Honghan Fei, for being part of this fruitful collaboration.

Leif Hammarström for the collaborations we had together and for being someone to look up to with all the things you manage at the same time and the deep knowledge you have.

Stenbjörn Styring for being a great source of motivation and for leading CAP in such a great way! Thanks for all the mentoring and for trusting me with the organization of ISF-1-Young.

Andreas Orthaber for being a great collaborator and for all the inspirational conversations we had.

Our collaboration partners from Stockholm University, Belén Martin-Matute and Vlad Pascanu for a great project we had together.

All the people from our group being involved in the different projects that constitute this thesis: Mohammad Mirmohades, Souvik Roy, Edgar Mijangos, Somnath Maji, and Andreas Wagner.

Project students that have been working with me throughout the years: Lea Meier, Maximilian Schmucker, Johann Pann, and Carlota Bozal-Ginésta.

Hanna Ellis and Mohammad Mirmohades, I thank both of you for being there for me all the years, for all the time we spent together inside and outside of the lab and for being really great friends. Every PhD student should have fellows like you around!!!

Kjell Jorner for correcting my Swedish summary and for all the great discussions we had together at lunch since you work at Ångström.

All the amazing people that have accompanied me in the different periods of my PhD and who provided a lot of motivation and fun: Katharina Brinkert, Christian König, Huan Ma, Djawed Nauroozi, Burkhard Zietz, Jens Föhlinger, Travis White, Hong-Yan Wang, Sven Johansson, Susanne Söderberg, Jessica Stålberg, and many others. Thank you all for being good friends and colleagues.

Felix Ho and Daniel Brandell for offering me the possibility to teach and get to know the other side of academia. I think that teaching is the best way of learning about the topic and yourself!

All the past and present members of the Synthesis group for creating such a good atmosphere in and around the lab. Especially Anders Thapper, Eszter Borbas, Keyhan Esfandiarfard, Muhammad Anwar Shameem, Michele Bedin, Giovanny Parada, Elisabeth Öberg, and Anna Arkhypchuk.

SOFI, Å-Forsk, Kungliga Vetenskapsakademin, and the Liljewalchs Foundation for supporting conference trips and my stay in San Diego.

My parents and my brother Armin for always supporting me and for listening to all these weird things I talked about on the phone like MOFs and artificial photosynthesis.

My deepest gratitute goes to Matthias, who always had to deal with my temper going up and down. Thank you for all the support (computer, proof-reading…) and all the motivation and belief in me!!!

My sunshine Carla Linnéa for being the cutest person on earth and making me happy everyday when I come home or just think about you :-) And finally the little person that started growing inside me while I have been writing this thesis. I am so much looking forward to meet you soon!

11. Populärvetenskaplig svensk sammanfattning

I tider av växande ekonomisk utveckling och befolkningsökning är efterfrågan på energi enorm. Samhället idag är fortfarande huvudsakligen beroende av fossila bränslen, men betydande framsteg har också gjorts i den tekniska utvecklingen av alternativa energikällor.

Vind- och solenergi används redan på många ställen till att vinna el på ett hållbart sätt. Problemet är att det är svårt att lagra elen. I det här sammanhanget framstår vätgas som ett attraktivt sätt att lagra energi. Vätgas kan produceras direkt från vatten och på grund av den starka bindningsenergi mellan väteatomer kan en molekyl vätgas spara väldigt mycket energi.

Artificiell fotosyntes är ett forskningsområde som behandlar utvecklingen av nya katalysatorer inspirerade av naturen. Denna forskning också kallas för biomimetisk katalys. Syftet är att dela vatten med hjälp av solljus och katalysatorer i vätgas och syrgas (ekvation 11.1).

$$2\,H_2O \rightarrow O_2 + 2\,H_2 \tag{11.1}$$

Ekvationen kan delas in i två delreaktioner: Den första innebär uppdelningen av vatten till molekylärt syre, protoner och elektroner

$$2\,H_2O \rightarrow O_2 + 4\,H^+ + 4\,e^- \tag{11.2}$$

I det andra steget kombineras protoner och elektronerna och bilda vätgas.

$$2\,H^+ + 2\,e^- \rightarrow H_2 \tag{11.3}$$

Det är redan idag tekniskt möjligt att använda el för att dela vatten i vätgas och syre. Processen uppkallas för *elektrolys* och genomförs med hjälp av en platinakatalysator. Problemet är att platina är en ädelmetall och mycket dyr och därför är det viktiga att utveckla nya katalysatorer baserade på billigare råvaror.

En katalysator kan liknas vid en vigselförrätare på molekylär nivå. Två personer (reaktanterna) går till vigselförrätaren (katalysatorn) och gifter sig. Resultatet är ett registrerat äktenskap och de två män bildar ett gift par (reaktionsprodukten). På samma sätt blir väte, protoner och elektroner förbundna med varandra och bildar vätgas. Eftersom denna reaktion inte händer spontant behövs en katalysator som knytar ihop de två.

Detta avhandlingen handlar om att upprätta och undersöka nya biomimetiska katalysatorer som kan producera vätgas.

[FeFe]-hydrogenas enzymer är naturliga katalysatorer som producerar väte från protoner och elektroner på ett mycket effektivt sätt. Dessa enzymer finns i gröna alger och vissa cyano-bakterier.

I min forskning är det viktigt att den exakta funktionen hos enzymerna kan förstås och att reproducerar biomimetiska modellkomplex med naturen som förebild. Dessa modeller kan i framtiden vara lovande katalysatorer för framställning av väte.

Det så kallade aktiva centrumet av hydrogenas-enzymer består av två järnatomer som är förbundna med så kallade ligander. Det aktiva centrumet är också inbäddad i en protein. Det finns redan många modellkomplex som liknar [FeFe]-hydrogenas-enzymernas aktiva centrumet, men dessa är hittills inte så effektiva som enzymet. Ett noggrann undersökning av enzymens kristallstruktur har visat att det inte bara själva järnkomplexet spelar en viktig roll, utan också proteinet som omger det aktiva centrumet. Naturen skyddar på detta sätt katalysatorn, som en frukt är omgivet av ett skal. Dessutom gör proteinen i enzymet mycket mer: det interagerar med järnkomplexet och styr på så sett den katalytiska processen. Proteinen stabiliserar järnkomplexet i ett specifikt form som kallas för nyckel-tillsåndet. Denna form är mycket reaktiv och gör att hydrogenas-enzymer är så effektiver katalysatorer för produktionen av vätgas.

Denna avhandling visar två olika vägar att återskapa dessa effekter i modellsystem.

Det första alternativet använder en specifik ligand som installeras i i modellsystemet. Den slingar runt komplexet som en arm och komplexet har därigenom begränsad möjligjet att röra på sig och hålls fast i ett specifikt tillstånd, precis som proteinen gör det i enzymet. Ett antal nya modellkomplex med detta motiv presenteras i avhandlingen. Deras potential att stabilisera nyckeltillståndet utvärderas. Studien visar att införandet av sådana ligander faktiskt begränsar rörligheten hos katalysatorn. En lovande kandidat för ytterligare katalytiska studier har identifierats.

Det andra alternativet är inriktad på att installera modellkomplex i tredimensionella, porösa material. Dessa är metall-organiska ramverk (så kallade MOFs, eng. metal-organic framework). En MOF är som ett stort hus med en mängd lika stora rum. Alla rum har fönster och dörrar i en viss storlek, och alla rum är anslutna till varandra. MOFs kan monteras som ett modulärt hus och erbjuder därmed många möjligheter för integrering av katalysatorn. Samtidigt möjliggör den modulära designen en relativt snabb syntes och materialet kan också justeras efteråt för att få önskade egenskaper. Detta på samma sätt som ett rum i ett hus kan anpassas efter att huset har byggts. Väggarna kan målas i en viss färg och möbler kan placeras i rummet.

Installationen av biomimetiska katalysatorer i olika så kallade MOFs har testats i denna avhandling. I exemplet med vigselförrätaren skulle en MOF nu vara stadshuset. Det är så stort att hundratals vigselförrätarna kan få plats

och de kan nu gifta så många par på samma gång som möjligt. Eftersom det är okänt under vilka villkor vigselförrätarna arbetar bäst kan flera stadshus av olika storlek och med olika inredda rum byggas.

Studierna i denna avhandlingen har visat att de olika MOFs kan stabilisera katalysatorn och därmed bidra till en högre katalytisk aktivitet. Det materialer som utvecklades kan producera vätgas. Problemet med de använda MOFs är dock att inte alla katalysatorerna i materialet är lättillgängliga, och beroende på utformningen av MOF, en stora delar av materialet är inaktivt.

I stadshus nr. 1 visade det sig att bara vigeslförrätarna besöktes som satt i rummet vid ytterdörren. Det fanns långa köer framför deras dörrar och bara få människor gick vidare in i byggnaden för att träffa de andra vigselförrätarna. Detta beror på de ändlöst långa och vindlande korridorerna i stadshus nr. 1. Dessutom finns det ingen WLAN i huset och även telefonförbindelsen mellan de olika rummen fungerar inte. Därför kan vigselförrätarna som har en hel del att göra, inte få hjälp av sina kollegor.

Stadshus nr. 2 har betydligt större lokaler och även korridorerna är bredare. Därför kunde många fler människor bli gifta då nästan alla vigselförrättare fanns tillgängliga. Men även här skulle det vara bättra med en telefonförbindelse mellan de enskilda rummen så att alla vigselförrätarna kan samarbeta och bli ännu effektivare.

Överfört till MOF innebär detta att de är icke-ledande material. Det vill säga att elektronerna inte kan transporteras genom materialet och därför inte kan nå alla katalysatorer.

I MOF nr. 1 som har mycket mindre porer, var således en stor del av de inbyggda katalysatorerna inaktiva. MOF nr. 2 har signifikant större porer och därför var nästan alla katalysatorer inblandade i produktionen av vätgas. Men också här skulle konduktivitet bidra till en betydande förbättring av den katalytisk processen genom att möjliggöra samverkan mellan katalysatorerna.

I framtiden ska därför tillgängligheten till katalysatorerna förbättras. För att göra det är det nödvändigt att framställa MOFs med mindre storlek än de som har framställts i avhandlingen. Dessutom bör ledande strukturer utvecklas som gör det möjligt att transportera elektroner genom hela materialet.

12. Populärwissenschaftliche Zusammenfassung

In Zeiten stetig wachsender wirtschaftlicher Entwicklung und Bevölkerung ist der Energiebedarf enorm. Unsere Gesellschaft ist heute noch immer hauptsächlich abhängig von fossilen Brennstoffen, obwohl inzwischen deutliche Fortschritte in der technologischen Entwicklung alternativer Energiequellen gemacht wurden. Wind- und Sonnenenergie werden bereits heute an vielen Orten genutzt, um nachhaltig elektrischen Strom zu gewinnen. Jedoch ist es schwierig, Strom zu lagern. Wasserstoff bietet sich als Energieträger deshalb an, weil er direkt aus Wasser hergestellt werden kann und aufgrund der starken Bindungsenergie zwischen Wasserstoffatomen besonders viel Energie speichert. Mit Hilfe von Brennstroffzellen lässt sich die gespeicherte Energie jederzeit wieder in elektrischen Strom umwandeln.

Die Verwendung von Strom zur Aufspaltung von Wasser in Wasserstoff und Sauerstoff ist bereits heute technisch möglich. Der zugrundeliegende Prozess nennt sich Elektrolyse und wird mit Hilfe eines Platin-Katalysators durchgeführt. Das Problem dabei ist, dass Platin ein Edelmetall und sehr teuer ist. Daher ist es wichtig, alternative Katalysatoren auf Basis günstigerer Rohstoffe zu entwickeln.

Artifizielle Photosynthese ist ein Forschungsgebiet das sich mit der Entwicklung von neuartigen Katalysatoren nach dem Vorbild der Natur beschäftigt. Dabei soll Wasser (H_2O) mit Hilfe von Sonnenlicht in Wasserstoff (H_2) und Sauerstoff (O_2) gespalten werden (Gleichung 12.1).

$$2\,H_2O \rightarrow O_2 + 2\,H_2 \tag{12.1}$$

Die Gleichung lässt sich in zwei Teilreaktionen aufteilen. Die erste ist die Spaltung von Wasser in molekularen Sauerstoff, Protonen und Elektronen:

$$2\,H_2O \rightarrow O_2 + 4\,H^+ + 4\,e^- \tag{12.2}$$

Im zweiten Schritt werden Protonen und Elektronen miteinander verbunden und bilden dabei molekularen Wasserstoff:

$$2\,H^+ + 2\,e^- \rightarrow H_2 \tag{12.3}$$

Ein Katalysator ist im Grunde genommen nichts anderes als ein Standesbeamter auf molekularer Ebene. Zwei Menschen (die Reaktionspartner) gehen zum Standesbeamten (dem Katalysator) und lassen sich trauen. Das Ergebnis

ist eine eingetragene Ehe und die beiden Menschen bilden ein Ehepaar (das Reaktionsprodukt). Im Fall von Wasserstoff werden Protonen und Elektronen – beides Bestandteile von Wasser – miteinander verbunden, um molekularen Wasserstoff zu bilden. Da diese Reaktion nicht spontan geschieht, braucht es einen Katalysator, der beide miteinander verbindet.

Die vorliegende Arbeit befasst sich mit der Herstellung und Untersuchung biomimetischer Katalysatoren zur Herstellung von Wasserstoff. [FeFe]-Hydrogenase Enzyme sind natürliche Katalysatoren, die unter energetisch günstigen Bedingungen Wassertoff aus Protonen und Elektronen erzeugen können. Sie kommen in grünen Algen und bestimmten Bakterien vor. In meiner Forschung ist es wichtig, die Funktionsweise der Enzyme genau zu verstehen und biomimetische Modellkomplexe nach dem Vorbild der Natur herzustellen. Diese Modelle könnten dann in Zukunft kostengünstige Katalysatoren für die Herstellung von Wasserstoff werden.

Das so genannte Aktive Zentrum der [FeFe]-Hydrogenasen besteht aus zwei Eisenatomen, die durch sogenannte Liganden miteinander verbunden sind. Das Aktive Zentrum ist in ein Protein eingebettet. Es gibt bereits viele Modellkomplexe, die das Aktive Zentrum der [FeFe]-Hydrogenasen nachstellen. Jedoch sind diese bei Weitem nicht so effektiv wie das Enzym. Durch die genaue Untersuchung der Kristallstruktur des Enzyms konnte herausgefunden werden, dass nicht nur der Eisenkomplex eine wichtige Rolle spielt, sondern auch das ihn umgebende Protein. Die Natur schützt damit den Katalysator, so wie bei einer Nuss die Frucht in eine Schale gehüllt ist. Jedoch kann das Protein im Enzym noch einiges mehr: Es interagiert mit dem Eisenkomplex und dirigiert damit den Katalyseprozess. In der vorliegenden Doktorarbeit werden zwei Wege aufgezeigt, diese Effekte in Modellsystemen nachzustellen.

Die erste Alternative befasst sich damit, einen speziellen Liganden in den Modellkomplex einzubauen, der diesen wie ein Arm umschlingt. Der Komplex soll dadurch in seiner Bewegung eingeschränkt und in einer besonders reaktiven Position festgehalten werden, genau so wie auch das Protein im Enzym das Aktive Zentrum stabilisiert. In der Arbeit werden eine Reihe neuer Modellkomplexe mit diesem Design vorgestellt und deren Potential zur Stabilisierung des Schlüssel-Intermediates erörtert. Es konnte dabei gezeigt werden, dass die Einführung solcher Liganden die Beweglichkeit des Katalysators tatsächlich einschränken kann. Es wurde ein vielversprechender Kanditat für weitere katalytische Studien identifiziert.

Die zweite Alternative orientiert sich daran, Modellkomplexe in dreidimensionale, poröse Materialen einzubauen. Diese sind Metall-organische Gerüstverbindungen (engl. metal-organic frameworks = MOFs). Ein MOF ist wie ein großes Haus mit einer vielzahl an gleich großen Räumen. Alle Räume haben Fenster und Türen in einer bestimmten Größe, und alle Räume sind miteinander verbunden. MOFs können genau wie Häuser maßgeschneidert zusammengebaut werden und bieten somit vielfältige Möglichkeiten zur Einbindung des Katalysators. Gleichzeitig erlaubt der modulare Aufbau eine vergleichsweise

schnelle Synthese und auch die nachträgliche Anpassung des Materials an die gewünschten Eigenschaften. Genau so wie die Räume in einem Haus nach dem Bau gestaltet werden können. Die Wände können in einer bestimmten Farbe gestrichen, und Möbelstücke hereingestellt werden.

Der Einbau der biomimetischen Katalysatoren in verschiedene MOFs wurde in dieser Arbeit erprobt und erfolgreich durchgeführt. Im Beispiel mit dem Standesbeamten wäre ein MOF nun das Standesamt. Es ist besonders groß, damit hunderte von Standesbeamten darin Platz haben und möglichst viele Paare zur gleichen Zeit miteinander verheiraten können. Da nicht bekannt ist, unter welchen Bedingungen die Standesbeamten am besten arbeiten, wurden gleich mehrere Standesämter mit unterschiedlich eingerichteten Räumen von unterschiedlicher Größe gebaut.

Die Studien in dieser Arbeit haben gezeigt, dass die unterschiedlichen MOFs den Katalysator stabilisieren können und somit zu höherer Aktivität beitragen. Die hergestellten Materialien konnten Wasserstoff erzeugen. Das Problem mit den verwendeten MOFs ist jedoch, dass nicht alle eingebauten Katalysatoren gleich gut erreichbar sind und je nach Design bleiben große Teile des Materials inaktiv. Im Standesamt Nr. 1 werden vor allem die Beamten aufgesucht, deren Zimmer gleich an der Eingangstür liegen. Es bilden sich lange Schlangen vor deren Türen und nur wenige Menschen gehen weiter in das Gebäude hinein. Das liegt an den endlos langen und verwinkelten Korridoren. Außerdem gibt es kein WLAn im Haus und auch die Telefonverbindung zwischen den Räumen funktioniert nicht. Daher können sich die Standesbeamten, die besonders viel zu tun haben, nicht bei ihren Kollegen melden und um Unterstützung bitten. Standesamt Nr. 2 hat deutlich größere Räume und auch die Korridore sind breiter. Daher können viel mehr Menschen auch ins Innere gelangen und die Standesbeamten dort aufsuchen. Doch auch hier wäre eine Telefonverbindung zwischen den einzelnen Zimmern hilfreich, damit die Standesbeamten besser zusammenarbeiten und noch effektiver werden können.

Übertragen auf die MOFs bedeutet dies, dass diese nicht leitfähig sind. Das heißt, dass die Elektronen nicht zu allen Katalysatoren gelangen können. In MOF Nr. 1, welches deutlich kleinere Poren hat, war daher ein Großteil der eingebauten Katalysatoren nicht aktiv. MOF Nr. 2 hatte deutlich größere Poren und daher waren fast alle Katalysatoren an der Produktion von Wasserstoff beteiligt. Doch auch hier wäre Leitfähigkeit eine deutliche Verbesserung, um ein besseres Zusammenspiel der Katalysatoren zu ermöglichen.

Um die Erreichbarkeit der Katalysatoren in Zukunft zu verbessern, wird es nötig sein kleinere MOF-Kristalle herzustellen. Außerdem sollten Strukturen entwickelt werden, die Elektronentransfer innerhalb des Materials ermöglichen. Das beste Standesamt wäre eines, in dem alle Räume eine Tür nach draußen haben.

Bibliography

[1] U. Nations, Goal 7: Ensure access to affordable, reliable, sustainable and modern energy for all. http://www.un.org/sustainabledevelopment/energy/ (visited on 03/29/2017).

[2] J. A. Turner, *Science* **1999**, *285*, 687–689.

[3] N. Stern, *American Economic Review* **2008**, *98*, 1–37.

[4] L. Hammarstrom, *Chem* **2016**, *1*, 515–516.

[5] NREL, Best Research-Cell Efficiencies, tech. rep., **2016**.

[6] M. A. Green, *Journal of Materials Science: Materials in Electronics* **2007**, *18*, 15–19.

[7] M. I. Hoffert, K. Caldeira, G. Benford, D. R. Criswell, C. Green, H. Herzog, A. K. Jain, H. S. Kheshgi, K. S. Lackner, J. S. Lewis, H. D. Lightfoot, W. Manheimer, J. C. Mankins, M. E. Mauel, L. J. Perkins, M. E. Schlesinger, T. Volk, T. M. L. Wigley, *Science* **2002**, *298*, 981–987.

[8] M. Z. Jacobson, *Energy Environ. Sci.* **2009**, *2*, 148–173.

[9] IPCC, Climate Change 2014 Synthesis Report Summary for Policymakers, tech. rep., **2014**.

[10] REN21, Renewables 2015 Global Status Report, tech. rep., **2015**.

[11] K. Aleklett, M. Höök, K. Jakobsson, M. Lardelli, S. Snowden, B. Söderbergh, *Energy Policy* **2010**, *38*, 1398–1414.

[12] U. Strandberg, *Energy Policy* **2010**, *38*, 1227–1228.

[13] L. Lohmann, *Carbon Trading – A Critical Conversation on Climate Change, Privatisation and Power*, 1st ed., Dag Hammarskjöld Foundation, **2006**.

[14] N. Armaroli, V. Balzani, *Energy for a Sustainable World*, WILEY-VCH Verlag, **2011**.

[15] V. Balzani, A. Credi, M. Venturi, *ChemSusChem* **2008**, *1*, 26–58.

[16] S. Styring, *Faraday Discuss.* **2012**, *155*, 357–376.

[17] T. Faunce, S. Styring, M. R. Wasielewski, G. W. Brudvig, A. W. Rutherford, J. Messinger, A. F. Lee, C. L. Hill, H. deGroot, M. Fontecave, D. R. MacFarlane, B. Hankamer, D. G. Nocera, D. M. Tiede, H. Dau, W. Hillier, L. Wang, R. Amal, *Energy Environ. Sci.* **2013**, *6*, 1074–1076.

[18] G. M. Whitesides, G. W. Crabtree, *Science* **2007**, *315*, 796–798.

[19] U. Eberle, M. Felderhoff, F. Schüth, *Angew. Chem. Int. Ed.* **2009**, *48*, 6608–6630.

[20] F. Schüth, *Chem. Ing. Tech.* **2011**, *83*, 1984–1993.

[21] S. Dunn, *Int. J. Hydrogen Energy* **2002**, *27*, 235–264.

[22] G. W. Crabtree, M. S. Dresselhaus, M. V. Buchanan, *Physics Today* **2004**, *57*, 39–44.

[23] B. C. R. Ewan, R. W. K. Allen, *Int. J. Hydrogen Energy* **2005**, *30*, 809–819.

[24] G. Ciamician, *Science* **1912**, *36*, 385–394.

[25] H. C. V. Baeyer, *The Sciences* **2000**, *40*, 12–15.

[26] Z. Guo, F. Zhou, J. Hao, W. Liu, *J. Am. Chem. Soc.* **2005**, *127*, 15670–15671.

[27] L. Marchetti, M. Levine, *ACS Catalysis* **2011**, *1*, 1090–1118.

[28] M. Y. Darensbourg, R. D. Bethel, *Nat Chem* **2012**, *4*, 11–13.

[29] E. I. Solomon, D. E. Heppner, E. M. Johnston, J. W. Ginsbach, J. Cirera, M. Qayyum, M. T. Kieber-Emmons, C. H. Kjaergaard, R. G. Hadt, L. Tian, *Chem. Rev.* **2014**, *114*, 3659–3853.

[30] C. E. Valdez, Q. A. Smith, M. R. Nechay, A. N. Alexandrova, *Acc. Chem. Res.* **2014**, *47*, 3110–3117.

[31] A. Magnuson, M. Anderlund, O. Johansson, P. Lindblad, R. Lomoth, T. Polivka, S. Ott, K. Stensjö, S. Styring, V. Sundström, L. Hammarström, *Acc. Chem. Res.* **2009**, *42*, 1899–1909.

[32] S. Friedle, E. Reisner, S. J. Lippard, *Chem. Soc. Rev.* **2010**, *39*, 2768–2779.

[33] R. E. Blankenship, *Molecular Mechanisms of Photosynthesis*, 2nd ed., Wiley Blackwell, **2014**.

[34] A. Fujishima, K. Honda, *Nature* **1972**, *238*, 37–38.

[35] Y. Umena, K. Kawakami, J.-R. Shen, N. Kamiya, *Nature* **2011**, *473*, 55–60.

[36] C. Zhang, C. Chen, H. Dong, J.-R. Shen, H. Dau, J. Zhao, *Science* **2015**, *348*, 690–693.

[37] J. D. Blakemore, R. H. Crabtree, G. W. Brudvig, *Chem. Rev.* **2015**, *115*, 12974–13005.

[38] S. W. Gersten, G. J. Samuels, T. J. Meyer, *J. Am. Chem. Soc.* **1982**, *104*, 4029–4030.

[39] M. D. Kärkäs, O. Verho, E. V. Johnston, B. Åkermark, *Chem. Rev.* **2014**, *114*, 11863–12001.

[40] W. Lubitz, H. Ogata, O. Rüdiger, E. Reijerse, *Chem. Rev.* **2014**, *114*, 4081–4148.

[41] J.-M. Lehn, R. Ziessel, *Proceedings of the National Academy of Sciences of the United States of America* **1982**, *79*, 701–704.

[42] H. Ozawa, M.-a. Haga, K. Sakai, *J. Am. Chem. Soc.* **2006**, *128*, 4926–4927.

[43] S. Rau, B. Schäfer, D. Gleich, E. Anders, M. Rudolph, M. Friedrich, H. Görls, W. Henry, J. G. Vos, *Angew. Chem. Int. Ed.* **2006**, *45*, 6215–6218.

[44] V. Artero, M. Chavarot-Kerlidou, M. Fontecave, *Angew. Chem. Int. Ed.* **2011**, *50*, 7238–7266.

[45] M. L. Helm, M. P. Stewart, R. M. Bullock, M. R. DuBois, D. L. DuBois, *Science* **2011**, *333*, 863–866.

[46] D. L. DuBois, *Inorg. Chem.* **2014**, *53*, 3935–3960.

[47] T. R. Cook, D. K. Dogutan, S. Y. Reece, Y. Surendranath, T. S. Teets, D. G. Nocera, *Chem. Rev.* **2010**, *110*, 6474–6502.

[48] B. A. Pinaud, J. D. Benck, L. C. Seitz, A. J. Forman, Z. Chen, T. G. Deutsch, B. D. James, K. N. Baum, G. N. Baum, S. Ardo, H. Wang, E. Miller, T. F. Jaramillo, *Energy Environ. Sci.* **2013**, *6*, 1983–2002.

[49] N. S. Lewis, D. G. Nocera, *Proceedings of the National Academy of Sciences* **2006**, *103*, 15729–15735.

[50] K. S. Joya, Y. F. Joya, K. Ocakoglu, R. van de Krol, *Angew. Chem. Int. Ed.* **2013**, *52*, 10426–10437.

[51] R. Sathre, C. D. Scown, W. R. Morrow, J. C. Stevens, I. D. Sharp, J. W. Ager, K. Walczak, F. A. Houle, J. B. Greenblatt, *Energy Environ. Sci.* **2014**, *7*, 3264–3278.

[52] A. M. Brown, L. J. Antila, M. Mirmohades, S. Pullen, S. Ott, L. Hammarström, *J. Am. Chem. Soc.* **2016**, *138*, 8060–8063.

[53] M. Schulz, M. Karnahl, M. Schwalbe, J. G. Vos, *Coord. Chem. Rev.* **2012**, *256*, 1682–1705.

[54] P. M. Vignais, B. Billoud, *Chem. Rev.* **2007**, *107*, 4206–4272.

[55] M. Frey, *ChemBioChem* **2002**, *3*, 153–160.

[56] J. W. Peters, W. N. Lanzilotta, B. J. Lemon, L. C. Seefeldt, *Science* **1998**, *282*, 1853–1858.

[57] A. Silakov, B. Wenk, E. Reijerse, W. Lubitz, *PCCP* **2009**, *11*, 6592–6599.

[58] G. Berggren, A. Adamska, C. Lambertz, T. R. Simmons, J. Esselborn, M. Atta, S. Gambarelli, J. M. Mouesca, E. Reijerse, W. Lubitz, T. Happe, V. Artero, M. Fontecave, *Nature* **2013**, *499*, 66–69.

[59] R. Lomoth, S. Ott, *Dalton Trans.* **2009**, 9952–9959.

[60] D. Schilter, J. M. Camara, M. T. Huynh, S. Hammes-Schiffer, T. B. Rauchfuss, *Chem. Rev.* **2016**, *116*, 8693–8749.

[61] C. Greco, M. Bruschi, L. D. Gioia, U. Ryde, *Inorg. Chem.* **2007**, *46*, 5911–5921.

[62] M. Bruschi, C. Greco, P. Fantucci, L. D. Gioia, *Inorg. Chem.* **2008**, *47*, 6056–6071.

[63] M. Bruschi, C. Greco, M. Kaukonen, P. Fantucci, U. Ryde, L. D. Gioia, *Angew. Chem. Int. Ed.* **2009**, *48*, 3503–3506.

[64] A. R. Finkelmann, M. T. Stiebritz, M. Reiher, *Chemical Science* **2014**, *5*, 215–221.

[65] C. Liu, J. N. T. Peck, J. A. Wright, C. J. Pickett, M. B. Hall, *Eur. J. Inorg. Chem.* **2011**, *2011*, 1080–1093.

[66] F. Gloaguen, T. B. Rauchfuss, *Chem. Soc. Rev.* **2009**, *38*, 100–108.

[67] H. Reihlen, A. Gruhl, G. v. Heßling, O. Pfrengle, *Justus Liebigs Annalen der Chemie* **1930**, *482*, 161–182.

[68] C. Tard, C. J. Pickett, *Chem. Rev.* **2009**, *109*, 2245–2274.

[69] Y. Li, T. B. Rauchfuss, *Chem. Rev.* **2016**, *116*, 7043–7077.

[70] D. Streich, M. Karnahl, Y. Astuti, C. W. Cady, L. Hammarström, R. Lomoth, S. Ott, *Eur. J. Inorg. Chem.* **2011**, *2011*, 1106–1111.

[71] T. B. Rauchfuss, S. M. Contakes, S. C. N. Hsu, M. A. Reynolds, S. R. Wilson, *J. Am. Chem. Soc.* **2001**, *123*, 6933–6934.

[72] L. Schwartz, P. S. Singh, L. Eriksson, R. Lomoth, S. Ott, *Comptes Rendus Chimie* **2008**, *11*, 875–889.

[73] M. Razavet, S. J. Borg, S. J. George, S. P. Best, S. A. Fairhurst, C. J. Pickett, *Chem. Commun.* **2002**, 700–701.

[74] Ö. F. Erdem, L. Schwartz, M. Stein, A. Silakov, S. Kaur-Ghumaan, P. Huang, S. Ott, E. J. Reijerse, W. Lubitz, *Angew. Chem. Int. Ed.* **2011**, *50*, 1439–1443.

[75] J. W. Tye, M. Y. Darensbourg, M. B. Hall, *Inorg. Chem.* **2006**, *45*, 1552–1559.

[76] M. Y. Darensbourg, E. J. Lyon, X. Zhao, I. P. Georgakaki, *Proceedings of the National Academy of Sciences* **2003**, *100*, 3683–3688.

[77] A. K. Justice, T. B. Rauchfuss, S. R. Wilson, *Angew. Chem. Int. Ed.* **2007**, *46*, 6152–6154.

[78] T. Liu, M. Y. Darensbourg, *J. Am. Chem. Soc.* **2007**, *129*, 7008–7009.

[79] S. Tschierlei, S. Ott, R. Lomoth, *Energy Environ. Sci.* **2011**, *4*, 2340–2352.

[80] M. Bourrez, R. Steinmetz, F. Gloaguen, *Inorg. Chem.* **2014**, *53*, 10667–10673.

[81] G. A. N. Felton, A. K. Vannucci, J. Chen, L. T. Lockett, N. Okumura, B. J. Petro, U. I. Zakai, D. H. Evans, R. S. Glass, D. L. Lichtenberger, *J. Am. Chem. Soc.* **2007**, *129*, 12521–12530.

[82] P. Knörzer, A. Silakov, C. E. Foster, F. A. Armstrong, W. Lubitz, T. Happe, *The Journal of Biological Chemistry* **2012**, *287*, 1489–1499.

[83] S. Ezzaher, J.-F. Capon, F. Gloaguen, F. Y. Pétillon, P. Schollhammer, J. Talarmin, R. Pichon, N. Kervarec, *Inorg. Chem.* **2007**, *46*, 3426–3428.

[84] R. Zaffaroni, T. B. Rauchfuss, D. L. Gray, L. D. Gioia, G. Zampella, *J. Am. Chem. Soc.* **2012**, *134*, 19260–19269.

[85] R. Zaffaroni, T. B. Rauchfuss, A. Fuller, L. D. Gioia, G. Zampella, *Organometallics* **2013**, *32*, 232–238.

[86] L. Schwartz, G. Eilers, L. Eriksson, A. Gogoll, R. Lomoth, S. Ott, *Chem. Commun.* **2006**, 520–522.

[87] F. Gloaguen, J. D. Lawrence, M. Schmidt, S. R. Wilson, T. B. Rauchfuss, *J. Am. Chem. Soc.* **2001**, *123*, 12518–12527.

[88] F. Gloaguen, J. D. Lawrence, T. B. Rauchfuss, M. Bénard, M.-M. Rohmer, *Inorg. Chem.* **2002**, *41*, 6573–6582.

[89] S. Ott, M. Kritikos, B. Åkermark, L. Sun, R. Lomoth, *Angew. Chem. Int. Ed.* **2004**, *43*, 1006–1009.

[90] S. Ezzaher, A. Gogoll, C. Bruhn, S. Ott, *Chem. Commun.* **2010**, *46*, 5775–5777.

[91] M. Beyler, S. Ezzaher, M. Karnahl, M.-P. Santoni, R. Lomoth, S. Ott, *Chem. Commun.* **2011**, *47*, 11662–11664.

[92] Y. Na, M. Wang, J. Pan, P. Zhang, B. Åkermark, L. Sun, *Inorg. Chem.* **2008**, *47*, 2805–2810.

[93] D. Streich, Y. Astuti, M. Orlandi, L. Schwartz, R. Lomoth, L. Hammarström, S. Ott, *Chemistry – A European Journal* **2010**, *16*, 60–63.

[94] Y. Na, M. Wang, K. Jin, R. Zhang, L. Sun, *J. Organomet. Chem.* **2006**, *691*, 5045–5051.

[95] M. L. Singleton, D. J. Crouthers, R. P. Duttweiler, J. H. Reibenspies, M. Y. Darensbourg, *Inorg. Chem.* **2011**, *50*, 5015–5026.

[96] G. Ferey, *Chem. Soc. Rev.* **2008**, *37*, 191–214.

[97] M. O'Keeffe, O. M. Yaghi, *Chem. Rev.* **2012**, *112*, 675–702.

[98] N. Stock, S. Biswas, *Chem. Rev.* **2012**, *112*, 933–969.

[99] W. Lu, Z. Wei, Z.-Y. Gu, T.-F. Liu, J. Park, J. Park, J. Tian, M. Zhang, Q. Zhang, T. G. Iii, M. Bosch, H.-C. Zhou, *Chem. Soc. Rev.* **2014**, *43*, 5561–5593.

[100] M. Eddaoudi, J. Kim, N. Rosi, D. Vodak, J. Wachter, M. O'Keeffe, O. M. Yaghi, *Science* **2002**, *295*, 469–472.

[101] M. P. Suh, H. J. Park, T. K. Prasad, D.-W. Lim, *Chem. Rev.* **2012**, *112*, 782–835.

[102] K. Sumida, D. L. Rogow, J. A. Mason, T. M. McDonald, E. D. Bloch, Z. R. Herm, T.-H. Bae, J. R. Long, *Chem. Rev.* **2012**, *112*, 724–781.

[103] F. Jeremias, V. Lozan, S. K. Henninger, C. Janiak, *Dalton Trans.* **2013**, *42*, 15967–15973.

[104] L. E. Kreno, K. Leong, O. K. Farha, M. Allendorf, R. P. V. Duyne, J. T. Hupp, *Chem. Rev.* **2012**, *112*, 1105–1125.

[105] P. Horcajada, R. Gref, T. Baati, P. K. Allan, G. Maurin, P. Couvreur, G. Férey, R. E. Morris, C. Serre, *Chem. Rev.* **2012**, *112*, 1232–1268.

[106] J. Lee, O. K. Farha, J. Roberts, K. A. Scheidt, S. T. Nguyen, J. T. Hupp, *Chem. Soc. Rev.* **2009**, *38*, 1450–1459.

[107] L. Ma, C. Abney, W. Lin, *Chem. Soc. Rev.* **2009**, *38*, 1248–1256.

[108] M. Yoon, R. Srirambalaji, K. Kim, *Chem. Rev.* **2012**, *112*, 1196–1231.

[109] H. Li, M. Eddaoudi, M. O'Keeffe, O. M. Yaghi, *Nature* **1999**, *402*, 276–279.

[110] G. Ferey, M. Latroche, C. Serre, F. Millange, T. Loiseau, A. Percheron-Guegan, *Chem. Commun.* **2003**, 2976–2977.

[111] G. Férey, C. Mellot-Draznieks, C. Serre, F. Millange, J. Dutour, S. Surblé, I. Margiolaki, *Science* **2005**, *309*, 2040–2042.

[112] J. H. Cavka, S. Jakobsen, U. Olsbye, N. Guillou, C. Lamberti, S. Bordiga, K. P. Lillerud, *J. Am. Chem. Soc.* **2008**, *130*, 13850–13851.

[113] L. Valenzano, B. Civalleri, S. Chavan, S. Bordiga, M. H. Nilsen, S. Jakobsen, K. P. Lillerud, C. Lamberti, *Chem. Mater.* **2011**, *23*, 1700–1718.

[114] M. J. Katz, Z. J. Brown, Y. J. Colon, P. W. Siu, K. A. Scheidt, R. Q. Snurr, J. T. Hupp, O. K. Farha, *Chem. Commun.* **2013**, *49*, 9449–9451.

[115] S. M. Cohen, *Chem. Rev.* **2012**, *112*, 970–1000.

[116] J. D. Evans, C. J. Sumby, C. J. Doonan, *Chem. Soc. Rev.* **2014**, *43*, 5933–5951.

[117] S. M. Cohen, *J. Am. Chem. Soc.* **2017**, *139*, 2855–2863.

[118] I. Nath, J. Chakraborty, F. Verpoort, *Chem. Soc. Rev.* **2016**, *45*, 4127–4170.

[119] S. Pullen, S. Ott, *Top. Catal.* **2016**, 1–10.

[120] C. Wang, Z. Xie, K. E. deKrafft, W. Lin, *J. Am. Chem. Soc.* **2011**, *133*, 13445–13454.

[121] C. Wang, J.-L. Wang, W. Lin, *J. Am. Chem. Soc.* **2012**, *134*, 19895–19908.

[122] B. Nepal, S. Das, *Angew. Chem. Int. Ed.* **2013**, *52*, 7224–7227.

[123] X.-F. Lu, P.-Q. Liao, J.-W. Wang, J.-X. Wu, X.-W. Chen, C.-T. He, J.-P. Zhang, G.-R. Li, X.-M. Chen, *J. Am. Chem. Soc.* **2016**, *138*, 8336–8339.

[124] B. Wurster, D. Grumelli, D. Hötger, R. Gutzler, K. Kern, *J. Am. Chem. Soc.* **2016**, *138*, 3623–3626.

[125] P. Manna, J. Debgupta, S. Bose, S. K. Das, *Angew. Chem. Int. Ed.* **2016**, *55*, 2425–2430.

[126] B. A. Johnson, A. Bhunia, S. Ott, *Dalton Trans.* **2017**, *46*, 1382–1388.

[127] N. Kornienko, Y. Zhao, C. S. Kley, C. Zhu, D. Kim, S. Lin, C. J. Chang, O. M. Yaghi, P. Yang, *J. Am. Chem. Soc.* **2015**, *137*, 14129–14135.

[128] I. Hod, M. D. Sampson, P. Deria, C. P. Kubiak, O. K. Farha, J. T. Hupp, *ACS Catalysis* **2015**, *5*, 6302–6309.

[129] H. Fei, M. D. Sampson, Y. Lee, C. P. Kubiak, S. M. Cohen, *Inorg. Chem.* **2015**, *54*, 6821–6828.

[130] Y. Lee, S. Kim, J. K. Kang, S. M. Cohen, *Chem. Commun.* **2015**, *51*, 5735–5738.

[131] T. Kajiwara, M. Fujii, M. Tsujimoto, K. Kobayashi, M. Higuchi, K. Tanaka, S. Kitagawa, *Angew. Chem. Int. Ed.* **2016**, *55*, 2697–2700.

[132] N. C. Burtch, H. Jasuja, K. S. Walton, *Chem. Rev.* **2014**, *114*, 10575–10612.

[133] A. Phan, C. J. Doonan, F. J. Uribe-Romo, C. B. Knobler, M. O'Keeffe, O. M. Yaghi, *Acc. Chem. Res.* **2010**, *43*, 58–67.

[134] M. Dan-Hardi, C. Serre, T. Frot, L. Rozes, G. Maurin, C. Sanchez, G. Férey, *J. Am. Chem. Soc.* **2009**, *131*, 10857–10859.

[135] K. Sasan, Q. Lin, C. Mao, P. Feng, *Chem. Commun.* **2014**, *50*, 10390–10393.

[136] R. Ahlrichs, M. Bär, M. Häser, H. Horn, C. Kölmel, *Chem. Phys. Lett.* **1989**, *162*, 165–169.

[137] A. D. Becke, *Physical Review A* **1988**, *38*, 3098–3100.

[138] J. P. Perdew, *Physical Review B* **1986**, *33*, 8822–8824.

[139] W. Koch, M. C. Holthausen, *A Chemist's Guide to Density Functional Theory*, 2nd Edition, Wiley-VCH, **2001**.

[140] G. Eilers, L. Schwartz, M. Stein, G. Zampella, L. de Gioia, S. Ott, R. Lomoth, *Chemistry – A European Journal* **2007**, *13*, 7075–7084.

[141] M. Reiher, O. Salomon, B. A. Hess, *Theor. Chem. Acc.* **2001**, *107*, 48–55.

[142] C. J. Cramer, D. G. Truhlar, *PCCP* **2009**, *11*, 10757–10816.

[143] A. D. Becke, *The Journal of Chemical Physics* **1993**, *98*, 1372–1377.

[144] S. H. Vosko, L. Wilk, M. Nusair, *Can. J. Phys.* **1980**, *58*, 1200–1211.

[145] P. J. Stephens, F. J. Devlin, C. F. Chabalowski, M. J. Frisch, *The Journal of Physical Chemistry* **1994**, *98*, 11623–11627.

[146] F. Weigend, R. Ahlrichs, *PCCP* **2005**, *7*, 3297–3305.

[147] A. Schafer, A. Klamt, D. Sattel, J. C. W. Lohrenz, F. Eckert, *PCCP* **2000**, *2*, 2187–2193.

[148] A. Juris, V. Balzani, F. Barigelletti, S. Campagna, P. Belser, A. von Zelewsky, *Coord. Chem. Rev.* **1988**, *84*, 85–277.

[149] B. Shan, T. Baine, X. A. N. Ma, X. Zhao, R. H. Schmehl, *Inorg. Chem.* **2013**, *52*, 4853–4859.

[150] J. G. Santaclara, F. Kapteijn, J. Gascon, M. A. van der Veen, *CrystEngComm* **2017**.

[151] E. Mijangos, S. Roy, S. Pullen, R. Lomoth, S. Ott, *Dalton Trans.* **2017**.

[152] H. Li, T. B. Rauchfuss, *J. Am. Chem. Soc.* **2002**, *124*, 726–727.

[153] J. M. Camara, T. B. Rauchfuss, *Nat Chem* **2012**, *4*, 26–30.

[154] M. V. Pavliuk, A. M. Cieslak, M. Abdellah, A. Budinska, S. Pullen, K. Sokolowski, D. L. A. Fernandes, J. Szlachetko, E. L. Bastos, S. Ott, L. Hammarstrom, T. Edvinsson, J. Lewinski, J. Sa, *Sustainable Energy and Fuels* **2017**.

[155] F. E. Hahn, W. W. Seidel, *Angew. Chem.* **1995**, *107*, 2938–2941.

[156] W. W. Seidel, F. E. Hahn, T. Lügger, *Inorg. Chem.* **1998**, *37*, 6587–6596.

[157] D. Sellmann, T. Becker, F. Knoch, *Chem. Ber.* **1996**, *129*, 509–519.

[158] H. V. Huynh, W. W. Seidel, T. Lügger, R. Fröhlich, B. Wibbeling, F. E. Hahn, *Z. Naturforsch.* **2002**, *57b*, 1401–1408.

[159] H. Fei, S. M. Cohen, *J. Am. Chem. Soc.* **2015**, *137*, 2191–2194.

[160] M. Mirmohades, S. Pullen, M. Stein, S. Maji, S. Ott, L. Hammarström, R. Lomoth, *J. Am. Chem. Soc.* **2014**, *136*, 17366–17369.

[161] F. I. Adam, G. Hogarth, S. E. Kabir, I. Richards, *Comptes Rendus Chimie* **2008**, *11*, 890–905.

[162] B. E. Barton, M. T. Olsen, T. B. Rauchfuss, *J. Am. Chem. Soc.* **2008**, *130*, 16834–16835.

[163] M. E. Carroll, B. E. Barton, T. B. Rauchfuss, P. J. Carroll, *J. Am. Chem. Soc.* **2012**, *134*, 18843–18852.

[164] A. K. Vannucci, S. Wang, G. S. Nichol, D. L. Lichtenberger, D. H. Evans, R. S. Glass, *Dalton Trans.* **2010**, *39*, 3050–3056.

[165] S. M. Cohen, Z. Zhang, J. A. Boissonnault, *Inorg. Chem.* **2016**, *55*, 7281–7290.

[166] P. Deria, W. Bury, J. T. Hupp, O. K. Farha, *Chem. Commun.* **2014**, *50*, 1965–1968.

[167] M. Kim, J. F. Cahill, H. Fei, K. A. Prather, S. M. Cohen, *J. Am. Chem. Soc.* **2012**, *134*, 18082–18088.

[168] M. Kim, J. F. Cahill, Y. Su, K. A. Prather, S. M. Cohen, *Chemical Science* **2012**, *3*, 126–130.

[169] H. Fei, J. F. Cahill, K. A. Prather, S. M. Cohen, *Inorg. Chem.* **2013**, *52*, 4011–4016.

[170] S. Pullen, H. Fei, A. Orthaber, S. M. Cohen, S. Ott, *J. Am. Chem. Soc.* **2013**, *135*, 16997–17003.

[171] C. H. Hendon, D. Tiana, A. Walsh, *PCCP* **2012**, *14*, 13120–13132.

[172] S. Lin, Y. Pineda-Galvan, W. A. Maza, C. C. Epley, J. Zhu, M. C. Kessinger, Y. Pushkar, A. J. Morris, *ChemSusChem* **2016**, n/a–n/a.

[173] S. J. Garibay, S. M. Cohen, *Chem. Commun.* **2010**, *46*, 7700–7702.

[174] H. Fei, S. M. Cohen, *Chem. Commun.* **2014**, *50*, 4810–4812.

[175] S. Bernt, V. Guillerm, C. Serre, N. Stock, *Chem. Commun.* **2011**, *47*, 2838–2840.

[176] V. Pascanu, Q. Yao, A. B. Gómez, M. Gustafsson, Y. Yun, W. Wan, L. Samain, X. Zou, B. Martín-Matute, *Chemistry (Weinheim an Der Bergstrasse Germany)* **2013**, *19*, 17483–17493.

[177] S. Roy, V. Pascanu, S. Pullen, G. G. Miera, B. Martin-Matute, S. Ott, *Chem. Commun.* **2017**, *53*, 3257–3260.

[178] C.-C. Hou, T.-T. Li, S. Cao, Y. Chen, W.-F. Fu, *Journal of Materials Chemistry A* **2015**, *3*, 10386–10394.

[179] H. Deng, C. J. Doonan, H. Furukawa, R. B. Ferreira, J. Towne, C. B. Knobler, B. Wang, O. M. Yaghi, *Science* **2010**, *327*, 846–850.

[180] P. S. Singh, H. C. Rudbeck, P. Huang, S. Ezzaher, L. Eriksson, M. Stein, S. Ott, R. Lomoth, *Inorg. Chem.* **2009**, *48*, 10883–10885.

[181] J. E. Mondloch, W. Bury, D. Fairen-Jimenez, S. Kwon, E. J. DeMarco, M. H. Weston, A. A. Sarjeant, S. T. Nguyen, P. C. Stair, R. Q. Snurr, O. K. Farha, J. T. Hupp, *J. Am. Chem. Soc.* **2013**, *135*, 10294–10297.

[182] I. Hod, W. Bury, D. M. Gardner, P. Deria, V. Roznyatovskiy, M. R. Wasielewski, O. K. Farha, J. T. Hupp, *The Journal of Physical Chemistry Letters* **2015**, *6*, 586–591.

[183] S. Yuan, W. Lu, Y.-P. Chen, Q. Zhang, T.-F. Liu, D. Feng, X. Wang, J. Qin, H.-C. Zhou, *J. Am. Chem. Soc.* **2015**, *137*, 3177–3180.

[184] J. D. Rocca, D. Liu, W. Lin, *Acc. Chem. Res.* **2011**, *44*, 957–968.

[185] T. Zhang, W. Lin, *Chem. Soc. Rev.* **2014**, *43*, 5982–5993.

[186] K. Meyer, M. Ranocchiari, J. A. van Bokhoven, *Energy Environ. Sci.* **2015**, *8*, 1923–1937.

[187] O. Shekhah, J. Liu, R. A. Fischer, C. Woll, *Chem. Soc. Rev.* **2011**, *40*, 1081–1106.

[188] A. Bétard, R. A. Fischer, *Chem. Rev.* **2012**, *112*, 1055–1083.

[189] Y. Hu, X. Dong, J. Nan, W. Jin, X. Ren, N. Xu, Y. M. Lee, *Chem. Commun.* **2011**, *47*, 737–739.

[190] A. Demessence, P. Horcajada, C. Serre, C. Boissiere, D. Grosso, C. Sanchez, G. Ferey, *Chem. Commun.* **2009**, 7149–7151.

[191] C.-W. Kung, T.-H. Chang, L.-Y. Chou, J. T. Hupp, O. K. Farha, K.-C. Ho, *Chem. Commun.* **2015**, *51*, 2414–2417.

[192] H. Yang, H. Fei, *Dalton Trans.* **2017**.

[193] H. Fei, S. Pullen, A. Wagner, S. Ott, S. M. Cohen, *Chem. Commun.* **2015**, *51*, 66–69.

[194] A. Wagner, S. Pullen, S. Ott, D. Primetzhofer, *Nuclear Instruments and Methods in Physics Research Section B: Beam Interactions with Materials and Atoms* **2016**, *371*, 327–331.

[195] J. A. Denny, M. Y. Darensbourg, *Chem. Rev.* **2015**, *115*, 5248–5273.

[196] T. B. Rauchfuss, *Acc. Chem. Res.* **2015**.

Acta Universitatis Upsaliensis

Digital Comprehensive Summaries of Uppsala Dissertations from the Faculty of Science and Technology 1498

Editor: The Dean of the Faculty of Science and Technology

A doctoral dissertation from the Faculty of Science and Technology, Uppsala University, is usually a summary of a number of papers. A few copies of the complete dissertation are kept at major Swedish research libraries, while the summary alone is distributed internationally through the series Digital Comprehensive Summaries of Uppsala Dissertations from the Faculty of Science and Technology. (Prior to January, 2005, the series was published under the title "Comprehensive Summaries of Uppsala Dissertations from the Faculty of Science and Technology".)

Distribution: publications.uu.se
urn:nbn:se:uu:diva-318975

ACTA
UNIVERSITATIS
UPSALIENSIS
UPPSALA
2017